Dublin City University

Growth by Pulsed Laser Deposition and Characterisation of Zinc Oxide Thin Films and Nanostructures

A thesis submitted for the degree of

Doctor of Philosophy

Presented to

School of Physical Sciences

Submitted by

Richard J. O'Haire

Supervisor

Dr. Jean-Paul Mosnier

1st December, 2009

Declaration

I hereby certify that this material which I now submit for assignment on the programme of study leading to the award of Doctor of Philosophy is entirely my own work and has not been taken from others save and to the extent that it has been cited and acknowledged within the text of my work.

.....

Richard J. O'Haire, 1st December, 2009

Student Number: 53128991

Abstract

This thesis describes the growth and characterisation of ZnO thin films and nanostructures grown using the pulsed laser deposition technique. In this technique, a solid state Nd:YAG laser operating at 266 nm and with a 6 ns pulse width was fired at a sintered, ceramic target to produce an expanding plume of ZnO into a vacuum chamber (pressures in the 10^{-1} mbar range). The plume material condenses on various substrates, chiefly sapphire, to form a thin film.

The samples were analysed using a range of structural, optical, and surface analyses to determine the effects that varying pressures, temperatures, and laser energy fluence had on the growth modes of these thin films and nanostructures. Additionally, a study was carried out to determine the effects a mixed background gas (O_2 and Ar) has on the nanostructured growth. A model for this case was proposed.

Finally, a biomedical application of ZnO was investigated to determine the potential of ZnO thin films for the sterilisation of biofilms of the bacterium *Staphylococcus epidermidis*. It was found that such a biofilm grown atop a ZnO thin film is inactivated after exposure to UV light while submerged in an aqueous solution.

Dedication

To Mom, Dad, & Ryan

It hailed that day.

Acknowledgements

First and foremost, I would like to thank my research supervisor, Dr. Jean-Paul Mosnier for all of his guidance and support over the years through both the good times and the bad. The blood, sweat, and tears paid off (plus I think I finally learned which direction to turn a spanner!) I would also like to thank both Dr. Enda McGlynn and Prof. Martin Henry for help and assistance in our collaborative ZnO endeavours. Also I would like to thank Prof. John Costello for support and discussions (some random, some not) over the years.

I would like to thank both Des Lavelle and Pat Wogan for their shop and electronics skills when sometimes they knew what you wanted or needed before yourself! Thanks also to Lisa Peyton, Shelia Boughton, and Alan Hughes for putting up with 5PM order forms and random requests along the way.

I also wish to thank those postgrads I've become friends with over the years including the 'oldest' group: Mark Stapleton (snarf), Murph, Deirdre McCabe and James, Brendan Ryan, and Pat Yeates. The 'intermediate' postgrads: Eoin, Conor, Justyna, and Alan. And, lastly, the 'newest' postgrads: Dardis, Caroline, Padraig, Mairead, Mossy, Vince, Conor (black), and my two understudies, Eanna and Jack.

I would also like to thank the postdocs that I've worked with who had bestowed as many life-lessons onto me as they did physics-related knowledge. Jean-Rene taught me things are always 'a bit more complicated' than I'd first imagine. Brendan (Anyong!) taught me things were a lot less complicated if I just sat back and rationalised. And finally, Subho, you taught me that I am just plain complicated - that and the value of research. Also a mention of thanks to both Deirdre Kilbane and Paddy Hayden for random things along the way.

I would like to thank postgrads/postdocs whom I've had the pleasure of

working with to publish papers together including Barry Brennan, Steve MacDonnell, Dorota Wencel, Lisa O'Reilly, and Maria Boyle (including her supervisor Dr. Kevin McGuigan).

Aside from the main physics crowd, I would also like to thank those who were and still are there outside of DCU including, Phil Smyth, Mike Kelly, Ciaran, Cathy, Aoife, Trevor, Kev, Claire Kelly, Jen Courtney, Tine, Anne Beaucamp (and Ethan!), Francesca, and Aoibheann. Also I would like to thank my friends waiting for my return on the other side of the pond for continued support. Pat (who's been there from high school) and Sarah - thanks for sheltering me every New Years. We'll get out to C.P. soon! Sara/Jess/April - thanks for the profound musings of the universe and continued Scrabble distractions. And lastly but not least, Leah and Todd - thanks for putting up with my absence for so long and for staying as true friends despite.

Also I quick thank you to all the girls in the registry (and invigilators) I've come to know, particularly Ger, Orna, Jenny, and Karen.

Lastly, and most importantly, I would like to thank my immediate (and extended) family who have been patiently waiting for this day to come. The support and encouragement given transatlantically through the thick and thin of it all was much needed and appreciated. It is of no surprise that I dedicate this work to them.

Publications

1. J.-P. Mosnier, R. J. O'Haire, E. McGlynn, M. O. Henry, S. J. McDonnell, M. A. Boyle, and K. G. McGuigan. ZnO films grown by pulsed-laser deposition on soda lime glass substrates for the ultraviolet inactivation of *Staphylococcus epidermidis* biofilms. *Science and Technology of Advanced Materials*, 10 (4) 045003, 2009.

2. R. O'Haire, E. McGlynn, M. O. Henry, and J.-P. Mosnier. ZnO nanostructured thin films grown by pulsed laser deposition in mixed O_2/Ar background gas. *Superlattices and Microstructures*, 42(1-6)468-472, 2007.

3. R. O'Haire, A. Meaney, E. McGlynn, M. O. Henry, J.-R. Duclère, and J.-P. Mosnier. Growth of crystalline ZnO nanostructures using pulsed laser deposition. *Superlattices and Microstructures*, 39(1-4)153161, 2006.

4. J.-R. Duclere, E. McGlynn, M. O. Henry, R. O'Haire, and J.-P. Mosnier. Nitrogen doping of ZnO thin films grown by plasma-assisted pulsed-laser deposition. *Journal of Physics Conference Series*, 59(1)505-509, 2007.

5. S. Chakrabarti, B. Doggett, R. O'Haire, E. McGlynn, M. O. Henry, A. Meaney, and J.-P. Mosnier. Characterization of nitrogen-doped ZnO thin films grown by plasma-assisted pulsed laser deposition on sapphire substrates. *Superlattices and Microstructures*, 42(1-6)21-25, 2007.

6. B. Doggett, S. Chakrabarti, R. O'Haire, A. Meaney, E. McGlynn, M. O. Henry, and J.-P. Mosnier. Electrical characterisation of phosphorus-doped ZnO thin films grown by pulsed laser deposition. *Superlattices and Microstructures*, 42(1-6)74-78, 2007.

7. R. Grunwald, U. Neumann, W. Seeber, H. Lange, J.-P. Mosnier, R. O'Haire, and E. McGlynn. Growth controlled and laser induced nanostructures in thin nonlinear optical ZnO layers. *Physics and Chemistry of Glasses - European Journal of Glass Science and Technology: Part B*, 48(3)134-137, 2007.

8. S. Chakrabarti, B. Doggett, R. O'Haire, E. McGlynn, M. O. Henry, A. Meaney, and J.-P. Mosnier. p-type conduction above room temperature in nitrogen-doped ZnO thin film grown by plasma-assisted pulsed laser deposition. *Electronics Letters*, 42(20)1181-1183, 2006.

9. J.-R. Duclère, C. McLoughlin, J. Fryar, R. O'Haire, M. Guilloux-Viry, A. Meaney, A. Perrin, E. McGlynn, M. O. Henry, and J.-P. Mosnier. ZnO thin films grown on platinum (111) buffer layers by pulsed laser deposition. *Thin Solid Films*, 500(1-2)78-83, 2006.

10. A. Meaney, J.-R. Duclère, E. McGlynn, J.-P. Mosnier, R. O'Haire, and M. O. Henry. Comparison of structural, optical and electrical properties of undoped ZnO thin films grown on *r*- and *c*-Al_2O_3 substrates using pulsed laser deposition. *Superlattices and Microstructures*, 38(4-6)256-264, 2005.

11. J.-R. Duclère, M. Novotny, A. Meaney, R. O'Haire, E. McGlynn, M. O. Henry, and J.-P. Mosnier. Properties of Li-, P- and N-doped ZnO thin films prepared by pulsed laser deposition. *Superlattices and Microstructures*, 38(4-6)397-405, 2005.

Contents

Chapter 1

Introduction

This thesis outlines the work done in controlling the growth of zinc oxide films and nanostructures via the pulsed laser deposition (PLD) technique with additional work in using the material as a possible biomedical application. PLD of thin film materials was developed in the mid-1960s but did not receive much attention until 1987 with the first laser deposited growth of the first high temperature superconductor, $YBa_2Cu_3O_7$ [1]. This technique had produced a higher quality thin film than any from the more elaborate techniques which previously eclipsed pulsed laser deposition. From then on, PLD became one of the leading competitors in high-quality thin films growth, and even more so with the development of more advanced lasers with shorter pulse widths.

Some of the main advantages PLD has over its competitors is the ability to deposit target material onto a substrate relatively quick and with the same initial stoichiometry of the target. Additionally, provided on the system configuration, PLD has the added ability to quickly change between targets during a growth process to produce multilayered films without the need to break vacuum or halt the programme. Pulsed laser deposition is not without its own drawbacks, the main one being the size scale on which samples can be produced. The size of the ablated plume is limited and some system configurations can allow

for covering larger areas, but they too would not be comparable to large-area deposition techniques, such as the sputtering or sol-gel. Also, constant ablating of the target causes erosion or pitting to the surface which necessitates the need to smooth and clean the target often. Equally, the surface of oxide material targets become chemically reduced due to oxygen-ambient growths over time, thus decreasing the ablated stoichiometric ratio of the target.

The material used throughout this work was zinc oxide (ZnO). ZnO is well know for its antibacterial properties and had been commonly used throughout the centuries in lotions, skin ointments and powders, and additionally, is usually the chief compound found in sunscreen lotion. It has also been widely used over hundreds of years as additives to common items such as paint bases, rubber, and cigarette filters. In the realm of materials research, the current focus on growth, development, and use of zinc oxide is just as widely varied as noted by extensive reviews [2, 3] and more so when it comes to ZnO in a nanostructured form [4, 5]. Much of this research spans different deposition and growth techniques such as chemical vapour deposition, sol-gel, molecular beam epitaxy, and to our concern, pulsed laser deposition.

Zinc oxide is an intrinsically n-type, group II-VI semiconductor with a wide band-gap of 3.37 eV at room temperature and a large exciton binding energy of 60 meV. This binding energy is much larger than some comparable semiconductors, for example gallium nitride (with a binding energy of 25 meV), which have enjoyed much success in terms of optoelectronic devices over the last decade. ZnO is difficult to dope p-type, yet despite this ZnO is potentially more of a favourable and lucrative semiconductor in the ultraviolet region. This larger binding energy means that the excitons are stable at temperatures much greater than room temperature ($\sim$423 °C) - an obvious advantage to certain consumer and industrial products.

ZnO commonly takes the structural forms of either the hexagonal wurtzite or cubic zincblende. Structurally the hexagonal wurtzite ZnO typically grows

along the [000l] axis[1], or the c-axis, as seen in Figure 1.1. The ZnO(0001)

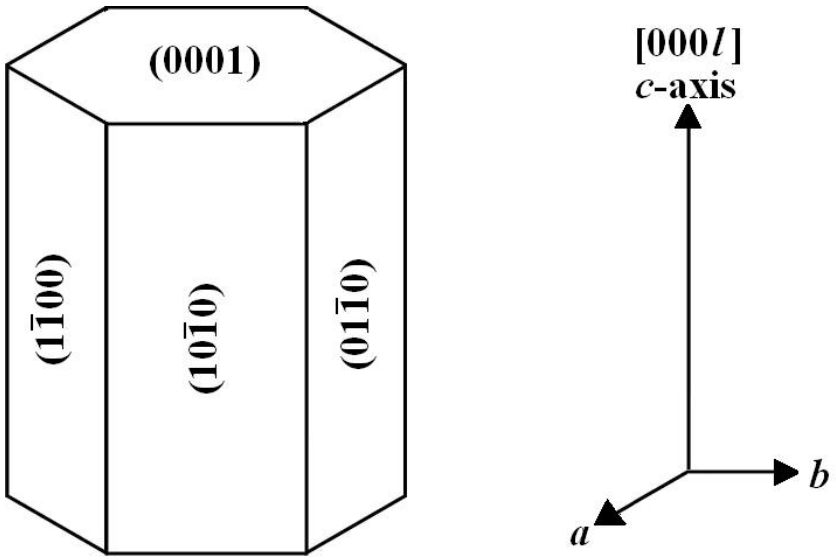

Figure 1.1: Image showing the main planar surfaces of the hexagonal ZnO on the left and the unit cell axes on the right.

face is Zn-terminated and the opposite ZnO(000$\bar{1}$) face is O-terminated. As ZnO is a polar material along the [0001]-direction [4], many of the resultant nanostructures observed in literature are formed along this primary axis or are intricately shaped due to the polar surface in the more delicate nanostructures, eg nano-helixes, nano-belts [6]. There is as much of a demand to understand the nature of these various nanometric structures and shapes as there is to develop methods of controlling their growth as simplistically as possible.

One main advantage PLD has with respect to nanostructures is that growth is typically a catalyst-free method, unlike vapour-liquid-solid (VLS) techniques which are commonly used for ZnO nanostructures [2, 3, 5]. Many VLS-grown nanostructures have been used for device applications, but recent works with PLD demonstrate that production of device quality ZnO nanostructures have

[1]Note that typically crystal planes and directions are notated with {h k l} Miller indexing, however it is typically the case, as seen throughout this work, hexagonal systems are notated as {h k -(h+k) l}.

also been used as field emitters, nanolasers, or optical resonators to name a few [2, 3, 5]. The corresponding growth mechanisms have also been studied, with a view to control and optimize the process. Several authors also report the formation of ZnO nanoclusters in the ablation plume with the PLD technique, which is recognised as the main process leading to the formation of nucleation sites for subsequent nanocluster growths [7–9].

Recent studies have found the semiconductor TiO_2 to use photocatalytic chemistry as a powerful disinfectant, for example [10]. This material, however, requires complex deposition methods [11] and furthermore is a possible carcinogen [12]. Therefore, ZnO, with its similar structural and antibacterial properties to that of TiO_2, became an ideal area of investigation for utilising ZnO as a potential device application. Additionally, the resistance of certain biofilms to all known antibiotics and forms of chemical treatments is driving substantial research into alternative disinfectant technologies. The choice bacteria used bacterial inactivation study, *Staphylococcus epidermidis*, is closely related to methicillin-resistant *Staphylococcus aureus* (MRSA) which is the leading cause of death from hospital-acquired infections.

Our motivation and goals throughout this work were:

- to produce high-quality ZnO material at par with what is found in literature,
- to produce and gain control over nanostructured ZnO material,
- to utilise ZnO in a novel way for a practical or device application, and
- to investigate and model the surface interactions at the interface of a ZnO material and a biofilm.

1.1 Thesis Layout

The thesis itself is divided into seven chapters. The following is a brief description of the contents for each chapter.

Chapter One:

gives the brief history, importance, and descriptions of the methods of materials growth as well as that of the material itself used throughout this thesis. Additionally, the motivations behind the research done are briefly mentioned.

Chapter Two:

outlines the theoretical background behind pulsed laser ablation, plume expansion, film deposition, and the atomic behaviour of the deposited particles on surfaces in relation to the data presented in the results and analysis chapters. Basic crystallisation and growth modes are also outlined.

Chapter Three:

details the experimental ultra-high vacuum system in its capabilities, motions, and limitations. It also includes the details on the purities of the materials, substrates, and gasses used throughout the research.

Chapter Four:

outlines and describes all of the *ex-situ* characterisations done on the samples after they had been produced and examples of each.

Chapter Five:

presents all of the data results, analyses, and conclusions on the majority of our research on zinc oxide. The work is presented in the linear and chronological order of progression from initial start-up research on

smooth, thin films through to the growth and control over nanostructured films.

Chapter Six:

presents research, analyses, and conclusions on the use of a zinc oxide thin film for the ultraviolet inactivation of a biofilm.

Chapter Seven:

presents a summarised conclusion for the work and results presented in this thesis. Additionally, potential future experiments and extensions of this work are discussed.

References

[1] D. Dijkkamp, T. Venkatesan, X. D. Wu, S. A. Shaheen, N. Jisrawi, Y. H. Min-Lee, W. L. McLean, and M. Croft. Preparation of Y-Ba-Cu oxide superconductor thin films using pulsed laser evaporation from high T_C bulk material. *Applied Physics Letters*, 51(8):619–621, 1987.

[2] D. P. Norton. Synthesis and properties of epitaxial electronic oxide thin-film materials. *Materials Science and Engineering: R*, 43(5-6):139–247, 2004.

[3] S. J. Pearton, D. P. Norton, K. Ip, Y. W. Heo, and T. Steiner. Recent progress in processing and properties of ZnO. *Progress in Materials Science*, 50(3):293–340, 2005.

[4] C. Wöll. The chemistry and physics of zinc oxide surfaces. *Progress in Surface Science*, 82(2-3):55–120, 2007.

[5] Z. L. Wang. ZnO nanowire and nanobelt platform for nanotechnology. *Materials Science and Engineering: R*, 64(3-4):33–71, 2009.

[6] X. Y. Kong and Z. L. Wang. Spontaneous polarization-induced nanohelixes, nanosprings, and nanorings of piezoelectric nanobelts. *Nano Letters*, 3(12):1625–1631, 2003.

[7] T. Okada, K. Kawashima, and M. Ueda. Ultraviolet lasing and field emis-

sion characteristics of ZnO nano-rods synthesized by nano-particle-assisted pulsed-laser ablation deposition. *Applied Physics A*, 81(5):907–910, 2005.

[8] I. Ozerov, A. V. Bulgakov, D. K. Nelson, R. Castell, and W. Marine. Production of gas phase zinc oxide nanoclusters by pulsed laser ablation. *Applied Surface Science*, 247(1-4):1–7, 2005.

[9] S. Choopun, H. Tabata, and T. Kawai. Self-assembly ZnO nanorods by pulsed laser deposition under argon atmosphere. *Journal of Crystal Growth*, 274(1-2):167–172, 2005.

[10] K. Hashimoto, H. Irie, and A. Fujishima. TiO_2 photocatalysis: A historical overview and future prospects. *Japanese Journal of Applied Physics*, 44(12):8269–8285, 2005.

[11] M. Maeda and T. Watanabe. Visible light photocatalysis of nitrogen-doped titanium oxide films prepared by plasma-enhanced chemical vapor deposition. *Journal of The Electrochemical Society*, 153(3):C186–C189, 2006.

[12] R. Baan, K. Straif, Y. Grosse, B. Secretan, F. El Ghissassi, and V. Cogliano. Carcinogenicity of carbon black, titanium dioxide, and talc. *The Lancet Oncology*, 7(4):295–296, 2006.

Chapter 2

Theoretical Background

Pulsed laser deposition is a method of materials growth, in which, a short-pulsed laser beam is focussed onto a target beyond the material's ablation threshold creating a plasma of the target material to expand towards and deposit onto a substrate under vacuum. A diagram is shown in Figure 2.1. This ejected material is comprised of ions, atoms, and molecules as it propagates, and, on reaching the substrate, they diffuse on the surface and arrange themselves in one or more crystallographic orientations. As this method was initially used for maintaining the stoichiometry of complex materials, it was later realised that it can also be used in the growth and control of micron- and nano-sized structures. In this chapter, the theory and background from the first laser pulse to crystalline modes of material growth will be examined.

2.1 Pulsed Laser Ablation

A plasma is a state of matter existing as a cloud of ionised gas, meaning that a system had been acted upon with energy sufficient enough to rip all or some of the electrons free of the atoms or molecules in that system. Since the coining of the term *plasma* by Irving Langmuir [1] in 1928, we now know of countless occurrences of these systems of ionised gasses throughout our universe. They can

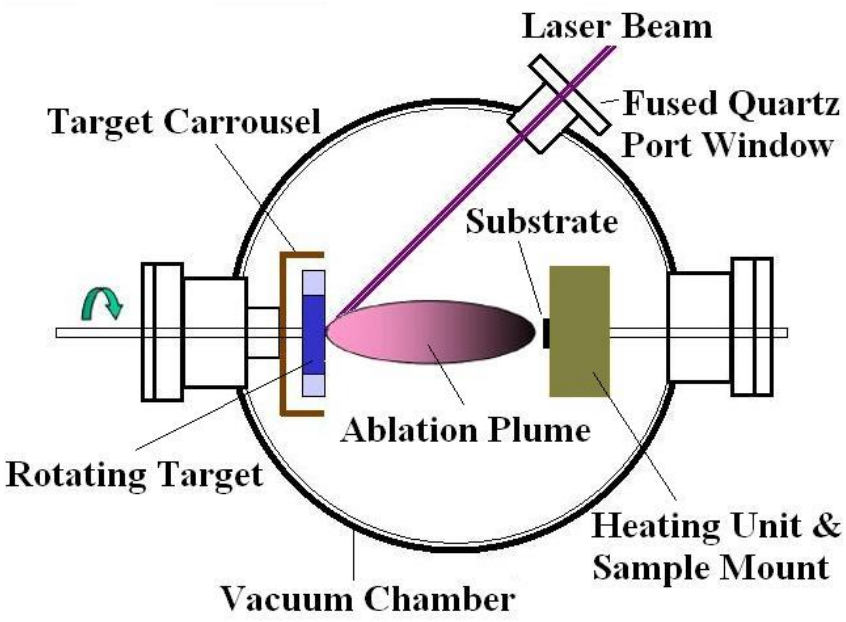

Figure 2.1: Diagram showing the overview of a pulsed laser deposition system as a laser ablates target material towards a substrate under vacuum.

be found scattered throughout as stars, nebulae, or intergalactic medium, right down to earthbound examples such as the mysterious aurorae and phenomenon of lightning. With such large amounts of naturally occurring plasmas, numerous uses of man-made plasmas are found in technology and manufacturing today because of extensive research done in this field, however, in the interest of this thesis, the type of plasma taken into consideration was laser produced.

2.1.1 Ambient Background Gasses

In this section, the basic dynamics of a background gas will be briefly discussed as studies throughout this work occurred within the presence of an ambient background gas during the production of a sample.

From the Ideal Gas Law the molecular density, n, can easily be derived by:

$$n = \frac{p}{k_B T} \tag{2.1}$$

where p is the pressure, k_B is the Boltzmann's constant, and T is the temperature of the gas. Then, in knowing n, the mean free path can be worked out by:

$$\lambda = \frac{1}{\sqrt{2}n\sigma^2} \tag{2.2}$$

where σ^2 is the cross-sectional area for molecular collisions equal to that of twice the diameter of the molecule for a Maxwellian distribution of velocities. As calculated by Maxwell and Boltzmann, the distribution of these velocities goes as:

$$P(v) = 4\pi \left(\frac{m}{2\pi k_B T}\right)^{3/2} v^2 e^{-\frac{mv^2}{2k_B T}} \tag{2.3}$$

where m is the mass of the molecule. This is a probability distribution where the area under the curve, *P(v)* $\mathrm{d}v$, is a dimensionless quantity representing the possibility of fraction of molecules within the width of $\mathrm{d}v$ centered at v for a particular speed. From this distribution, the average speed of the molecules, v_{avg}, is found by integrating the product of each velocity by the probability of a molecule having that velocity over the entire range of possible velocities. Similarly the root-mean-squared (RMS) velocity can be found by substituting v_{avg} for $(v^2)_{\text{avg}}$ in the calculations. Both are derived as follows:

$$v_{\text{avg}} = \int_0^\infty vP(v)\mathrm{d}v = \pi\sqrt{\frac{8k_B T}{m\pi}} \tag{2.4}$$

$$v_{\text{rms}} = \sqrt{(v^2)_{\text{avg}}} = \sqrt{\int_0^\infty v^2 P(v)\mathrm{d}v} = \sqrt{\frac{3k_B T}{m}} \tag{2.5}$$

The average kinetic energy of the molecule from $\frac{1}{2}mv^2$ can be found by substituting v_{rms} from equation (2.5) for v to yield:

$$K_{\text{avg}} = \frac{1}{2}mv_{\text{rms}}^2 = \frac{3}{2}k_B T \tag{2.6}$$

Now that the basic dynamics of the ambient background gasses have been defined, it leads next to develop the dynamics of a plasma in this environment, detailed in the following section.

2.1.2 Laser Induced Plasmas

The entire method of growing a pulsed laser deposited sample begins with just that - a pulsed laser. For our process, a laser fires a short pulse-width burst of energy at some rate of repetition [units of Hz]. The choice of laser used has a nanosecond pulse-width, and has an associated value of energy per cross-sectional area, defined as fluence [units of J/cm^2]. As the laser light interacts with a material, a percentage of this light radiation is absorbed into the material while the rest is reflected. If enough energy is absorbed by the material sufficient enough to break the chemical bonds holding the material together, then the ablation threshold has been surpassed and instantaneously, a cloud of ionised gas of target material propagates from the target surface. This plasma is commonly called an ablation plume and can occur either in vacuum or in the presence of a background gas.

2.1.2.1 Laser-Solid Interaction

As a pulse of laser light first comes into contact with a metallic surface, the energy of the pulse that is not reflected is transferred into the target. The distance at which this portion of energy penetrates the material is called the skin depth, δ, given by

$$\delta = \sqrt{\frac{2}{\omega\mu\sigma}} \tag{2.7}$$

where ω is the angular frequency of the light radiation, μ is the magnetic permeability of the target material, and σ is its conductivity. It is within this skin depth layer where electrons absorb the radiation and raise them to higher energy states. This subsequently heats, melts, and vapourises the interacted region. The area of the target material below the skin depth subsequently heats to a depth known as the heat penetration depth, L_{th}, given by

$$L_{th} = \sqrt{\frac{2k\tau_p}{\rho c}} \tag{2.8}$$

where k is thermal conduction, τ_p is the pulse length of the laser, ρ is the material's mass density, and c is the speed of light [2]. According to Amoruso *et al.*, because vapourising a metal demands much more energy than to melt one, evaporation will occur when the energy (per unit volume) absorbed into the vapourised layer surpasses the latent heat of evaporation (per unit volume). This ablation depth, Δz_v, is given by

$$\Delta z_v \approx \frac{A(F_L - F_{th})}{\rho L_v} \tag{2.9}$$

where A is the surface absorbance of the target, F_L is the fluence of the laser, L_v is the latent heat per unit mass, and the F_{th} is the laser fluence threshold representing the minimum energy above which appreciable vapourisation occurs [2]. As target material vapourises it then propagates outwards from the target surface. This expansion into either vacuum or presence of a background gas is briefly looked at in the following two subsections.

2.1.2.2 Plume Expansion Under Vacuum

As a laser introduces energy sufficient enough to create an ablation plume, collectively this system of ions and electrons of an initially neutral matter is assumed to maintain this neutrality over the lifetime of the plasma. This electron neutrality is given by

$$n_{\mathrm{e}} = \sum_z n_{\mathrm{z}} z \tag{2.10}$$

where n_{e} is the electron density and n_z is the density of the ions of charge z [3]. This system exhibits a collective phenomena which, according to Carroll and Kennedy, is the basic defining characteristic of plasmas and is quantifiable as the Debye length, or λ_D. This means that any charge within the plasma will be acted upon by another of opposite charge by a calculable Coulombic force. The Debye length then is the distance beyond this collective phenomena at

which separation can occur in vacuum is given by

$$\lambda_D = \sqrt{\frac{\varepsilon_0 k_B T}{n_e e^2}} \tag{2.11}$$

where ε_0 is the permitivity of free space, T is the plasma temperature, and e is the electron charge [3].

According to the authors [2, 4], the plume evolution over the time of laser impact to expansion can be broken into two regions over that time. The first segment, during the incidence of the laser pulse itself, can be described as an isothermal expansion. The equation of this expansion is given by

$$\begin{aligned} X(t)\left(\frac{1}{t}\frac{dX}{dt} + \frac{d^2X}{dt^2}\right) &= Y(t)\left(\frac{1}{t}\frac{dY}{dt} + \frac{d^2Y}{dt^2}\right) \\ &= Z(t)\left(\frac{1}{t}\frac{dZ}{dt} + \frac{d^2Z}{dt^2}\right) \\ &= \frac{k_B T}{m}, t \leq \tau \end{aligned} \tag{2.12}$$

where m is the mass of the particles [2, 4]. The $X(t)$, $Y(t)$, and $Z(t)$ terms denote the dimensions for plasma expansion as a function of time along the general x-, y-, and z-axes.

The second segment of expansion, beginning at the termination of the laser pulse, can be described as an adiabatic expansion. The equation for this is given by

$$\begin{aligned} X(t)\left(\frac{d^2X}{dt^2}\right) &= Y(t)\left(\frac{d^2Y}{dt^2}\right) \\ &= Z(t)\left(\frac{d^2Z}{dt^2}\right) \\ &= \frac{k_B T}{m}\left(\frac{X_0 Y_0 Z_0}{X(t)Y(t)Z(t)}\right)^{\gamma-1}, t > \tau \end{aligned} \tag{2.13}$$

where X_0, Y_0, and Z_0 are the initial orthogonal edges of the plasma after the termination of the laser pulse ($t = \tau$) and γ is the ratio of the specific heat capacities at constant pressure and volume [4].

2.1.2.3 Plume Expansion in a Gas

The expansion of a plasma into a background gas is a complex process and is still being researched and understood, eg [5, 6]. Some groups show that if a plasma expands into a gas typically less than pressures of 100 mTorr, then the ambient gas will have a negligible effect and can be treated as if it were expanding in a vacuum. Beyond that, a shock wave will form at the leading surface of the expanding volume of the plasma [5–8].

Three models are typically used to try and describe the expansion of the laser produced plume: drag model [7, 9, 10], diffusion model [11], and the shock wave model [7, 8]. The drag model as described by D.B. Geohegan is regarded an ensemble which experiences a viscous force proportional to its velocity through the background gas [9]. This was found to hold true for the ablated species which were heavier than that of the background gas [7, 9]. The diffusion model follows a likeness to that of particles diffusing through a material, in research by A.V. Rode *et al.*, carbon plume species through an ambient gas of argon [11]. The shock wave model is used to describe the final stages of plume expansion with the presence of a shock wave formation as the plume rapidly expands into the background gas [7, 8]. Harilal *et al.* also note that the plume expansion can be treated as a free expansion in pressures less than 10^{-2} Torr [8].

Assuming the presence of a shock wave due to the pressures throughout this work, the calculated position of the shock wave itself (R_{sw}) is given by [12, 13]

$$R_{sw}(t) = \alpha \left(\frac{E_0}{\rho_0} \right)^{\frac{1}{(2+\zeta)}} t^{\frac{2}{(2+\zeta)}} \tag{2.14}$$

and [14]

$$\alpha = \left[2 \left(\frac{75(\gamma-1)(\gamma+1)^2}{16\pi(3\gamma-1)} \right) \right]^{\frac{1}{(2+\zeta)}} \tag{2.15}$$

where E_0 is the energy gone into creating the plasma itself, ρ_0 is the density of the ambient background gas, γ is the polytropic index of the background gas,

and ζ is a parameter that accounts for the dimensionality of propagation (for spherical propagation $\zeta = 3$, for cylindrical propagation $\zeta = 2$, and for planar propagation $\zeta = 1$) [13].

Theoretically the shock wave will have a gaseous thickness, Δ_{sw}, given by [15]

$$\Delta_{sw}(t) = \frac{R_{sw}(\gamma - 1)}{3(\gamma + 1)} \tag{2.16}$$

and if this is significantly larger than the diffusion length of the ambient gas molecules, given by

$$l_{Diff} = 2\sqrt{Dt} \tag{2.17}$$

then a shock wave will occur. The D in this case is the diffusion coefficient and as follows [16]

$$D = D_0 \left(\frac{T_{sw}}{T_0}\right)^{0.75} \left(\frac{\rho_A}{\rho_{sw}}\right) \tag{2.18}$$

where T_{sw} is the temperature of the gas ahead of the shock wave, T_0 is the temperature of the ambient background gas, ρ_A is the density of the gas at atmospheric pressure, and ρ_{sw} is the density of the gas ahead of the shock wave. The terms T_{sw} and ρ_{sw} are defined as follows [16]

$$T_{sw} = \frac{2\gamma}{\gamma + 1}\left[\frac{(\gamma - 1)}{(\gamma + 1)}M^2 + 1\right] T_0 \tag{2.19}$$

and

$$\rho_{sw} = \rho_0 \frac{\gamma + 1}{\gamma - 1} \tag{2.20}$$

where $M = R_{sw}/c$ is the Mach number.

2.2 Pulsed Laser Deposition

Up until the mid-19$^{\text{th}}$ Century, crystals were merely naturally occurring solids that were recorded and classified by physical observations and measurements.

During this century, the need was seen to classify the composition crystals further still, eventually creating the fields of crystallography and solid state physics. During the 1920s greater understanding of crystals and their natural and man-made formations was achieved which laid the path for understanding the process of crystallisation and modes of this crystal growth. Today these are the basic tools needed in understanding the complex formation, growth, and manipulation of crystals.

With the pulsed laser deposition method of crystalline growth, the expanding plume as described in the previous section, is the beginning of the growth process. As the ablated plume expands under some finite vacuum pressure, it propagates towards a substrate for film deposition. The substrate is typically crystalline in order to facilitate the growth of a crystalline film, but is not necessary. This section will develop the interactions between the first atoms as they reach the surface of the substrate through to a fully grown film.

2.2.1 Crystal Seeding

As each plume of laser ablated material adiabatically expands towards the surface of a substrate, we will consider the initial interaction with the surface just prior to the first particle touching the surface. We can also begin by treating each of the species of the plume individually as they strike the substrate surface. In this section, the interaction between the plume and the substrate surface is developed first assuming a perfect crystal.

2.2.1.1 Surface Interaction

When a particle from the expanding plume first comes into contact with a substrate surface, it will have some potential energy, ϕ, of attractiveness or repulsion with the surface as a function of distance r between the two objects. This potential energy function is commonly represented by the Lennard-Jones

potential, which is

$$\phi(r) = \varepsilon_{\mathrm{B}} \left[\left(\frac{r_e}{r} \right)^{12} - 2 \left(\frac{r_e}{r} \right)^{6} \right] \tag{2.21}$$

where ε_{B} is the minimum potential energy located at a distance r_e where the particles are at equilibrium. At any interatomic separation distance greater than r_e the incoming particle will adsorb to the substrate surface, which arises from the r^{-6} term. This term is commonly known as the weak van der Waals interaction. If the separation is less than r_e than the particle will experience a repulsion by the r^{-12} term due to the Pauli exclusion principle.

When impinging particles are subjected to substrate surface forces, they all have the possibility of either adsorbing or desorbing from the surface. Treating the particles within the propagating plume as gas particles, we could assume that the flux of particles which pass through an arbitrary unit of space which goes as $nv/4$. Therefore, by substituting equations (2.1) and (2.5)into this, the average molecular flux is:

$$\Gamma_{\mathrm{avg}} = \frac{p}{\sqrt{2\pi m k_B T}} \tag{2.22}$$

where m is the mass of a molecule or here, an impinging particle. This average flux is equally a rate at which particles impinge the surface, or $\mathrm{d}N/\mathrm{d}t$. As the surface progresses from one atomically smooth layer through deposition to another atomically smooth layer, a monolayer (ML) is formed. Thus we can determine the time it takes for a single monolayer to form on top of a surface at a particular pressure and temperature from:

$$\tau_{ML} = \frac{n_0}{\Gamma} = \frac{n_0 \sqrt{2\pi m k_B T}}{p} \tag{2.23}$$

where n_0 is the total number of atoms in a monolayer. The coverage is usually denoted as the range $0 < \vartheta < 1$ representing the percentage of completion for a single monolayer. Therefore, for a surface with a possible n_0 sites which a particle may occupy, ϑ may not exceed the ratio of n_0/n_{a} for the number n_{a} particles on the single surface.

Now, from equation (2.22), we can show that the rate at which a monolayer forms is directly proportional to $\frac{\mathrm{d}N}{\mathrm{d}t}$ by a coefficient, S, called the sticking coefficient, i.e.

$$\frac{\mathrm{d}\vartheta}{\mathrm{d}t} = S\frac{\mathrm{d}N}{\mathrm{d}t} \tag{2.24}$$

and rearranging we solve for S,

$$S(\vartheta) = \sqrt{2\pi m k_B T}\frac{1}{p}\frac{\mathrm{d}\vartheta}{\mathrm{d}t} \tag{2.25}$$

This particle will stick to the surface for a time, τ_{ad} given by [17]

$$\tau_{ad} = \frac{h}{k_B T_\theta} e^{\left(\frac{-\Delta H_{ad}}{k_B T}\right)} \tag{2.26}$$

where h is Plank's constant, T_θ is the Debye temperature, and ΔH_{ad} is the binding energy of an adatom to the surface.

2.2.1.2 Adatom Surface Movements and Nucleation

For those impinging particles that become adsorbed to the substrate or film surface, we begin to look at the basic motions of travel they undergo. Those particles that either ricocheted off the surface or desorbed due to an excess amount of latent energy no longer concern us anymore.

Assume initially that these atomic sized particles are cubic and are being deposited onto an array of packed 'crystalline' cubes, i.e. an atomically flat substrate surface. This model is close enough to gain perspective to what occurs initially and can be extrapolated to the hexagonal ZnO crystal structure. One particle that first interacts with the surface will have some initial energy before reaching the surface itself. This free energy particle, say with energy ε_0, will adhere to the surface provided the activation energy level is surpassed. Once this free particle adheres to the surface, it is known as an adatom. This lone adatom will have just the single contact, or nearest neighbour, with one face of the cube. This interaction between the surface and the nearest neighbour

would thus reduce the overall potential energy of the initially free particle, ε_0, to ε_A for the adatom. This single bond is weak enough to allow the adatom to travel the surface until it interacts with another adatom like itself, a dislocation on or in the surface, or simply becomes a location for which other species of the plume become attracted.

As the adatom travels along the surface, there are a number of locations which it may come across in its journey, including another adatom, a step-location, a kink-location, a hole within a step, or even a hole in the surface itself, as shown in Fig 2.2. First we take a look at a situation where a an

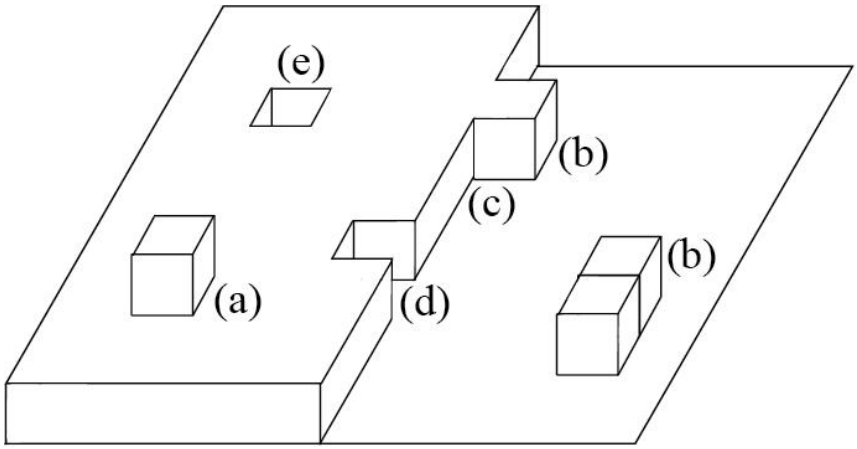

Figure 2.2: Image of the Terrace-Kink-Step model and the 5 main dislocation sites: (a) an adatom, (b) a step, (c) a kink, (d) a ledge or terrace, and (e) a vacancy. (b) is also depicted as a stand-alone nucleation site which would have the same nearest neighbours as a step. A bulk adatom within the film is not depicted.

adatom encounters a step (a.k.a. ledge) on the surface. It will then have 2 nearest neighbours and the potential energy of the adatom would reduce to that of a step particle ε_S. Theoretically, two free adatoms conjoining would be in itself the beginning of a step, or more commonly referred to as a nucleation site for nanostructured growth.

Next, if an adatom migrates into a corner formed by two perpendicular steps, also known as a kink, where half of its bonds would be incorporated into

the depositing film, and would have a kink energy of ε_{K}. If the adatom joins to separated steps to form a ledge, it bonds with 4 nearest neighbours and would have an energy of ε_{L}. As a film is deposited onto a substrate and particles begin to fill in all of the dislocations, vacancies are eventually left in the film. A particle that fills this vacancy would bond with 5 nearest neighbours and would have an energy of ε_{V}. Lastly, an adatom can also be thought of as a particle buried within the bulk of the crystalline film. This bulk adatom with all bonds shared, would have the lowest potential energy of ε_{B}, same as found in prior equation (2.21).

As the adatoms randomly diffuse across the surface and a monolayer after monolayer form, various dislocation sites will develop. As they do, the locations with a greater number of unsatisfied nearest neighbours will be attracted to those with lower potential energies. Before each monolayer begins to develop, it first initiates at nucleation sites across the substrate and subsequent film layers. Initially some free-traveling adatoms become seeds which develop into these nucleation sites.

The rate of 2D nucleation at each of these locations is given by a fairly complex rate equation which will not be listed here. It is, however, at these nucleation sites that will attract impinging particles as they near the surface or travel along the surface depending on the mode growth discussed later. If they are not affected by the nucleation sites, then they may either form their own site or randomly travel the surface until encountering some surface defect.

Depending on the conditions of growth, various ways in which the films will develop must be considered. The manner in which they crystallise and grow will be discussed in the following section.

2.3 Thin Film Crystallisation and Growth

As the atoms and molecules travel across the surface of the substrate and either seed a growth site or find a niche on a preexisting one, layers start to form. Throughout this upwards growth, numerous atomic and nanometric scaled occurrences start to emerge. As mentioned in the previous section, this is not a perfect crystal scenario, and defects do commonly occur due to such issues as lattice matching, stress, strain, dislocations, and other such defects found in most crystals. Here, in this section, we will develop these ideas as they are key to understanding the foundations of structures grown in the nanometric and micron regime.

2.3.1 Stress, Strain, Lattice Mismatch & Epitaxial Relationships

For the sake of the preceding section, we assumed an influx of particles which were cubic to help develop a generic model for explaining adatom and surface attraction, however as mentioned the systems in common practice are usually much more complex. Therefore, not only is the perfect crystal scenario difficult to achieve in the laboratory, but resultant film outcomes due to certain growth conditions for some materials are still being investigated. This vast array of both deposited materials and choice of substrate material causes unique sets of stresses and associated strains between a substrate and the depositing material.

Stress is given as the amount of work applied to a surface area and strain is the amount of (dimensionless) deformation that a material undergoes due to the stress. As the crystalline lattice structure of a substrate may, and usually does, vary from that of a deposited material as a bulk, the result is a mismatch between the lattices of the substrate and the film. Between these two materials,

there exists a quantifiable mismatch, δ by the simple relationship:

$$\delta = \frac{a_f - a_s}{a_s} \times 100\% \tag{2.27}$$

where a_f and a_s are the lengths of the crystal unit cell for the film and substrate, respectively.

Epitaxy, by definition, is used to describe the growth of one crystalline material on the surface of another with either a similar lattice structure, specifically in this case, a film on a substrate. As the substrate and film lattices can be described by some percentage of mismatch, they are also correlated by a comparison between a particular plane and directional orientation for each. This standard way of linking the crystalline orientations of both the substrate crystal and ZnO crystal is called an epitaxial relationship. This is done by expressing a relationship between parallel crystalline planes in each, and then defining parallel orientational directions within the planes. The epitaxial relationships are chosen for simpler planes and orientations, as they can be quite difficult to calculate for more complex crystals. Note that these epitaxial relationships, while particularly defining of the growth orientation, are not necessarily unique.

From x-ray diffraction, under a particular type of measurement called a ϕ-scan which is detailed in §4.1, we can determine and compare to reported epitaxial relationships between our main deposited material and the cuts of substrates used throughout this work. The epitaxial relationship between ZnO and a-Al_2O_3 is reported [18, 19] as

$$(0001)[11\bar{2}0]_{\text{ZnO}} \parallel (11\bar{2}0)[0001]_{\text{sapphire}} \tag{2.28}$$

with the lowest lattice mismatch of a typical 0.08% where the projection of the $[11\bar{2}0]$ direction onto the (0001) plane of ZnO is parallel with those of the sapphire substrate.

The epitaxial relationship between ZnO and r-Al_2O_3 is reported [20] as

$$(11\bar{2}0)[0001]_{\text{ZnO}} \parallel (01\bar{1}2)[0\bar{1}11]_{\text{sapphire}} \tag{2.29}$$

with a mismatch of 1.53% (along the c-axis which later mentioned runs along the surface of the r-Al_2O_3 substrate).

The epitaxial relationship between ZnO and c-Al_2O_3 slightly more complicated as there are 3 relationships which have been determined to exist and are reportedly [18–22] given as

$$(0001)[10\bar{1}0]_{\mathrm{ZnO}} \parallel (0001)[10\bar{1}0]_{\mathrm{sapphire}} \tag{2.30}$$

$$(0001)[1\bar{2}10]_{\mathrm{ZnO}} \parallel (0001)[1\bar{2}10]_{\mathrm{sapphire}} \tag{2.31}$$

$$(0001)[10\bar{1}0]_{\mathrm{ZnO}} \parallel (10\bar{1}4)[1\bar{2}10]_{\mathrm{sapphire}} \tag{2.32}$$

with a corresponding lattice mismatches of 31.8%, 18.3% and 2.2%. The first of these three is the scenario where the ZnO film lattice directly matches with the lattice of the sapphire. Sapphire unit cell itself is not hexagonal in structure, but rhombohedral. However, the unit cell can be considered hexagonal with a 3-fold rhombohedral symmetry. So if the ZnO lattice directly matches the underlying hexagonal lattice of the sapphire, the mismatch should be the mentioned 31.8%. Under certain temperature growth conditions, the ZnO lattice can be found rotated by 30° to that of the sapphire and is reportedly due to ZnO flipping its surface polarity [21], and will result in the second epitaxial relationship with a lesser compressive lattice mismatch. The last case was reported by Baxter *et al.* [18], but was not seen in the work in this thesis.

Lastly, as some work was done on silicon and glass substrates, it must be noted that it is difficult to grow ZnO epitaxially onto Si-substrates without the aid of buffer layers[23] therefore there are none listed. Additionally, as glass is an amorphous material, there are also no associated lattice mismatches between the film and substrate.

The stresses and strains on the ZnO lattice during deposition due to attributing these lattice mismatches and epitaxial relationships, various modes in which the film develops can occur and are the focus of the next section.

2.3.2 Growth Modes

There are 5 different crystal growth modes that can possibly occur. A diagram of the progress of these 5 growth modes are depicted in Figure 2.3 showing as the film is less than 1 monolayer (ML) through to more than 2 monolayers. The first

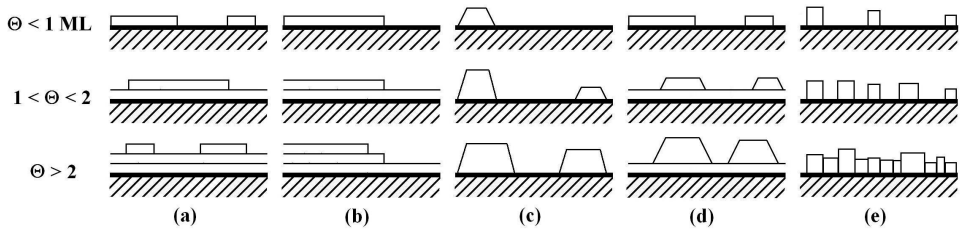

Figure 2.3: Image depicting the progression of crystal growth over time of monolayer coverage, Θ, similarly shown in book by M.A. Herman *et al.* [24]. The five modes of crystal growth shown are (a) layer-by-layer, (b) step-flow, (c) island growth, (d) layer-by-layer with island growth, and (e) columnar growth.

is the layer-by-layer or Frank-van der Merwe growth mode (see Fig 2.3(a)) [17, 24, 25]. This mode is the simplest growth where a stable monolayer will form on the surface of the substrate before another one begins and eventually ends with a smooth film.

The second type of growth mode is the step-flow growth mode (see Fig 2.3(b)) [24]. This is similar to the layer-by-layer growth except the layers form as a series of planar steps. The eventual film may have an atomically terraced effect rather than a smooth surface.

The third mode seen in Figure 2.3(c) is the island or Volmer-Weber growth mode [17, 24, 25]. This growth mode begins because adatoms nearing the surface are more attracted to nucleated growth sites rather than the interaction between the adatom and the surface. This causes an island-like structure to form directly on the substrate surface. As more and more adatoms join the the nucleation sites, these islands dominate the overall film growth. As is-

lands develop and meet other islands, they tend to merge and cover the whole substrate [24, 25].

The fourth is a combination of the layer-by-layer growth with an additional island growth mode on top (see Fig 2.3(d)) [17, 24, 25]. This is more commonly known as the Stranski-Krastanov or SK-mode. This growth mode is simply a combination of the last two modes where first a layer-by-layer film will develop. Eventually a stress may build up in the developing thin film where eventually it is more structurally and thermodynamically stable to begin a 3D island-type growth. From this point on, as with the Volmer-Weber mode, the islands will then dominate the remainder of the film growth. As more material is deposited and the islands meet, they tend to merge and form another layer underneath while continuing island growth.

The fifth and last type called columnar growth mode (see Fig 2.3(e)) [17, 24], is somewhat similar to both the Volmer-Weber and SK growth modes where merging islands form a connected structure underneath [24]. However in with columnar growth, as the columns widen and eventually meet, they retain their shape throughout the entire thickness of the deposited film.

The transition stage from a 2D layer-by-layer growth mode to a 3D island growth mode is when the potential for a particle's attraction to another particle overcomes its potential attraction to the substrate or surface. This simply means that until there is enough stress built up in the film, it will fail to grow more stable vertically and will continue growing parallel to the substrate surface.

2.3.3 Cluster Formation

In addition to the crystal growth modes just listed, there is also another form of crystallisation that has been under investigation by some research groups [26–28]. Evidence from this research points towards in-plume crystallisation, and is

sometimes referred to as nanoparticle-assisted PLD (NAPLD). The formation of nanoclusters in the ablation plume and their deposition onto the substrate have been recognised by these authors as the main process leading to the formation of nucleation sites for subsequent nanocluster growths. It has also been proposed that a combination of SK-mode nucleation followed by NAPLD assisted growth can occur [29]. These ideas are important to the work done in this thesis and this is our main avenue of research and will be further discussed in Chapter 5.

References

[1] I. Langmuir. Oscillations in Ionized Gases. *Proceedings of the National Academy of Sciences of the United States of America*, 14(8):627–637, 1928.

[2] S. Amoruso, R. Bruzzese, N. Spinelli, and R. Velotta. Characterization of laser-ablation plasmas. *Journal of Physics B: Atomic, Molecular and Optical Physics*, 32(14):R131–R172, 1999.

[3] P. K. Carroll and E. T. Kennedy. Laser-produced plasmas. *Contemporary Physics*, 22(1):61–96, 1981.

[4] R. K. Singh and J. Narayan. Pulsed-laser evaporation technique for deposition of thin films: Physics and theoretical model. *Physical Review B*, 41(13):8843–8859, 1990.

[5] S. Amoruso, A. Sambri, and X. Wang. Plume expansion dynamics during laser ablation of manganates in oxygen atmosphere. *Applied Surface Science*, 253(19):7696–7701, 2007.

[6] A. Bailini, P. M. Ossi, and A. Rivolta. Plume propagation through a buffer gas and cluster size prediction. *Applied Surface Science*, 253(19):7682–7685, 2007.

[7] J. Gonzalo, C. N. Afonso, and I. Madariaga. Expansion dynamics of the plasma produced by laser ablation of $BaTiO_3$ in a gas environment. *Journal of Applied Physics*, 81(2):951–955, 1997.

[8] S. S. Harilal, C. V. Bindhu, M. S. Tillack, F. Najmabadi, and A. C. Gaeris. Internal structure and expansion dynamics of laser ablation plumes into ambient gases. *Journal of Applied Physics*, 93(5):2380–2388, 2003.

[9] D. B. Geohegan. Fast intensified-CCD photography of $YBa_2Cu_3O_{7-x}$ laser ablation in vacuum and ambient oxygen. *Applied Physics Letters*, 60(22):2732–2734, 1992.

[10] S. Acquaviva and M. L. De Giorgi. Study of kinetics of atomic carbon during laser ablation of graphite in nitrogen by time- and space-resolved emission spectroscopy. *Applied Surface Science*, 186(1-4):329–334, 2002.

[11] A. V. Rode, E. G. Gamaly, and B. Luther-Davies. Formation of cluster-assembled carbon nano-foam by high-repetition-rate laser ablation. *Applied Physics A: Materials Science & Processing*, 70(2):135, 2000.

[12] L. I. Sedov. *Similarity and Dimensional Methods in Mechanics*. Academic Press, New York, 1959.

[13] G. Callies, P. Berger, and H. Hugel. Time-resolved observation of gas-dynamic discontinuities arising during excimer laser ablation and their interpretation. *Journal of Physics D: Applied Physics*, 28(4):794–806, 1995.

[14] M. Aden, E. W. Kreutz, H. Schluter, and K. Wissenbach. The applicability of the Sedov-Taylor scaling during material removal of metals and oxide layers with pulsed and excimer laser radiation. *Journal of Physics D: Applied Physics*, 30(6):980–989, 1997.

[15] J. L. Bobin, Y. A. Durand, Ph. P. Langer, and G. Tonon. Shock-wave generation in rarefied gases by laser impact on beryllium targets. *Journal of Applied Physics*, 39(9):4184–4189, 1968.

[16] P. E. Dyer, A. Issa, and P. H. Key. Dynamics of excimer laser ablation of superconductors in an oxygen environment. *Applied Physics Letters*, 57(2):186, 1990.

[17] J. M. Howe. *Interfaces in Materials: Atomic Structure, Thermodynamics and Kinetics of Solid-Vapor, Solid-Liquid, and Solid-Solid Interfaces*. John Wiley & Sons, Inc., New York, 1997.

[18] J. B. Baxter and E. S. Aydil. Epitaxial growth of ZnO nanowires on *a*- and *c*-plane sapphire. *Journal of Crystal Growth*, 274(3-4):407–411, 2005.

[19] P. Fons, K. Iwata, A. Yamada, K. Matsubara, S. Niki, K. Nakahara, T. Tanabe, and H. Takasu. Uniaxial locked epitaxy of ZnO on the a face of sapphire. *Applied Physics Letters*, 77(12), 2000.

[20] C. R. Gorla and N. W. Emanetoglu. Structural, optical, and surface acoustic wave properties of epitaxial ZnO films grown on $(01\bar{1}2)$ sapphire by metalorganic chemical vapor deposition. *Journal of Applied Physics*, 85(5):2595–2602, 1999.

[21] I. Ohkubo, A. Ohtomo, T. Ohnishi, Y. Mastumoto, H. Koinuma, and M. Kawasaki. In-plane and polar orientations of ZnO thin films grown on atomically flat sapphire. *Surface Science*, 443(1-2):L1043–L1048, 1999.

[22] B. P. Zhang, K. Wakatsuki, N. T. Binh, N. Usami, and Y. Segawa. Effects of growth temperature on the characteristics of ZnO epitaxial films deposited by metalorganic chemical vapor deposition. *Thin Solid Films*, 449(1-2):12–19, 2004.

[23] S. P. Chang, S. J. Chang, Y. Z. Chiou, C. Y. Lu, T. K. Lin, C. F. Kuo, H. M. Chang, and U. H. Liaw. ZnO epitaxial layers grown on nitridated Si(100) substrate with HT-GaN/LT-ZnO double buffer. *Journal of Crystal Growth*, 310(2):290–294, 2008.

[24] M. A. Herman, W. Richter, and H. Sitter. *Epitaxy: Physical Princilples and Technical Implementation*. Springer-Verlag, Berlin, Heidelberg, New York, 2004.

[25] H. Luth. *Solid Surfaces, Interfaces and Thin Films*. Springer-Verlag, Berlin, Heidelberg, New York, 4th, edition, 2001.

[26] T. Okada, K. Kawashima, and M. Ueda. Ultraviolet lasing and field emission characteristics of ZnO nano-rods synthesized by nano-particle-assisted pulsed-laser ablation deposition. *Applied Physics A*, 81(5):907–910, 2005.

[27] I. Ozerov, A. V. Bulgakov, D. K. Nelson, R. Castell, and W. Marine. Production of gas phase zinc oxide nanoclusters by pulsed laser ablation. *Applied Surface Science*, 247(1-4):1–7, 2005.

[28] S. Choopun, H. Tabata, and T. Kawai. Self-assembly ZnO nanorods by pulsed laser deposition under argon atmosphere. *Journal of Crystal Growth*, 274(1-2):167–172, 2005.

[29] M. Yan, H. T. Zhang, E. J. Widjaja, and R. P. H. Chang. Self-assembly of well-aligned gallium-doped zinc oxide nanorods. *Journal of Applied Physics*, 94(8):5240–5246, 2003.

Chapter 3

Experimental System Setup and Specifications

3.1 Deposition System

The thin film and nanostructure experiments were all preformed in a state-of-the-art, stainless steel chamber with approximately 50 L of volume space. The system also included a 4 L load-lock chamber with its own pumping system which allowed for the loading and unloading of samples without breaking vacuum in the main chamber. The two chambers were separated by a gate valve suitable for a 10^9 mbar pressure differential. See Figure 3.1 for an image of the PLD system configuration (or previous diagram in Figure 2.1. The main growth chamber was specifically designed for complete control over growing on any size substrate up to a diameter of 7.62 cm. The details and specifications of the system are outlined in this chapter.

3.1.1 Ultra High Vacuum System

Each chamber had both its own turbomolecular pump and a dry-running, i.e. oil free, backing pump. The pressures were monitored by a Pirani gauge (for

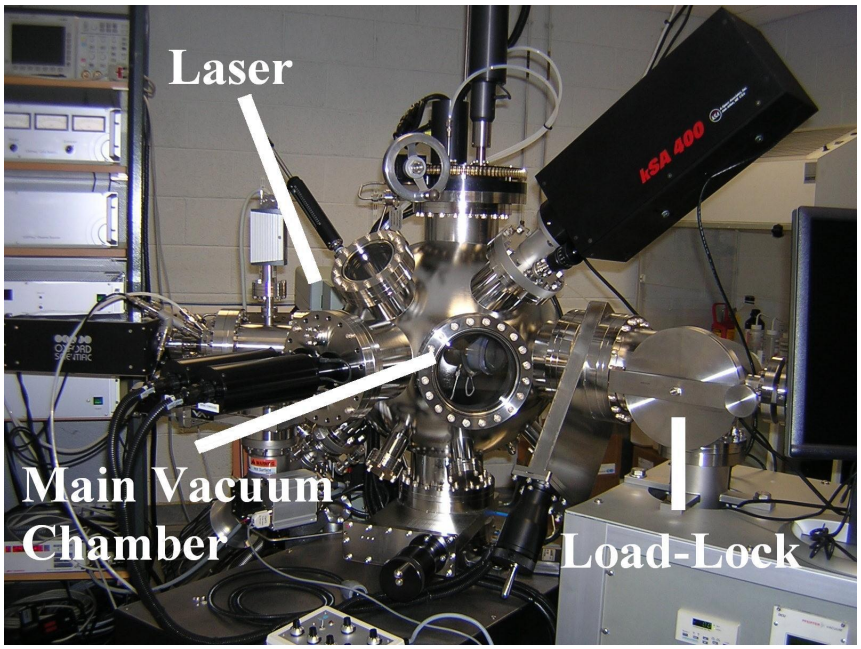

Figure 3.1: Configuration of the pulsed laser deposition system. The main deposition chamber is in the middle with the smaller load-lock chamber to the right (separated by a gate valve). The laser for the system, slightly seen, is behind the main chamber.

the range between atmospheric pressure to 10^{-3} mbar) and a compact full-range cold-cathode gauge (pressures down to 10^{-9} mbar). The turbomolecular drag pump for the main growth chamber evacuated gas at a rate of 500 L/s and would reach a pressure in the 10^{-7} mbar range from atmosphere within 30 minutes time. After approximately 12 hours it would reach pressures in the 10^{-8} mbar range and after approximately 24 hours it would reach its maximum base pressure of approximately 1.5×10^{-8} mbar when pumping from atmosphere. If pumped down after growth in gas pressures as high as 10^{-1} mbar, then the pressures would reach the low 10^{-7} mbar range within 30 minuets and attain its base pressure after 6-8 hours . As for the adjacent load-lock chamber, its turbomolecular pump evacuated gas at a rate of 60 L/s and would evacuate the chamber to a pressure in the 10^{-8} mbar range. This was sufficient enough to open the load-lock gate between chambers to allow for substrate transfer.

3.1.2 Substrate Heating Unit

The substrate heater was a unit located in the centre of the growth chamber which was fully rotatable (around a horizontal plane) by and external gear system. The unit can be seen through a port window in Fig 3.1, but a close-up view is shown in Figure 3.2. The unit was specially designed with an intricate

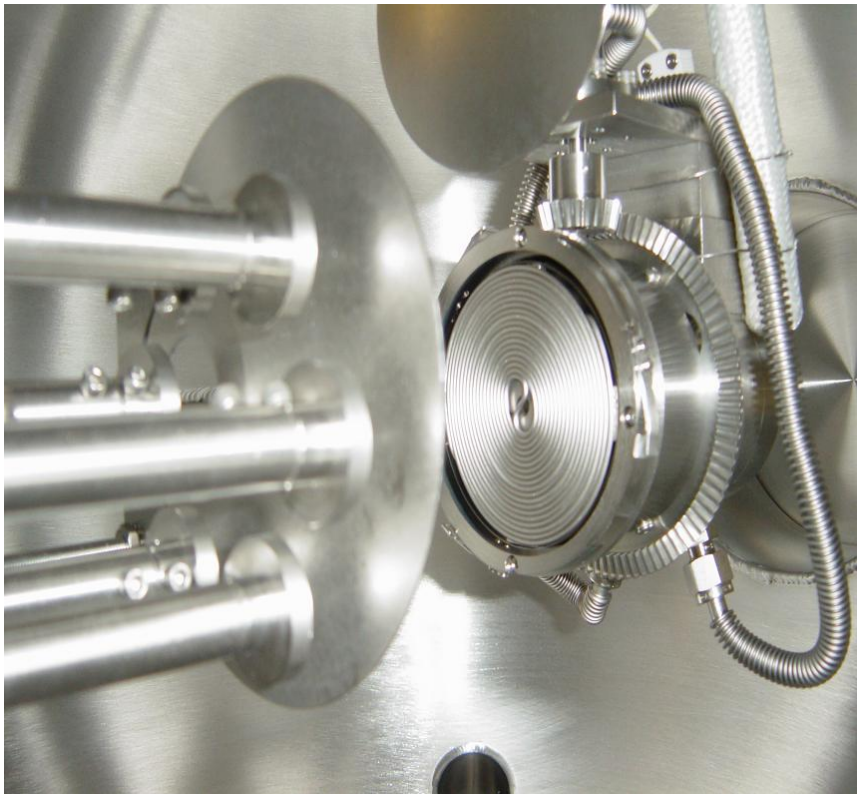

Figure 3.2: A close-up image of the heating unit and coils (without the nickel substrate disc). The target carrousel and shield can be seen on the right hand side.

substrate mounting system on top the thermal heating coil. The substrate mounting system was a circular disc of pure nickel with 6 evenly spaced notches around its circumference. The gear system allowed for the entire unit to be rotated into alignment with the load-lock chamber, where an extendable arm with three prongs would hold the nickel disc on three alternating notches. When the adjoining load-lock gate was opened and the arm was fully extended,

the nickel disc was then aligned with three more alternating prongs on the heating unit that fit into the 3 remaining empty notches on the substrate disc; thus, the substrate was mounted without breaking vacuum. After the disc was transferred to the heating unit, the unit was manually rotated into a position such that the substrate surface was perpendicular to the plasma plume's expansion for growth. Additionally, the heating unit itself was also rotatable about this perpendicular axis via computer-driven software at any chosen velocity.

The heating coil was controlled with a digital control unit and was designed to reach a maximum temperature of 1050 °C. However, due to both the nickel plate and adhesive silver paste used to affix the substrates, there was a large thermal loss. This was observed when the displayed value was compared to readings taken from a pyrometer. For clarity, throughout this thesis the temperature values read off of the system display will be used. This is also to avoid any confusion for future students who may refer to this work while using that particular system. The graph of the measured temperatures is shown in Figure 3.3. It shows both the measured values as the unit heated and as it cooled down at a rate 5 °C/min. The centre, edge, and substrate temperature curves were measured at those locations on the nickel disc (as the centre was visibly the hottest, followed by the edge of the disc, and then the measured temperature of the substrate. Respectively, the temperature curves of these regions deviate further from that of the displayed temperature, as would be expected.

3.1.3 Target Carrousel

The targets chosen to be ablated are placed inside the chamber on a target carrousel. The carrousel is picture in Figure 3.2 from the backside, and an image of it facing the target and shield is shown in Figure 3.4. The carrousel was another specially designed piece of machinery that allowed either six 1 inch

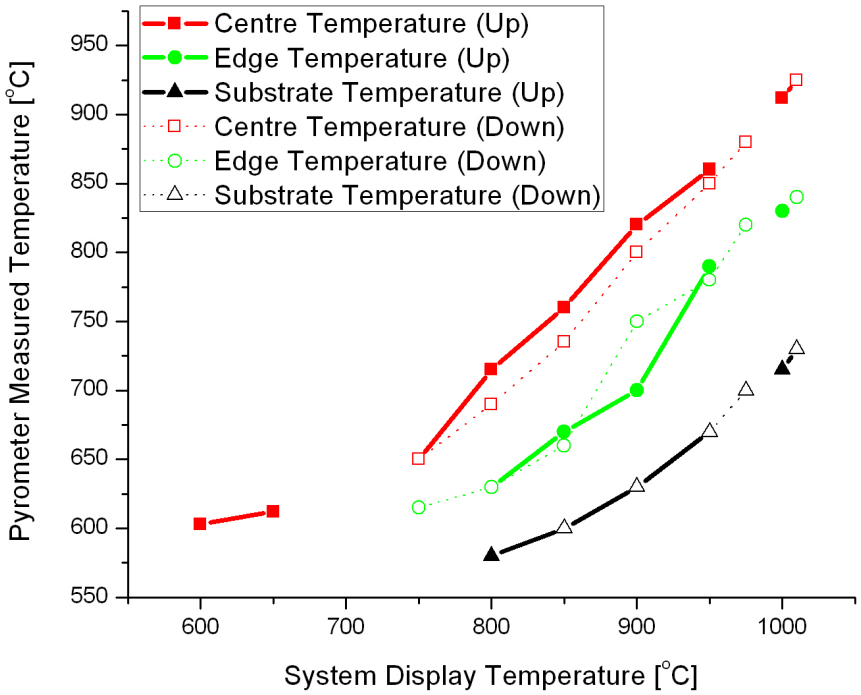

Figure 3.3: A graph of the measured temperatures with a pyrometer versus the temperature displayed by the system heating unit. The temperatures were measured at the centre and edge of the nickel substrate disc, and additionally the temperature of a sapphire substrate was measured. The solid lines represent the measurements as the unit was heated, and the dashed lines as the unit cooled at a rate of 5 °C/min.

diameter targets (or three 2 inch diameter targets if one so chooses) to be held in the chamber at any given time without breaking vacuum. All targets used were 25.4 mm diameter in order to maximise the number of usable targets at any given time. Six evenly spaced posts extend from the circumference of a large rotatable gear, as on a carrousel. The targets were each mounted on the ends of a post, and when loaded into the chamber, the principal (chiefly ZnO) target was directly in front of the substrate heating unit. This target would also be aligned with the laser to allow a forward-expanding to deposit directly

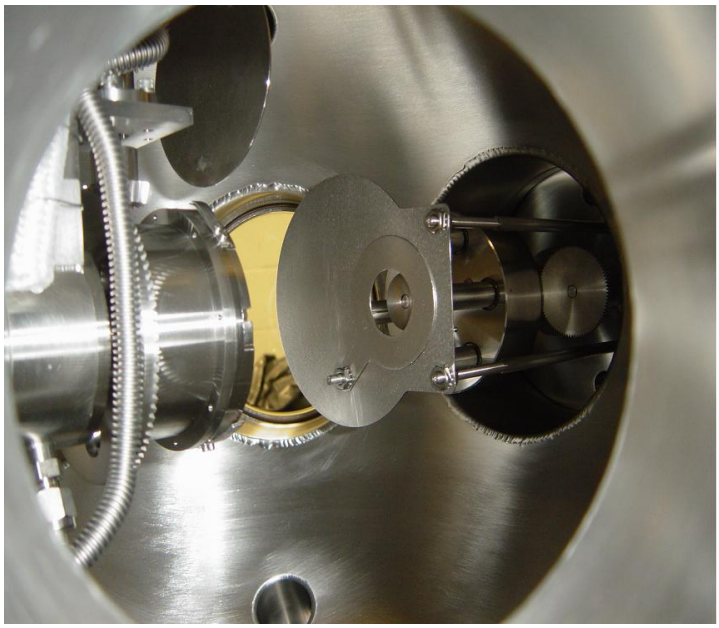

Figure 3.4: Image of the target carrousel as viewed down the path of the laser beam. One sintered ZnO target is seen in the image and the remaining 5 posts for other possible targets are hidden behind the protective shield.

onto the substrate surface. In addition to the rotation of these six posts about the centre of the gear, each of the posts themselves rotated about the axis of the post, both of which were controlled through computer software.

The above two motions, in turn, gave the substrates two possible independent degrees of rotation during ablation: (1) rastering, which was the rotation of the six posts about the centre of the carrousel, and (2) target rotation, which was simply the rotation of the target about the axis of the post. When ablated by a laser, rastering alone, created an arclike pattern on the target, whereas target rotation alone, caused a circular pattern on the surface of the target. When combined, a spirographic pattern was created, as intended, to evenly maximise the total usage of the target's surface area. Otherwise, the lifetime of the target would be greatly reduced, due to a target being ablated constantly over the same repeating pattern or even more so while remaining steadfast.

Additionally, a shield device could be manually lowered into the path of the plume expansion. This shield was used to block the substrate from unwanted deposition while any preliminary work was being done during a pre-ablation stage, eg. checking laser fluence is stable, adjusting pressure, etc.

3.2 Laser and Optics

The laser used for all experiments was a Surelite III solid state, frequency-quadrupled, Nd:YAG laser. The laser had a fundamental beam with a wavelength of 1064 nm that could be used as-is, or could be passed through a series of harmonic oscillators and dichroic mirrors to achieve different wavelengths: frequency-doubled (λ = 532 nm), frequency-tripled (λ = 355 nm), and frequency-quadrupled (λ = 266 nm.) In all experiments, the 266 nm wavelength was used. An image of a ZnO plume expanding into an oxygen background gas towards a substrate is show in Figure 3.5

A solid state laser was chosen due to its steady shot-to-shot energy output. This energy was monitored using a power meter type and had a measured energy output of approximately 140 mJ over the unfocussed beam of 7 mm diameter, yielding a fluence of 0.36 J/cm^2. This laser also had a short pulse duration of 6 ns which was favoured over a longer one due to the lesser interaction time with the target surface; this ensures a more rapid transition from a solid state into a plasma state. The laser beam was focussed down with a fused silica, plano-convex lens (f = 100 cm) directly towards the target. There was a measured loss in beam energy of approximately 15.4% from the laser to the target from absorption due to the lenses, mirrors, and chamber window. The target and laser were in fixed positions away from each other with an adjustable focussing lens between. With the focal point of the beam positioned well behind the target, this placed the target in a slightly defocussed region. Depending on the desired fluence, the lens was adjusted to the appropriate dis-

Figure 3.5: An image of an expanding ZnO plume into oxygen towards a substrate affixed to the heated nickel substrate disc. A reflection of the laser light off of the target onto the nickel disc is also shown.

tance from the target. From the simply geometry of our system, we would use the following equation to set the position of the lens, d, away from the target position:

$$d = f - \frac{f}{y}\sqrt{\frac{E}{\pi F}} \tag{3.1}$$

where y is the radius of the lens, E is the energy output of the laser, and F is the desired fluence. The spot size diameter of the slightly defocussed beam range would decreased from approximately 2.5 mm to 1.1 mm for increasing fluences of 1.0 - 5.0 J/cm^2 for $f = 100$ cm lens and $\lambda = 266$ nm laser light.

3.3 Targets and Substrates

3.3.1 Zinc Oxide Target

For all experiments, zinc oxide was the main growth material used as a target. The zinc oxide was sintered into a solid, 1 inch diameter ceramic disc with a high-purity standard of 99.999%. The four leading typical contributing impurities, as determined by the manufacturer, were: lead (at 4 ppm), cadmium (at <2 ppm), arsenic (at <1.5 ppm), and aluminium (at <1 ppm). Whenever the main growth chamber was exposed to the atmosphere, a 5 minute cleaning with the laser running at 10 Hz was used to ablate any contaminants that might have adhered to the surface of the target.

3.3.2 Substrates

For most of the work done in this thesis, sapphire (Al_2O_3) was the chosen substrate to grow on mainly for its similar 'hexagonal' structure to that of ZnO. The Al_2O_3 can be cut specifically (professionally cut) in such a way where the normal to the surface had a particular orientation. Three main orientation, or 'cuts', of sapphire were used in this work. They were: a-cut sapphire (a-Al_2O_3), c-cut sapphire (c-Al_2O_3), and r-cut sapphire (r-Al_2O_3). The orientation of each of these cuts were respectively along the $[11\bar{2}0]$, $[000l]$, and $[1\bar{1}02]$ directions.

Other than those cuts of sapphire, additional work was carried out on either cleaved pieces of a standard silicon Si(100) wafer or standard amorphous soda-lime glass.

Each of the mentioned substrates were single-side polished with a factory-quoted RMS surface roughness of 0.5 nm with the exception, of course, of the glass. Prior to deposition, each substrate was first degreased in acetone in an ultrasonic bath for 15 min, dried off with dry-N_2, then cleaned in isopropanol

(IPA) for 15 minutes in an ultrasonic bath, and finally, dried again with dry-N_2. The substrates would then be affixed to the nickel substrate disc using UHV-compatible silver paste. The disc was then heated to approximately 200 °C for 1 hour in order to dry the paste, which prevented much outgassing from the paste when under vacuum.

3.4 Ambient Growth Environment

For all experiments, 3 types of gasses were used: oxygen, nitrogen, and argon. The oxygen used was highly pure (99.999%) and was for the most part mainly used as an ambient background gas during growth. In other situations, either nitrogen (99.999% pure) or argon (99.99% pure) were used. All gasses enter the system through stainless steel piping, and the flow rates are independently controlled. When venting the main chamber (or the load-lock chamber), nitrogen was used to raise the pressure to atmosphere.

Chapter 4

Growth Characterisation Techniques

In this chapter, the collection of data from the various characterisation devices used throughout this thesis as well as the analysis of said data will be explained and discussed. All samples, once grown in the PLD system, are removed and stored in a dry air desiccating cabinet until characteristic measurements are later carried out *ex-situ*. These main techniques of structural, morphological, and optical measurements are discussed below along with example models as needed for future referencing.

4.1 X-Ray Diffraction

X-ray diffraction (XRD) was a characterisation technique used on all samples throughout this work to structurally analyse the crystallography of either the grown film or the substrate since the x-rays completely penetrate the samples. A 4-circle diffractometer (D8 Advance by Bruker AXS) was used with an emitting Cu K_α wavelength of $\lambda = 0.154$ nm. The 4 circular ranges of motion are in the 2θ-θ, ω, ϕ, and χ planes, as shown in Figure 4.1 [1].

The combined motions in the 2θ-θ-plane and ω-plane produce a scan com-

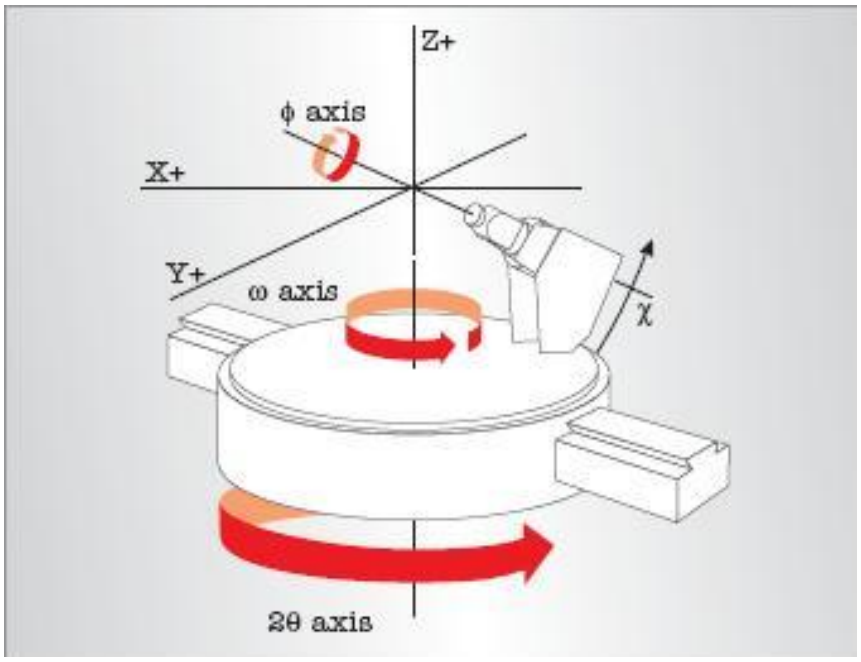

Figure 4.1: Diagram of the 4-circle ranges of motion for the x-ray diffraction system: 2θ-θ, ω, ϕ, and χ [1].

monly called a '2θ-ω scan' which indicate all crystalline peaks of both the grown material and the substrate crystal on which it was grown. Another scan that gave insight into the epitaxial growth of materials on top of substrates was the 'ϕ-scan': a scan where the sample is moved to a particular χ position and rotated about the ϕ-axis. After separate ϕ-scans for both the substrate and film were produced, the scans can then be compared to show how the lattice structure of the material grew on that of the substrate.

With the deposition of ZnO thin films and nanostructures, the basic, yet predominant underlying study was about the crystalline structure that was being grown as more and more material was deposited onto a substrate with each plume. As the material is deposited onto the substrate surface and subsequent ZnO layers, individual adatoms, whether single atoms, ions, or molecules, diffuse across the surface and eventually begin to cluster together in some fashion with individual alignment orientation. ZnO typically prefers to align itself in

the [000l] directional orientation (i.e. perpendicular to the (000l) planar surface) as mentioned in Chapter 1. If it were allowed, under perfect conditions, a 2θ-ω scan would detect an intense peak located at 34.42° with its (0004) reflection located at 72.56°. In other words, in this case, each ZnO cluster (whether an individual adatom or cluster of a nucleation site) with its own alignment eventually settled in perfect alignment with every other ZnO species which diffused across and settled onto the surface. A simplistic representation of this is shown in Figure 4.2.

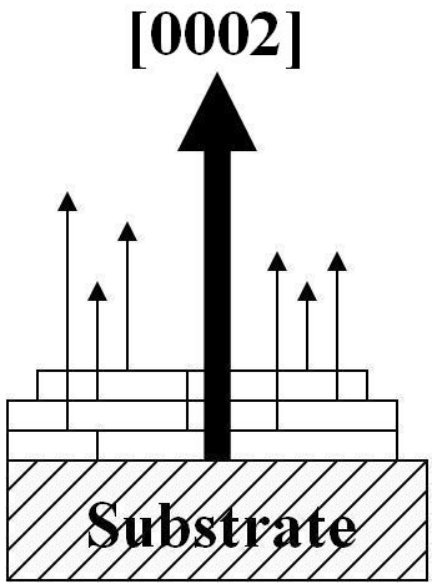

Figure 4.2: Diagram showing perfect alignment of a ZnO film grown in the c-axis direction on a substrate.

This, likely is never the case, so we can then say that, as a film develops over time, the bulk crystallinity of the overall film or nanostructure is determined by how well these individual crystallites are aligned in a particular growth direction to each other. This, then, gives information on how a film grows under specific growth conditions. An example of such a 2θ-ω scan for a ZnO film grown on each of the three sapphire substrate cuts is shown in Figure 4.3. All 2θ-ω scans were done over the range of 25° and 75° since the majority of

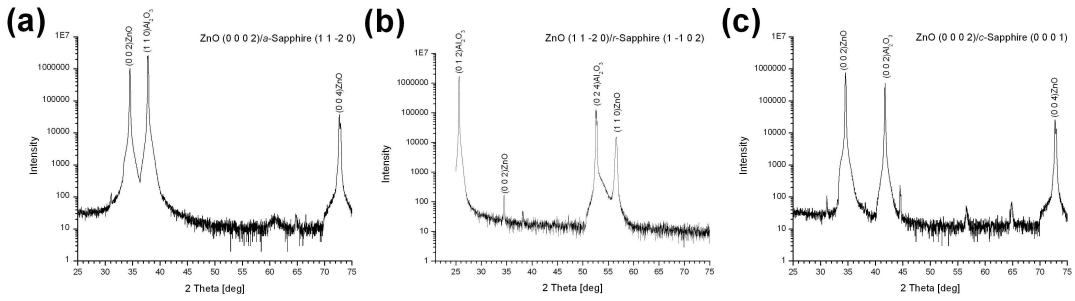

Figure 4.3: Example of a 2θ-ω scan of ZnO grown on (a) a-cut sapphire, (b) r-cut sapphire, and (c) c-cut sapphire. The typical ZnO and sapphire planes detected in a scan are labeled correspondingly and were obtained as part of this work.

the ZnO peak intensities and some of its reflections fall within this region.

From the 2θ-θ scan, the positions of peaks denoting crystalline material were each noted and a θ-scan (more conventionally known as a 'rocking curve') was then preformed. In the rocking curve scan, the source is fixed and the detector is scanned around the θ position determined from the 2θ-θ data. As an example, the rocking curve of a reference sample of bulk crystal ZnO is shown in Figure 4.4.

This information was used to as a way to discuss the crystalline structure of the grown material. The broadness or narrowness of this curve was measured in the standard way of measuring the full-width of the peak at half of the maximum (FWHM), which was approximately 0.016 ° for that of bulk ZnO. A broader peak, i.e larger FWHM value, means the the crystallites throughout the material are less aligned in orientation than a more narrow peak. Only peaks of significantly oriented, crystalline material would be present with a moderate to sharp curve above the background noise of the scan.

A film can be comprised of many crystallites detected with the 2θ-θ scan, thus making the bulk material crystalline, but the independent crystallites might not necessarily be oriented in the same direction. In this case, any peaks that might be present will just be washed out by noise or generally will produce

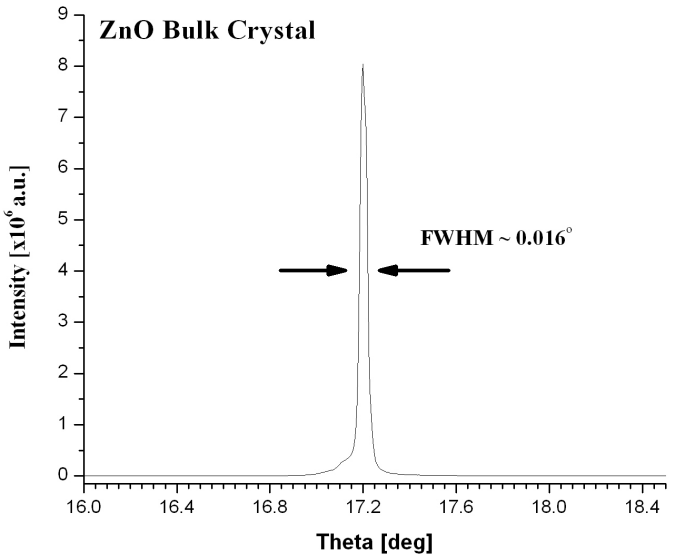

Figure 4.4: X-ray diffraction rocking curve (or θ-scan) of a bulk ZnO substrate.

very broad curve. This would nearly be the opposite case to that seen in Fig 4.2. For example, each cluster of either adatoms or a nucleation site which came together in the same crystalline orientation are said to be aligned in that particular direction. An entire film of such domains could occur to be aligned in the same orientation as mentioned earlier; however, this does not mean that it is well aligned.

In Figure 4.5 we see the 'perfect case' in Fig. 4.5(a) from earlier, but in Fig 4.5(b) and (c) we see that the ZnO clusters can be aligned in the [0002] direction, but overall the film itself is not well aligned. For a *c*-axis ZnO film, the extreme possibility is that in a perfectly oriented crystal, the [0002] vectors of individual crystallite domains throughout the film have no angle of divergence from that of any other, as shown in Fig. 4.5(a). Therefore, all of the domains would be perfectly aligned and would yield one sharp peak under a rocking curve. Conversely, if these domains pack together with no given shape

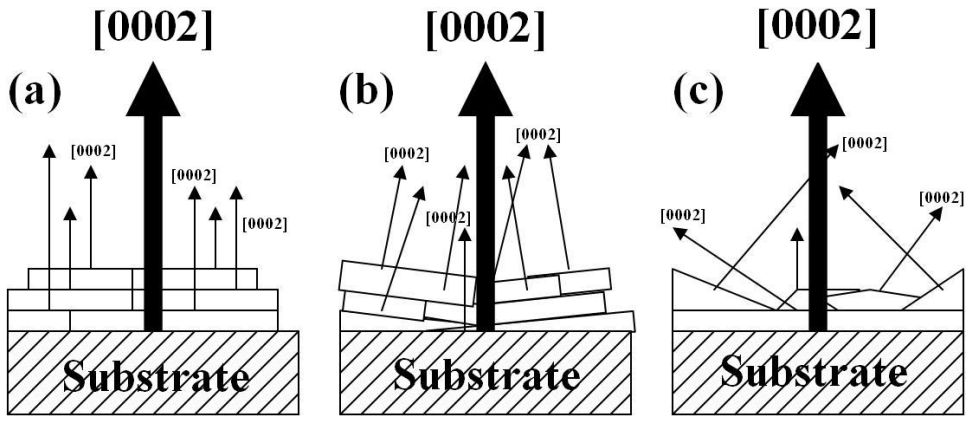

Figure 4.5: Image of ZnO, [0002]-oriented crystallites on a substrate. (a) again shows the perfect case scenario where the individual domains in the film are crystalline and the overall film is perfectly aligned. Both (b) and (c) show that the domains are also crystalline in the [0002] direction, however (b) shows a depiction of 'typical' alignment and (c) shows a poorly aligned ZnO film.

or order, the angles of divergence between any two of the normal vectors would be large, thus yielding a very broad shape for a rocking curve scan, as depicted in Fig 4.5(c). The FWHM of these rocking curves, then, are generally used as guideposts for the crystalline quality of our films.

Lastly, the epitaxial relationships between the substrates and the grown ZnO was checked with a ϕ-scan. The sample is moved to a χ-angle which has been calculated as the angle between the plane of the main crystalline growth peak of the material (determined in the 2θ-θ scan) and the plane of the most intense crystalline orientation of the material (so it's easily detectable); this is done for both the substrate and the ZnO separately.

For sapphire, the most intense crystalline orientation is listed as the $(10\bar{1}4)$ plane. The calculated χ-angles between this plane and the main growth plane for a-, r- and c-Al_2O_3 are 57.58°, 46.99°, and 34.32°, respectively. For ZnO, the most intense crystalline orientation is listed as the $(10\bar{1}1)$ plane. The calculated χ-angles between this plane and the (0002) and $(1\bar{2}0)$ ZnO planes

are, respectively, 61.59° and 40.37°. As an example, the diagram in Figure 4.6 shows the geometry for calculating the χ-angle for a c-cut sapphire substrate. In this image, the $(10\bar{1}4)$ plane is shown; it is around the normal to this plane, ie the $[10\bar{1}4]$ direction, that the 360° ϕ-scan is rotated. For each sample the ϕ-

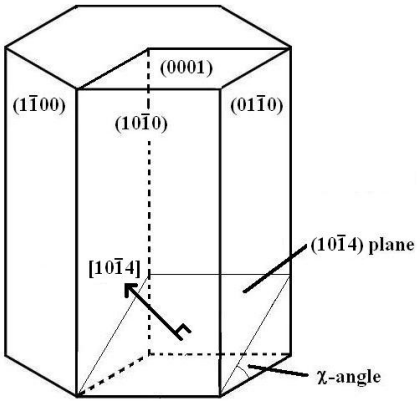

Figure 4.6: Configuration showing the χ angle between the basal plane of a c-cut sapphire substrate unit cell and the $(10\bar{1}4)$ plane which yields the most intense sapphire peak.

scan is taken for both the substrate and the deposited film, and this determines how the film is oriented on the substrate. In short, the ϕ-scans give the vector normal to the plane-in-question projected onto the base plane of the crystal. From these, we can then determine (1) whether or not the ZnO had grown epitaxially on the substrate and then (2) compare our epitaxial relationships to those calculated in literature, as listed in Chapter 2. It is later shown (and confirmed in literature) in §5.2.2 that we commonly find degrees of peak separation between the ZnO film and sapphire substrates. These typically are: (1) 8.5° separation between (0002)ZnO and a-Al_2O_3, (2) 4.4° separation between $(11\bar{2}0)$ZnO and r-Al_2O_3, and (3) a 30° separation between (0002)ZnO and c-Al_2O_3.

4.2 Scanning Electron Microscopy

The main instrument used to characterise the morphology of the sample surfaces was a scanning electron microscope, or SEM. From this imaging technique, the overall surface texture or structure can be observed and the widths of such structures can be measured. A sample SEM image ZnO grown on gold islands is shown in Figure 4.7. The SEM is an instrument in which a beam of

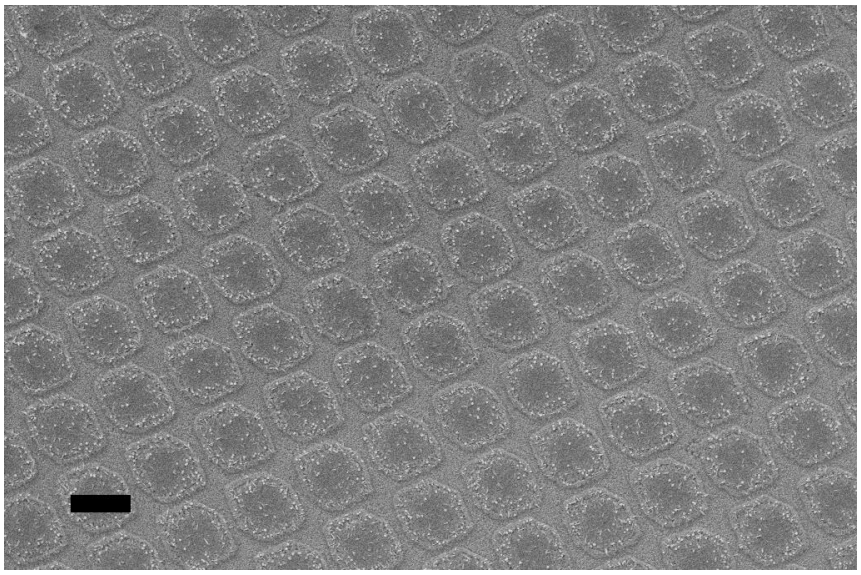

Figure 4.7: Sample SEM surface image of ZnO grown on top of gold islands on an a-Al_2O_3 substrate. The black scale bar is equal to 10 microns.

electrons, which scan repeatedly across the surface of a sample under vacuum, are thermionically emitted from a tungsten filament. The electrons would then backscatter from the observed area of the sample and this was detected and converted into an optical image [2]. This imaging process allowed for direct physical comparison between samples, mainly those involving nanostructured growths. In the case of high-resolution SEM (HR-SEM), samples were initially coated with a few angstroms of gold.

This scanning microscope is a technique to gain a 'true', or unprocessed, view of sample surfaces due to local variations of the electron emissivity of the

surface [2]. As the device images the surface, it is produced as a 2D interpretation of the surface, therefore no depth information can be determined for samples where holes, valleys or edges are present, particularly with nanostructured films. However, the sample can be tilted to give a faux-3D representation of the surface. Sometimes two unavoidable side-effects of working with the SEM are vibrations and straying. At times, natural vibrations of the system can sometimes cause lines in the images, more prevalent under higher magnification. Straying can also occur due to samples slightly moving or vibrations which cause some images to appear skewed or oblong.

When manually focusing on the surfaces of sample for imaging, it is easier to adjust the resolution by finding edges or debris on the surface. Typically, if the surface is nanostructured, there is hint of this from lower magnification, however at times it is hard to determine, especially for smooth films, so the aid of debris was used. Generally debris ablated from the sintered target is uncommon, but there is a negligible amount on the surface and it can be used to magnify and focus. In the cases of the thin films later mentioned in §5.1, this debris is present in the images, not because it is commonly strewn about the surface, but only to resolve any nanometric surface features.

4.3 Atomic Force Microscopy

A second imaging technique, atomic force microscopy (AFM), was used to characterise samples both physically and optically. Converse to SEM, this imaging technique does not produce a 'true' image of the sample surface, but a virtual, processed one. From this imaging technique, the width and height information about any structures on the sample surface can be quantitatively measured with surface profiles. Additionally the roughness of the surface can be analysed. A sample AFM image of a nanopyramid along with a profile scan is shown in Figure 4.8.

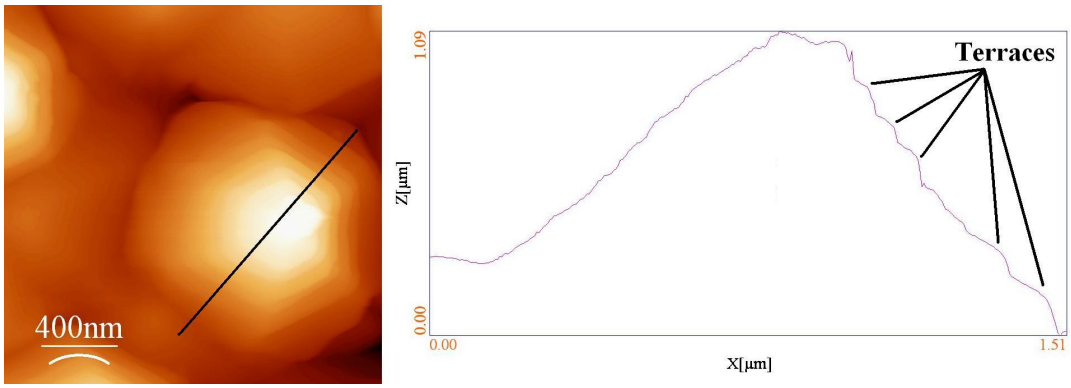

Figure 4.8: Sample AFM image of a ZnO nanopyramid (left) and a linear surface profile (right) as shown as a black line on the AFM image. The terraces of the nanopyramid can be seen in the AFM image and on the line profile.

The AFM has a vast array of possible ways one could analyse the surface of a sample, but only three were used in this work. The first two are called static and dynamic modes, or otherwise known as scanning mode and tapping mode, respectively. For both modes, a topographical 'map' of the surface is produced. The third is called a phase scan which can be used to determine variation between materials on a scanned surface [3].

For all three modes, an atomically sharp tip with a nominal tip radius of 7 nm, had been factory-made to sit on the end of a larger cantilever which was attached to an even larger mount, all of which is etched from a single piece of silicon nitride about 1 mm $\times$ 2 mm. This entire piece would be placed on a piezoelectric crystal, which was software controlled, and lowered down to only a few angstroms above the sample surface.

Under scanning mode, the atomic tip is attracted to the surface atoms due to van der Waals forces as the piezoelectric crystal traces the tip back and forth across the sample. As the tip encounters any slopes, peaks, cliffs, etc., the tip would 'trace out' these motions all while in contact with the surface. At the same time a laser is focussed and reflected off of the tip of this cantilever which then records and converts these motions into the topography of the surface,

giving physical measurements of length, depth, heights, etc [4].

In tapping mode, however, the cantilever is set to oscillate at the resonant frequency of the tip. The tip then 'taps' across the scanned area under the same atomic repulsion principle, sending data back to the software about variations in both the resonance frequency and phase due to the changes in the surface. As the oscillating tip comes across surface features, the oscillations will dampen. These changes in the resonant frequency are similarly recorded and converted into a physical topography of the scanned region [4].

For the majority of the samples which had nanostructured surfaces, AFM data was gathered. As mentioned, the resultant image morphology may not mirror that of one taken on the SEM. Some differences may be due to the tip itself as it passes over sharper edges and corners or over deeper features in the case of nanostructures. At times, the tip may possibly attract random atomic-sized material which adsorbs to the tip rather than the sample stuface, resulting in false images or images of repeating structures due to the material stuck to the tip.

Lastly, from time to time, samples were checked with a phase scan. In an SEM image, a questionable sample might appear to be only partially covered by ZnO leaving sections of substrate exposed. A phase scan detects changes in the tip oscillations, exactly as was done in tapping mode, however a change in the phase would indicate areas with more than one material due the difference in atomic repulsion for these different materials. As the cantilever passes over different materials in a phase scan, the lag in phase is recorded as it moves from one material to another. If the materials are different, different colour shades are imaged, otherwise, the phase image will be uniformly coloured. By checking the sample with a phase scan, we confirmed that all samples were completely covered with ZnO.

4.4 Photoluminescence

Photoluminescence (PL) is a technique used to measure the optical characteristics of a material. From this measurement technique, the optical quality of the material is measured as light emitted from the sample by illuminating it with an unfocused laser beam, in this case an unfocussed beam from a HeCd laser ($\lambda = 325$ nm) with 22 mW output. The photo-excited sample emits photons which are focused back into a 1 m grating spectrometer and collected by a photomultiplier tube in photon counting mode. The sample itself can be loaded into a vacuum chamber with the option of cooling the sample chamber down to 2 K with a closed cycle cryostat. The collected data will be displayed as peaks and bands over certain wavelengths. Depending on their location, information about excitonic emission, donor binding energies, and vacancies in the material can be determined by referencing to literature. For example, B.K. Meyer *et al.* is one such source, and examples of PL spectra for bulk ZnO at 4.2 K taken from this journal paper are reproduced in Figure 4.9 [5] as a reference.

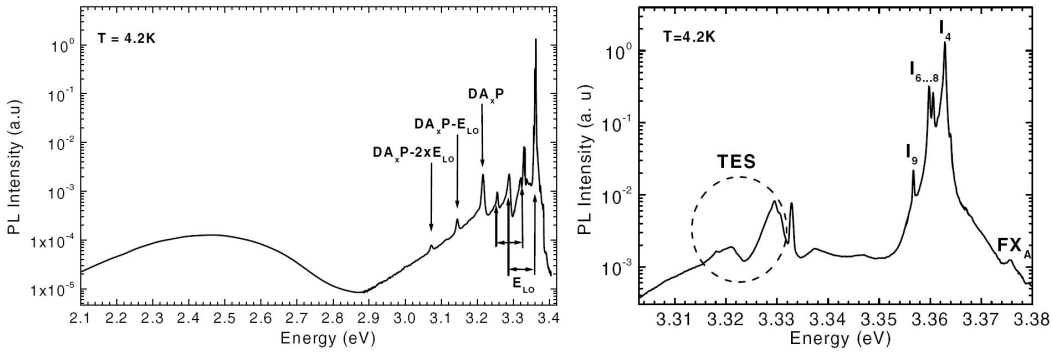

Figure 4.9: Example of PL spectra for bulk ZnO at 4.2 K taken by B.K. Meyer *et al.* [5]. In the left-hand image, typical excitonic, donor-acceptor-pair (DAP), deep-level emission, and corresponding phonon replica with longitudinal optical phonons (LO) are labeled. In the right-hand image, the two-electron satellite region is circled and the bound exciton lines (I_4 to I_9) are labeled along with the transversal free exciton (FX_A).

As ZnO is wide band gap material with a main luminescence peak around 365 nm (3.4 eV) at room temperature, all PL scans were taken from within the UV spectrum and through the visible, 350 - 600 nm. For collection, the increments were set to 0.5 nm and scanned for each at a speed of 2 sec. All scans were taken in a completely darkened room.

4.5 X-Ray Photoelectron Spectroscopy

X-ray photoelectron Spectroscopy (XPS) is a typically non-invasive technique to study the chemical composition of the surface and near-surface region of samples. With this analysis technique, photoelectrons from maximum depth of approximately 100 Å of the sample surface are detected after being excited by an x-ray source [4, 6]. Electrons are emitted from the core levels of the elements in the material and collected by a detector which can be used to determine the binding energies of the individual core levels on the surface. The number of electrons with a particular energy are counted and this data can then be deconvolved to fit reference peaks for the individual elements. The exact chemical nature of the materials can then be determined from both the binding energy positions of the peaks and from the integrated area under the curves, which gives information regarding the quantity of the material present [6].

The spectrometer used to collect the spectra is fitted with a standard Al K_α and Mg K_α twin anode x-ray source. The Mg K_α, with a photon energy of 1253.6 eV, was used for these experiments. The analyser pass energy was set at 20 eV with a step size of 0.1 eV and the dwell time was 0.2 seconds.

This technique was specifically used for the work on the samples later discussed in Chapter 6.

4.6 Raman Spectroscopy

Raman spectroscopy is a technique of detecting low-frequency vibrational modes in samples by exciting the sample material with laser light. A 'pseudo absorption' process is invoked where the difference between the incident and emitted radiation is equal to one quantum of vibrational energy. Alternatively, the molecular vibration is already in a higher state and, upon re-emission, photons of higher energy than the exciting energy result [4].

The micro-Raman system used (also specifically for work on the samples in Chapter 6) was in a back-scattering geometry using 325 nm HeCd UV laser excitation with a spot size of approximately 1 μm. The backscattered light is detected and any shift between the incident and returned light is measured. The resulting spectra displays the Raman shift as intensity peaks due to vibrational modes which are identified and compared to corresponding literature.

References

[1] C. F. Campana. Analytical application note: Single crystal diffraction, 2000. `http://www.bruker-axs.de/index.php?id=322`.

[2] H. Luth. *Solid Surfaces, Interfaces and Thin Films*. Springer-Verlag, Berlin, Heidelberg, New York, 4th, edition, 2001.

[3] M. A. Herman, W. Richter, and H. Sitter. *Epitaxy: Physical Princilples and Technical Implementation*. Springer-Verlag, Berlin, Heidelberg, New York, 2004.

[4] J. C. Vickerman. *Surface Analysis: The Principal Techniques*. John Wiley & Sons, Ltd., Chichester, West Sussux, 2007.

[5] B. K. Meyer, H. Alves, D. M. Hofmann, W. Kriegseis, D. Forster, F. Bertram, J. Christen, A. Hoffmann, M. Straßburg, M. Dworzak, U. Haboeck, and A. V. Rodina. Bound exciton and donor-acceptor pair recombinations in ZnO. *Physica Status Solidi (B)*, 241(2):231–260, 2004.

[6] J. B. Hudson. *Surface Science: An Introduction*. John Wiley & Sons, Inc., Troy, New York, 2008.

Chapter 5

Results & Analyses: Epitaxial Growth of ZnO

The laser-based growth techniques, pulsed laser deposition and laser molecular beam epitaxy (LMBE), have enjoyed great success in producing both high-quality epitaxial, thin films and nanostructured materials [1, 2]. In working with PLD to develop the growth of such high-quality ZnO thin films and nanostructures, the growth parameters for our system needed to first be explored and understood in order to manipulate and reproducibly fabricate high-quality material. When growing ZnO using pulsed laser deposition there are several important parameters that must be controlled during the entire process to achieve this high-quality. Depending on the combination of the variable parameters during deposition, the zinc oxide grows in either a 2D or 3D growth mode as discussed in §2.3.2. The majority of parameters produced, as it was found, 2D growth (i.e. thin films), and is where the foundation research for this work began. From this, we began to investigate how to gain control over the growth and development of ZnO to cross over into the 3-dimensional nanostructured regime.

In this chapter, we present our characterisation, analyses, an discussions of

the growth, development, and manipulation of zinc oxide deposited thin films and nanostructured material.

5.1 Smooth, Thin Films

The first work done in our new apparatus was to determine the effects a range of temperatures had on ZnO deposited films. This also required establishing a routine growth procedure for all future samples. Generally known growth conditions published in open literature, such as [3–5], for high quality films of ZnO were used as our starting point. As each apparatus configuration is different, so must the growth conditions. Therefore, we needed to first establish these conditions to suit our system. For these initial trials, silicon (100) was the first substrate of choice due to its availability then followed by deposition on more epitaxially suited sapphire.

5.1.1 Temperature Dependency: ZnO on Si(100)

Before loading any samples into the UHV system, all substrates were cleaned following the standard cleaning procedure previously mentioned in §3.3.2. It should be noted silicon surfaces naturally have thin oxide layer of SiO_2, approximately 2-3 nm thick, which is difficult to remove if the substrate is prepared *ex-situ* [6], so for convenience, the oxide layer was left for deposition. After the cleaned substrates were loaded, the chamber was evacuated down to base pressure. Then the substrates were heated to 850 °C at a rate of 11 °C/min for the sample presented here. This gradual heating was adopted partially to ensure a prolonged lifetime of the heating coil. After reaching the growth temperature, it became standard to allow the temperature to stabilise for 5 minutes, during which, the process gas was usually introduced. For this sample, the chamber was filled with O_2 ($pO_2 = 10^{-1}$ mbar). As the reactive, ambient gas pressure

stabilised, the laser energy was routinely stabilised and lens position was adjusted. In this case, the Nd:YAG laser beam was focused onto the ZnO target at a fluence of 2 J/cm^2 for 8 minutes of deposition at 10 Hz. After these 4,800 laser shots, the chamber pressure was immediately raised to 1/2 atmosphere of O_2 and the sample was annealed at 850 °C for 30 min. Afterwards, the sample was allowed to naturally cool down to room temperature.

The resulting morphology of the ZnO film deposited on a Si(100) substrate is presented in the SEM image in Figure 5.1. It can clearly been seen that the

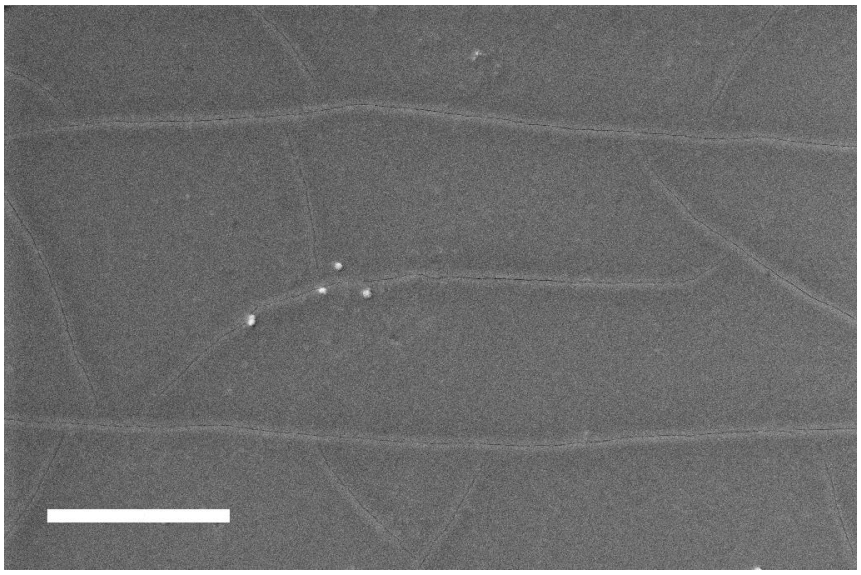

Figure 5.1: SEM image of a ZnO film on Si(100) substrate. Nanometric sized cracks on the surface are clearly visible (due to rapid cooling of the sample). The scale bar is 10 micron.

surface is cracked, but appears smooth and featureless otherwise. The speckles on the surface (approximately just under 0.5 micron in size) are debris which has landed on the surface during the ablation process. As was discussed in §4.2, the debris found on the surface assisted in resolving the image at higher magnifications to be sure the surface shows no presence of nanostructures. Since the debris is of submicron size, any possible nanometric surface features should be resolved while focusing on the debris. The cracks noted in the SEM image

were likely caused by the large amounts of stress which was relieved due to thermal contraction as it rapidly cooled (initially the temperature would drop from whatever the growth temperature to the 500-600 °C at a rate ranging from 500-1000 °C/min). Samples grown which cooled naturally after deposition from high temperatures were found to have cracked ZnO films.

To rectify the issue of cracked ZnO films, samples were grown under the same conditions, however they were slowly cooled from the growth temperature in the procedure down to 150 °C at a rate of 5 °C/min. All films grown with this slow-cooling process were found to be contiguous.

With an established growth routine, and the issue of cracked ZnO surfaces resolved with a slow-cooling procedure, we decided to determine a temperature suitable for growing crystalline ZnO films. From the literature, a majority did not produce ZnO nanostructures below 600 °C so we loosely defined this as a low growth temperature in our system. The maximum temperature our system was capable of was 1050 °C.

Another sample was grown on a Si(100)substrate at the lower temperature of 600 °C to compare it to the sample mentioned above grown at 850 °C. The system was slowly heated to 600 °C at a rate of 15 °C/min. All other conditions were the same. As with the sample grown at 850 °C, the resulting film was also found to be a featureless, thin film.

The XRD rocking curve analysis of the ZnO (0002) peak showed that the sample grown on Si(100) at 600 °C produced a very broad peak with a FWHM of roughly 7°. This indicates that the resulting ZnO film was weakly aligned. Comparatively, the sample grown at 850 °C was epitaxial, albeit poorly crystalline with a wide rocking curve of (1.2°). These XRD rocking curves are shown in Figure 5.2. Seemingly, the growth at 600 °C was too low a temperature for the film to properly align on the silicon substrate surface. This was more than likely due to the lack of epitaxy between the two materials and the associated large lattice mismatches noted in literature, eg [7, 8]. In order to

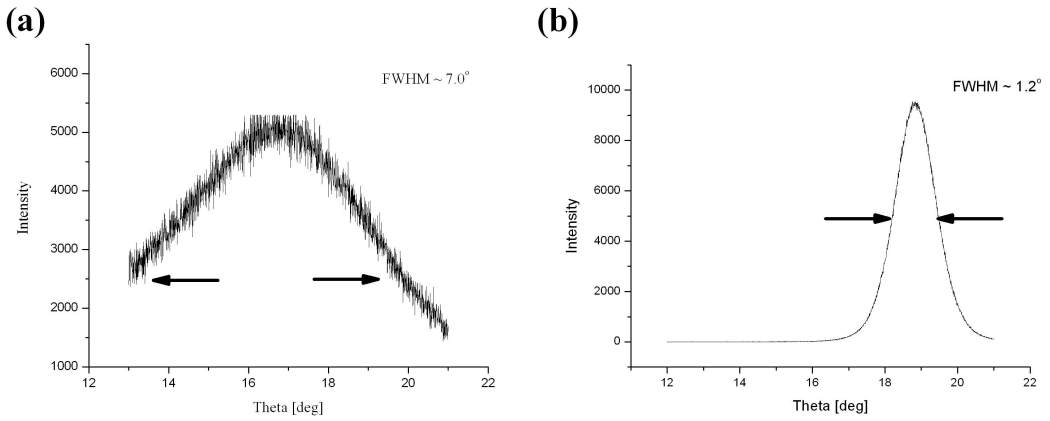

Figure 5.2: XRD rocking curve graphs of ZnO grown on Si(100) at (a) 600 °C and (b) 850 °C. For both samples, a laser deposited 4,800 shots (fluence of 2 J/cm^2) and were annealed for 30 min at 1/2 atmosphere of O_2. Following this, the sample in (a) was allowed to naturally cool down, whereas (b) was cooled at a rate of 5 °C/min.

improve upon this, we decided to (1) work with substrates which would allow epitaxial growth (using sapphire substrates) and (2) increasing the energy put into the deposition to assist ZnO align better (by increasing both the laser fluence and the growth temperatures).

5.1.2 Temperature Dependency: ZnO on Al_2O_3

We initially chose r-cut Al_2O_3 as a substrate which would allow epitaxial films of ZnO to grow. However, the favoured orientation is the $[1\bar{1}02]$ ZnO growth direction when grown on r-Al_2O_3. It was assumed that improved crystallinity on r-Al_2O_3 would also mean improved crystallinity for the (0001) ZnO peak on the a- and c-cuts of sapphire.

Thus, two ZnO films were grown on r-Al_2O_3 at 850 °C and 1050 °C with an increased laser fluence of 5 J/cm^2. All other growth conditions remained the same. Figure 5.3 shows the XRD rocking curve for the $(1\bar{1}02)$ ZnO peaks for these samples. Respectively, the FWHM of these curves were 0.47° and 0.70°, as compared to the FWHM value for bulk ZnO of approximately 0.016°

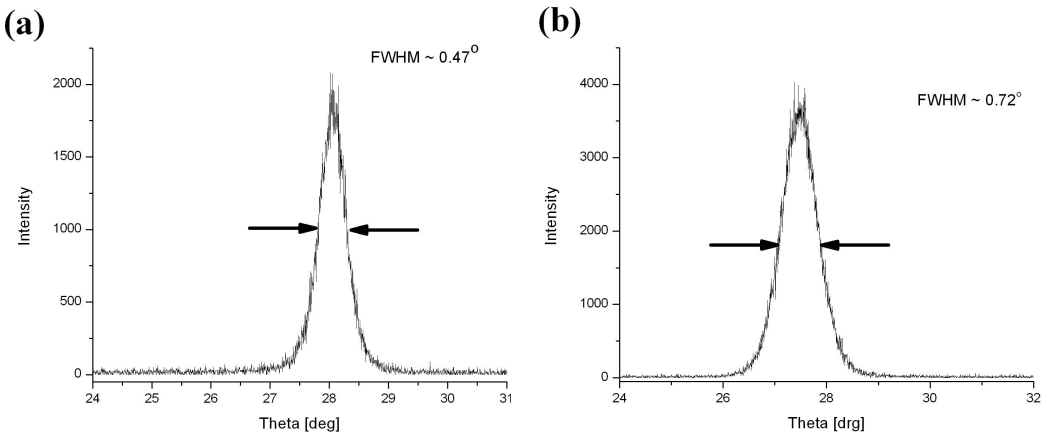

Figure 5.3: XRD rocking curve graphs of ZnO grown on r-Al_2O_3 at (a) 850 °C and (b) 1050 °C. For both samples, a laser deposited 4,800 shots (fluence of 5 J/cm^2) under 10^{-1} mbar of O_2. After deposition they were annealed for 30 min at 1/2 atmosphere of O_2 then slow-cooled to room temperature.

in §4.1. From this it was decided that temperatures around and above 850 °C favour the growth of crystalline ZnO in our apparatus.

SEM analyses revealed both samples had smooth ZnO surfaces with a possible hint of surface structure or texture, in particular the sample grown at 1050 °C (see Figure 5.4 however it is too unresolved to tell). AFM analyses of these two samples are shown in Figure 5.5. In Figure 5.5(a) striae are clearly running along the film; these are attributed to the fact that the c-axis of the ZnO lies within the r-cut sapphire substrate's plane. The rms roughness (ρ_{RMS}) of the surface was determined to be 3.9 nm. On the other hand, in Figure 5.5(b) clustered domains can be noticed across the surface in addition to the presence of a striated surface. For this sample surface, AFM analysis revealed $\rho_{\mathrm{RMS}} = 4.1$ nm. It is possible that those clustered domains account for the slight texture barely noticeable in the corresponding SEM image, and may also even account for the increased FWHM of the rocking curve angle in the $(1\bar{1}02)$ZnO reflection. Unlike smooth, thin films, ZnO adatoms were favoured

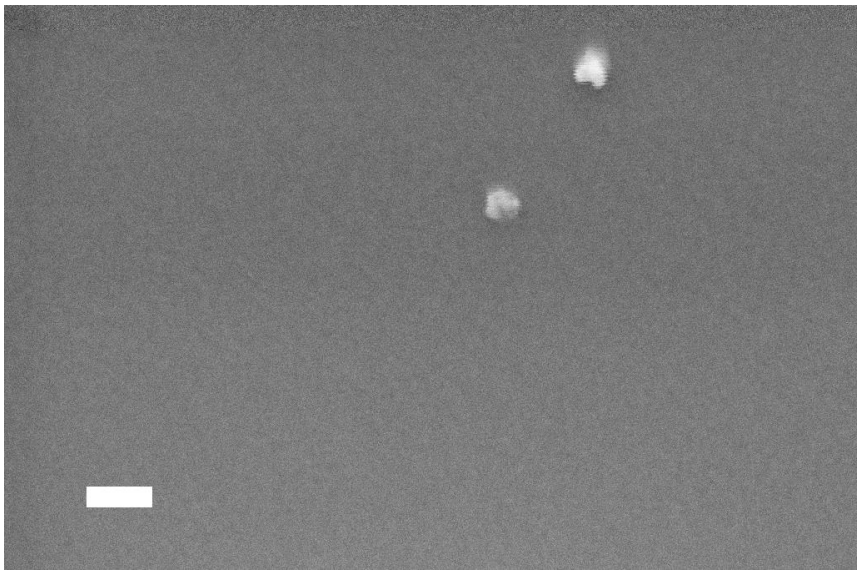

Figure 5.4: SEM showing ZnO grown on r-Al_2O_3 at 1050 °C with a laser fluence of 5 J/cm^2 under 10^{-1} mbar of O_2. The surface appears to be a smooth with the slightest hint of surface texture. Scale bar is equal to 1 micron.

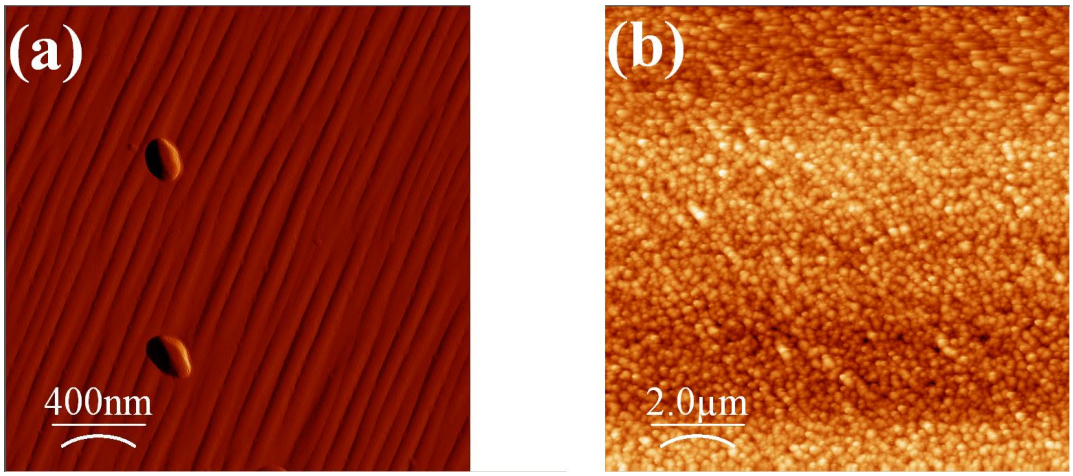

Figure 5.5: AFM showing ZnO grown on r-Al_2O_3 at (a) 850 °C and (b) 1050 °C, both deposited with a laser fluence of 5 J/cm^2 under 10^{-1} mbar of O_2. In (a) the surface striae of [0002]-ZnO as the c-axis of the r-Al_2O_3 runs along the surface of the substrate. For a less magnified view of the other sample shows in (b), the same striae can been seen.

to form into independent clusters or grains on the surface, with the possibility that these grains were aligning themselves irrespective to other such regions. We show in the following section evidence of these grains as the precursor to nanostructures.

5.2 Nanostructured Films

During initial growth depositions and procedural modifications, it was shown that a region of control over the crystalline structure of the ZnO film was established. All samples exhibited a smooth surface with the exception of the last sample mentioned in the previous section. From the possible evidence of nanoclusters, we decided to explore growth conditions close to this sample, as it was a possible precursor to nanostructured growth.

In this section we develop the work in determining the conditions needed to control the growth of ZnO from a 2D thin film into a 3D nanostructured one. Until now, growth conditions were formed under the idea that development of nanostructures on the sample surface would be influenced by the surface alone. We now decided to incorporate the idea that they might also develop during transport from the target to the surface, in particular using the lower laser fluence. In §2.3.3, it was discussed that the idea of in-plume crystallisation was becoming a topic of discussion in the open literature. Thus, the work detailed in this section was motivated by these works in order to necessitate nucleation sites due to in-plume nanoclusters, from which we can begin to develop a growth model.

5.2.1 Fluence Dependency

We decided to reduce the fluence to allow for possible in-plume nanocluster formation. The previous sample showed possible nanoclusters on the surface

and was grown on r-Al_2O_3 at 1050 °C ($pO_2 = 10^{-1}$ mbar, 4,800 shots, 10 Hz, 5 J/cm^2, and 1/2 atm O_2 post-anneal). A similar sample was grown with the same condition except for a lower laser fluence of 2 J/cm^2.

The resulting nanostructured surface can be seen in the SEM image in Figure 5.6. X-ray analysis determined the FWHM of the rocking curve of the

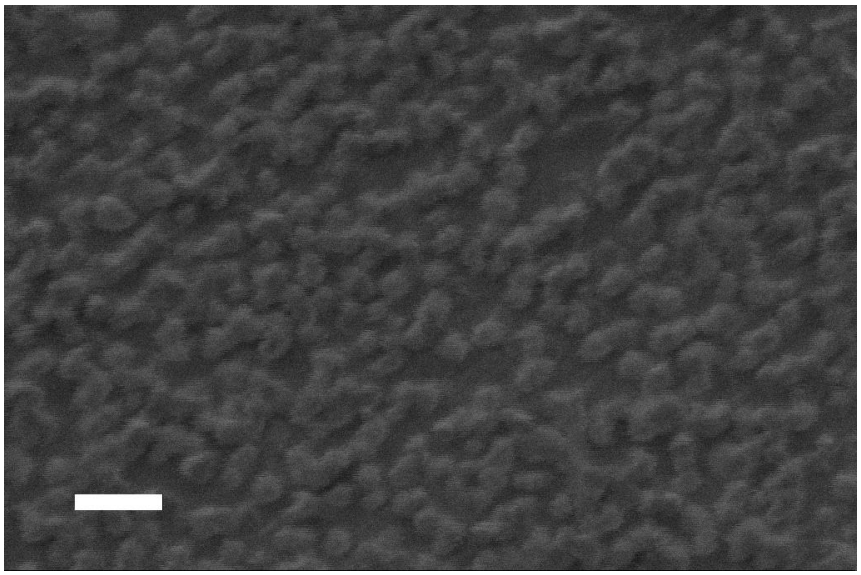

Figure 5.6: SEM showing ZnO grown on r-Al_2O_3 at 1050 °C with a laser fluence of 2 J/cm^2 under 10^{-1} mbar of O_2. Scale bar represents a length of 1 micron.

$(1\bar{1}02)$ZnO peak was (0.36°) as compared to the previous sample FWHM of (0.70°). AFM analysis determined the surface roughness increased from 4.1 nm to 95.0 nm for the samples grown at 5 J/cm^2 and 2 J/cm^2, respectively. The AFM surface scan of the sample grown at 2 J/cm^2 can be seen in Figure 5.7.

It is believed that the decrease of energy in the plume during transport allows for the molecules to condense before reaching the surface [3, 9]. There is a definite nanostructured texture to the surface as observed in the AFM images of these two samples, Figures 5.5(b) and 5.7. The AFM surface roughness data indicates a significant increase in surface area, likely attributed directly to the

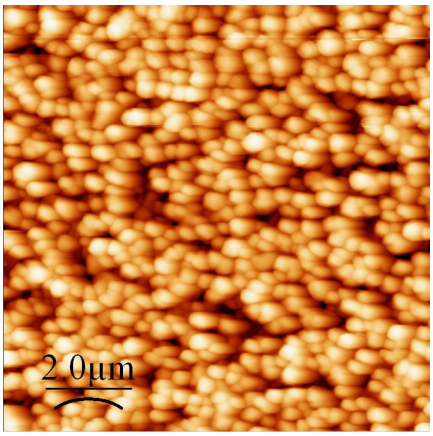

Figure 5.7: AFM showing ZnO grown on r-Al_2O_3 at 1050 °C with a laser fluence of 2 J/cm^2 under 10^{-1} mbar of O_2.

presence of nanostructures on the ZnO surface. The presence of nanostructures warrants more surface area since flatter structures are more 2D than 'rougher' 3D structures. Lastly the XRD also shows improved alignment indicating that any molecules, atoms, an ions diffusing on the surface, were more stable and aligned. This threshold from a 2D surface to a 3D one, was crossed by reducing only the laser fluence.

It is proposed that this follows in accordance to current literature regarding in-plume nanocluster formation, eg [3, 10]. These pre-formed nanoclusters arrive at the surface as larger pre-aligned adatom, sometimes called and adparticle, adhering to similar adparticles diffusing across the surface. As these are larger than they normally would be without forming in-plume, they have already each become a nucleation site which was pre-aligned in the plume. Additionally, as these clusters form in-plume, they are not bound by the constraints of surface forces, therefore they should logically have a more favourable chance of self-aligning than they would on the surface. These larger nucleation sites would likely have a greater chance of attracting any smaller particles that approach the surface with a greater potential energy, which would, in turn, allow for more complex growth modes to occur such as island or SK-growth

modes.

5.2.2 Substrate Dependency

It was decided to expand growth of ZnO on other cuts of sapphire, namely a-Al_2O_3 and c-Al_2O_3 substrates, and to further test and analyse the properties of these nanostructures. In keeping with the same growth conditions that yielded nanostructures on r-Al_2O_3, samples were grown on both a-Al_2O_3 and c-Al_2O_3. Further analyses were also carried out on the successful growth of nanostructures found on the r-Al_2O_3 sample.

Both the SEM and AFM images display the surface morphology for these samples in Figure 5.8. The surface imaging data displays that ZnO film grown on a-Al_2O_3 had hexagonally shaped nanodots with a typical size of 300 nm. The corresponding sample on r-Al_2O_3 had also produced nanostructures with a typical size of 300 nm, yet they were aggregated nanostructures with irregular, oblong shapes. ZnO films grown on the c-Al_2O_3 were isolated nanodots with a typical size of 150 nm. The AFM figures in Figure 5.8(a)-(c) revealed these nanostructures had typical heights of 100 nm, 300 nm, and 40 nm. Additionally, AFM phase scans were taken for each sample and revealed that the smooth areas between the nanostructures were also comprised of ZnO. This is in agreement with described 'wetting' layers by other authors [3, 9, 11] which occur for growth modes such as Stranski-Krastanov. The surface imaging shows hexagonal shaped nanostructures, albeit misshapen, for these samples all grown under 75 mTorr of oxygen pressure.

All three of these samples, which were good benchmark examples for XRD on the corresponding cuts of Al_2O_3, displayed the typical 2θ-θ scans of ZnO on their respective substrates, show in Figure 5.9. Figure 5.9(a) displays the three main crystalline peaks of that of ZnO on a-Al_2O_3: the peak seen centered at 37.78° is the position of the a-plane-oriented sapphire and the peaks centered

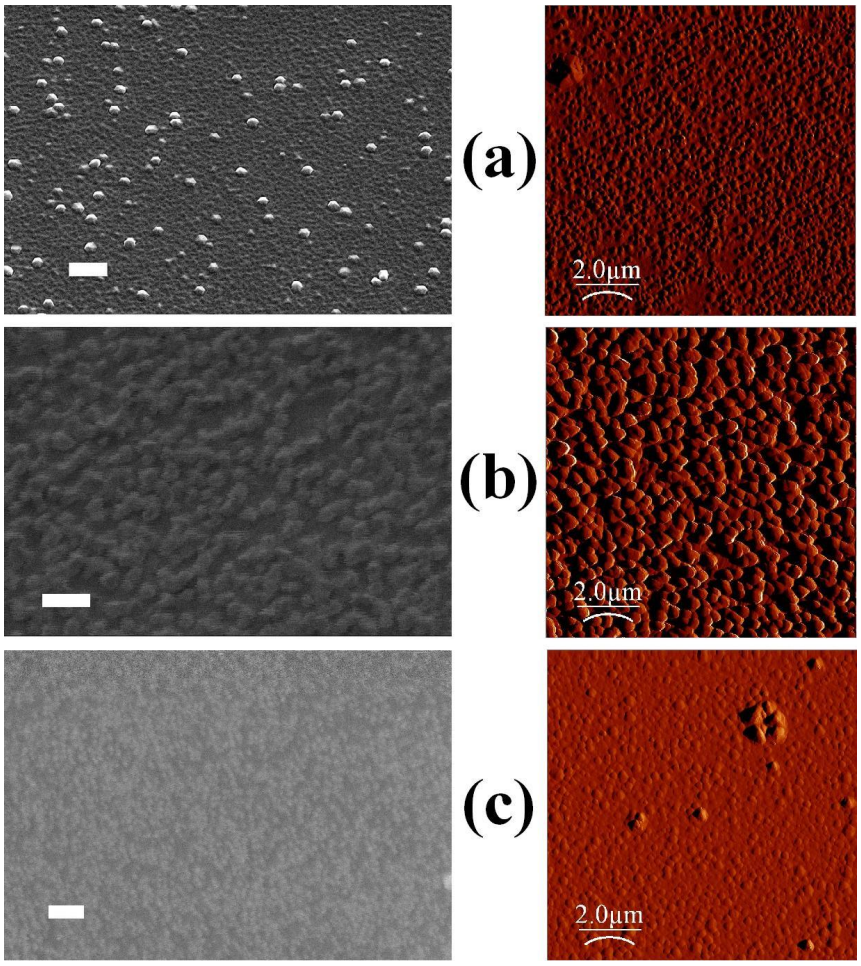

Figure 5.8: Image of SEM (left column) and AFM (right column) scans for ZnO grown on (a) a-Al_2O_3, (b) r-Al_2O_3, and (c) c-Al_2O_3 substrates. All three sample films were deposited at 1050 °C with a laser fluence of 2 J/cm^2 (4,800 shots) under 10^{-1} mbar of O_2. The scale bars for the SEM images depict 1 micron, and those for the AFM depict 2 micron.

around 34.42° and 72.56° are respectively the positions of the (0002)ZnO and it's (0004)ZnO reflection. Similarly, Figure 5.9(c) displays the same ZnO peaks and also the c-plane cut peak for the c-Al_2O_3 at 41.68°. As the c-axis runs along the surface of r-cut sapphire substrates, XRD results are slightly different. Figure 5.9(b) shows a typical 2θ-θ for ZnO on r-Al_2O_3 with the $(01\bar{1}2)Al_2O_3$ peak and it's $(02\bar{2}4)Al_2O_3$ reflection located respectively at 25.58° and 52.55°. The main ZnO peak typically grown on c-Al_2O_3 is the $(11\bar{2}0)$ZnO peak centered

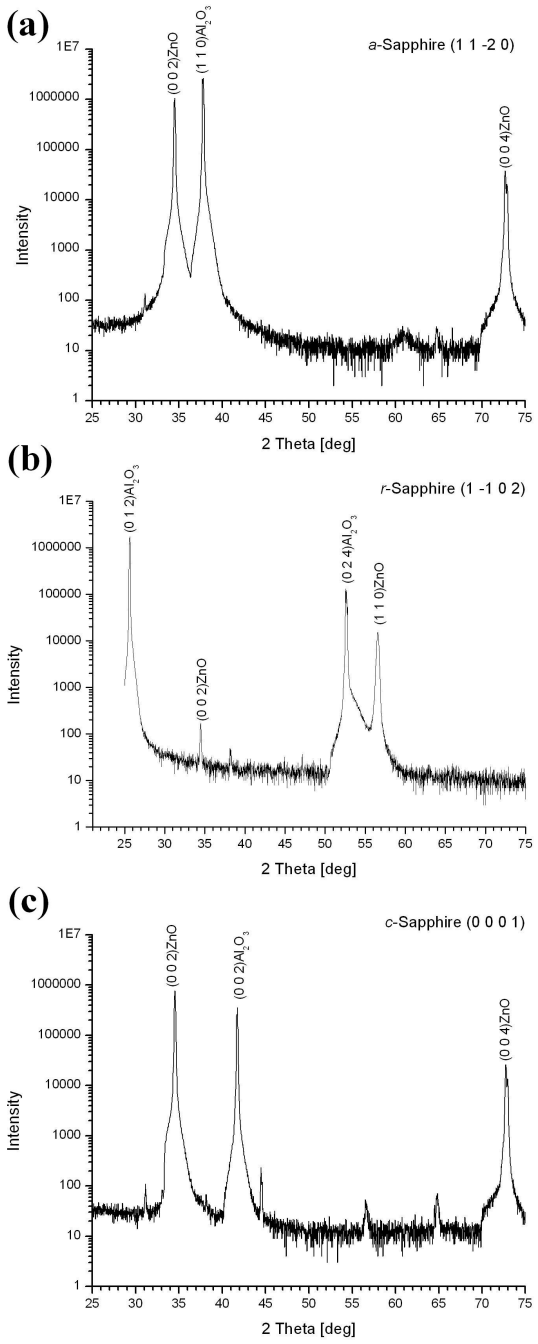

Figure 5.9: X-ray diffraction 2θ-θ scans showing the typical peak positions of all samples throughout this work for ZnO grown on (a) a-Al_2O_3, (b) r-Al_2O_3, and (c) c-Al_2O_3. These scans directly correlate to samples presented in Figure 5.8(a-c).

at 56.60° and sometimes the c-axis ZnO peak presents itself as it was in this particular film. From this XRD data, it is apparent that the ZnO nanodots grown on the a- and c-Al_2O_3 are both c-axis oriented.

The θ-scans for the (0002) rocking curve for the ZnO nanostructured, thin films grown on the a- and c-Al_2O_3 substrates were respectively found to have FWHM of 0.15° and 0.21°. The FWHM of the $[11\bar{2}0]$ZnO rocking curve for the film grown on r-Al_2O_3 was determined to be about 0.36°.

X-ray diffraction ϕ-scans were also performed on these three samples; these ϕ-scan seen in Figure 5.10 are also benchmark examples of most ZnO films grown on the respective cuts of sapphire substrates. The first of these was the ZnO grown on an a-Al_2O_3 substrate. In Figure 5.10(a), a combined image of the ϕ-scan of the a-Al_2O_3 and the ZnO ϕ-scan. Typically only two main peaks present themselves for the a-Al_2O_3 at 180° separation whereas, for the ZnO film, a typical 6 peaks present themselves with 60° separation. Due to the lattice mismatch between the (0001)ZnO and $(11\bar{2}0)$ sapphire planes, typically an 8.5° shift occurs between the closest two peaks. This corresponds to the epitaxial relationships $(0001)_{\mathrm{ZnO}} \parallel (11\bar{2}0)_{\mathrm{sapphire}}$ and $[11\bar{2}0]_{\mathrm{ZnO}} \parallel [0001]_{\mathrm{sapphire}}$ mentioned previously in Chapter 2.

The second ϕ-scan seen in Figure 5.10(b) is of ZnO on r-Al_2O_3. Typically, the Al_2O_3 ϕ-scan has two peaks separated by approximately 93°. The ZnO ϕ-scan shows two sets of peaks with the closer two separated by 85°; the two peaks in each set are themselves separated by 180°. These ϕ-scans correspond to the epitaxial relationships $(11\bar{2}0)_{\mathrm{ZnO}} \parallel (01\bar{1}2)_{\mathrm{sapphire}}$ and $[0001]_{\mathrm{ZnO}} \parallel [0\bar{1}11]_{\mathrm{sapphire}}$.

Lastly, Fig 5.10(c) show the typical ϕ-scans of c-Al_2O_3 and as-grown ZnO film. The Al_2O_3 displays three peaks each 120° apart and the ZnO displays six peaks each 60° apart. The ZnO and Al_2O_3 peaks are typically separated by 30° and yield the mentioned epitaxial relationships of $(0001)_{\mathrm{ZnO}} \parallel (0001)_{\mathrm{sapphire}}$ and $[1\bar{2}10]_{\mathrm{ZnO}} \parallel [1\bar{2}10]_{\mathrm{sapphire}}$.

Additional the optical properties of the ZnO films were checked for these

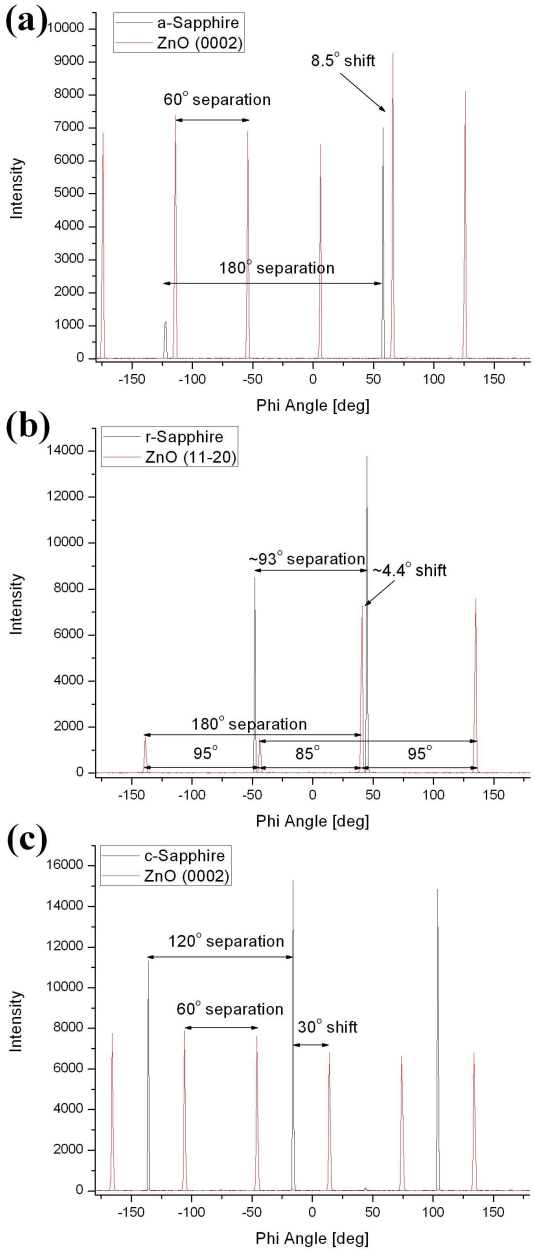

Figure 5.10: X-ray diffraction ϕ-scans for ZnO films (red) grown on (a) a-Al_2O_3, (b) r-Al_2O_3, and (c) c-Al_2O_3 substrates (black). These scans were collected as detailed in §4.1 and directly correlate to samples presented in Figure 5.8(a-c) and 5.9(a-c).

three samples with laser-excited photoluminescence at both room temperature and at 7 K, as shown in Figure 5.11(a). PL done for samples later presented in this thesis were typically similar to the data presented here. The a- and

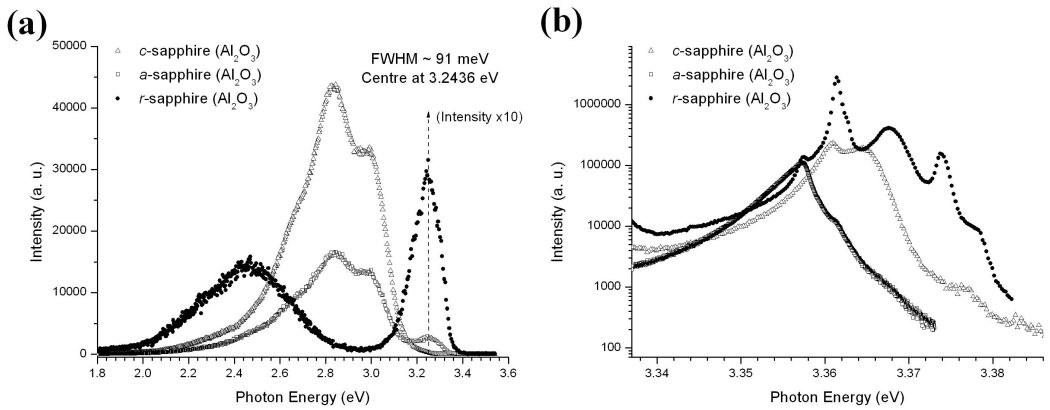

Figure 5.11: Photoluminescence spectra for ZnO films on a-, r, and c-cut sapphire substrates taken at (a) 300 K and (b) 7 K. In (b), the features for ZnO on r-Al_2O_3 are detailed in the following Figure 5.12.

c-sapphire substrates produced very similar patterns, with broad blue bands centered around 2.85 eV (435 nm). A small amount of near-band edge emission at 3.24 eV was also present for the samples grown on a-Al_2O_3. On the other hand, the ZnO thin films grown on r-Al_2O_3 substrates showed an intense free exciton peak centered at 3.24 eV photon energy with a full-width half-maximum of 0.09 eV and a broad green band centered around 2.45 eV normally associated with deep (oxygen vacancies) levels [12]. The blue band observed for the ZnO thin films grown on the a- and c-sapphire substrates has been reported by a few authors, for example [13], and its origin appears to be unknown. Low temperature spectra (at 7 K) are presented in Figure 5.11(b) and show the characteristic excitonic emission features [12], testifying to the high optical quality of the as-grown ZnO films produced in this research. In accord with the room temperature data, the ZnO/r-Al_2O_3 spectrum stands out in this respect. The photon energies of the band maxima are located at 3.3573 eV, 3.3609 eV, and 3.3614 eV for the samples grown on a-, r-, and c-sapphire, respectively. Details of the ZnO/r-Al_2O_3 spectrum are presented in Figure 5.12 and both our measured peaks and the assigned peaks referenced from B.K. Meyer *et*

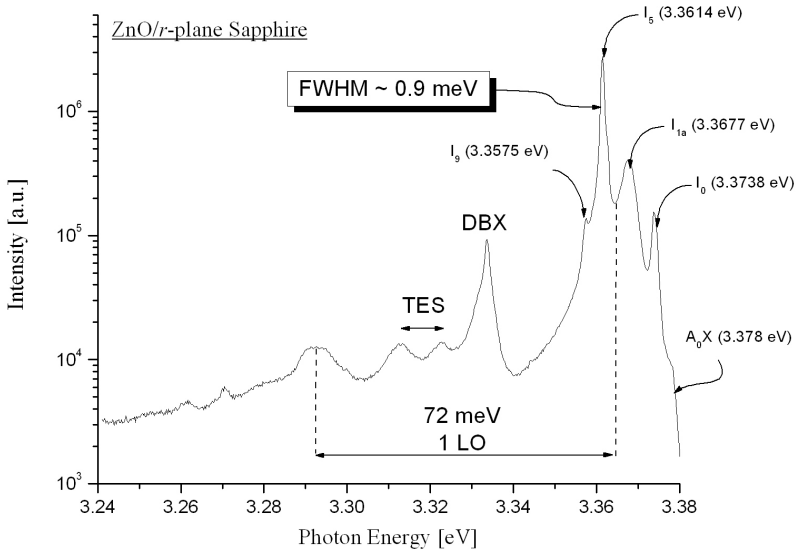

Figure 5.12: Expanded photoluminescence spectrum for ZnO film on an r-cut sapphire substrate taken at 7 K (from Figure 5.11). The high optical quality of the ZnO grown is shown. The donor-bound exciton, the two-electron satellites, and the first longitudinal optical phonon replica are apparent and labeled DBX, TES, and 1 LO respectively on the figure [12].

al. [12] are provided in Table 5.1.

The high optical quality is indicated by the 0.9 meV width of the I_5 line, the presence of the free exciton line FE(A), the longitudinal optical (LO) phonon replica of the original donor bound excitons and the two-electron satellites (TES) peaks, respectively.

5.3 Nanostructures

As shown in the previous sections, zinc oxide with quality crystalline structure and optical properties had been produced for both smooth and nanostructured thin films on various substrates. Our next motivation was to further enhance

Line	Energy [eV] as measured	Energy [eV] as assigned [12]
FE(A)	3.3780	3.3772
I_0	3.3738	3.3725
I_{1a}	3.3677	3.3674
I_5	3.3614	3.3614
I_9	3.3575	3.3567

Table 5.1: Table of peak lines determined from photoluminescence spectrum taken at 7 K of ZnO deposited on r-Al_2O_3 as shown in Figure 5.12 and the corresponding line assignment as given my Meyer *et al.* [12].

and control the growth of nanostructures. To do this, modifications needed to be made to growth procedures that could directly effect formation of proposed nanoclusters in the plume. However, without means of physically detecting such in-plume particles, logical changes needed to be made to the growth procedures that could indirectly evidence possible presence of such clusters. The three main changes which we explored were: increase in thickness of the deposited film, increase of ambient pressure, and change of ambient gas during growth.

5.3.1 Film Thickness & Growth Pressure

The decision was made to increase the number of shots from the previous 4,800 (8 min at 10 Hz) to 18,000 (30 min at 10 Hz). The number of ablationshots was increased to surpass an initial wetting layer in depositing a thicker film. These might have been seen in the previous nanostructured surfaces, as discussed later. For this particular set of samples, we increased the oxygen pressure during ablation to 3.5×10^{-1} mbar (approximately 4 times that of all previous samples mentioned) to assist in decreasing the mean free path of the ZnO

species traveling towards the surface.

A set of samples were grown in the same run on three different substrate cuts, *a*-, *r*-, and *a*-Al_2O_3. The cleaned and loaded substrates were raised to a temperature of 950 °C at a rate of 11 °C/min and the chamber was filled from base pressure to 3.5 $\times$ 10^{-1} mbar of oxygen. ZnO was then deposited for 25 min at 10 Hz (at 266 nm) with a fluence of 2 J/cm^2. (Normally the deposition time would be the mentioned 30 minutes, but for this set of samples, an extra 5 min was needed at the start to stabilise the laser.) After deposition, the oxygen pressure was raised to 1/2 atmosphere and slow cooled at the rate of 5 °C/min.

The SEM surface imaging is shown in Figure 5.13. The SEM analyses displayed densely packed ZnO nanostructures across the substrate. The nanostructures found on *a*-Al_2O_3 are vertical columns with no typical hexagonal shape. The majority of those grown on the *r*- and *c*-Al_2O_3 substrates also have no apparent shape, however, some definite, well-defined, hexagonal columns can be found scattered across the surfaces. Since all three samples were grown simultaneously and since *a*-Al_2O_3 and ZnO have a closer epitaxial relationship, it is somewhat surprising since that no hexagonal shaped structures were observed. The nanostructures grown on *a*-Al_2O_3 are in the range of 0.75 - 1 microns wide, whereas the width of the those grown on the other two cuts of sapphire have a wider range of 0.5 - 1 μm.

XRD analyses showed that ZnO/*a*-Al_2O_3 aligned itself in the typical (0002) plane and had a rocking curve FWHM of 0.17° centered at 17.2° (see Figure 5.14(a)). The ZnO/*r*-Al_2O_3 sample displayed 2 peak formations of ZnO in the typical [11$\bar{2}$0] direction (Figure 5.14(b) and also in a weak [0002] orientation (Figure 5.14(c)). The (11$\bar{2}$0) peak was 100 times more intense than that of the (0002) peak. The FWHM and centre positions of the rocking curves were respectively 0.30° at 27.8° and a broad 1.5° at approximately 17.0°. The broad rocking curve peak of the (0002) peak was likely due to the weak intensity from

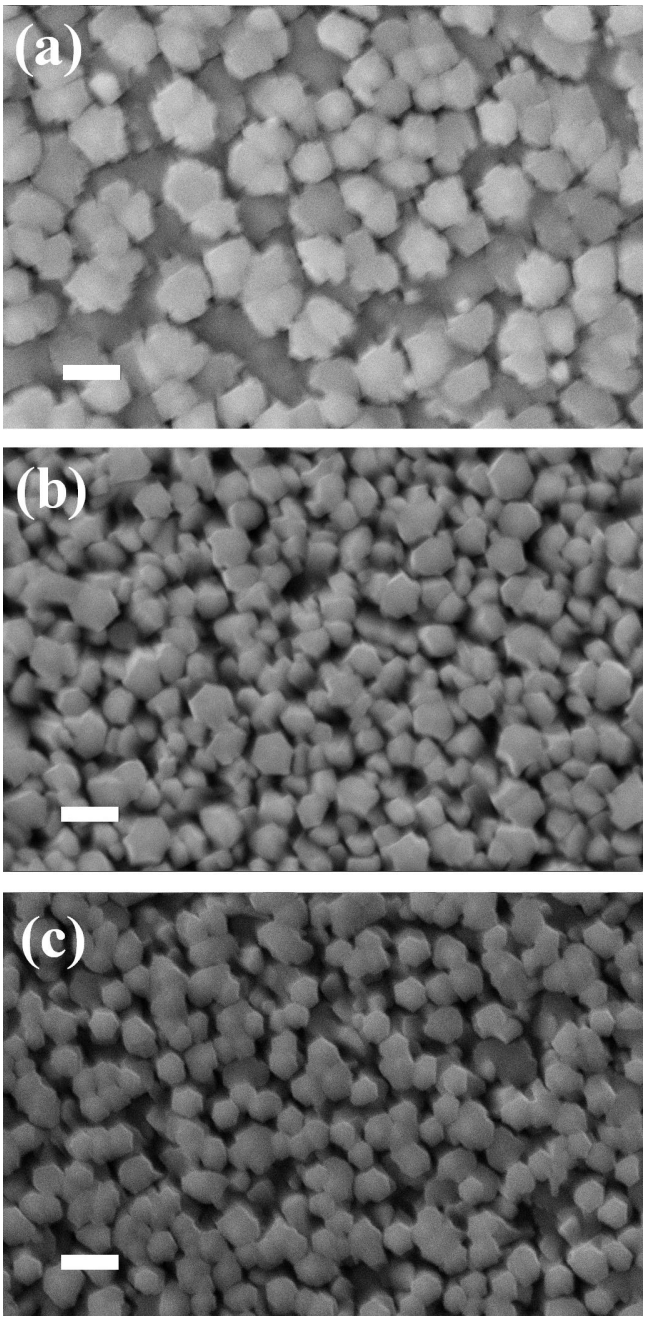

Figure 5.13: SEM images of ZnO grown on (a) a-Al_2O_3, (b) r-Al_2O_3, and (c) c-Al_2O_3 substrates deposited at 950 °C with a laser fluence of 2 J/cm^2 under 3.5 $\times$ 10^{-1} mbar of O_2 for 18,000 pulses. Scale bar represents 1 micron.

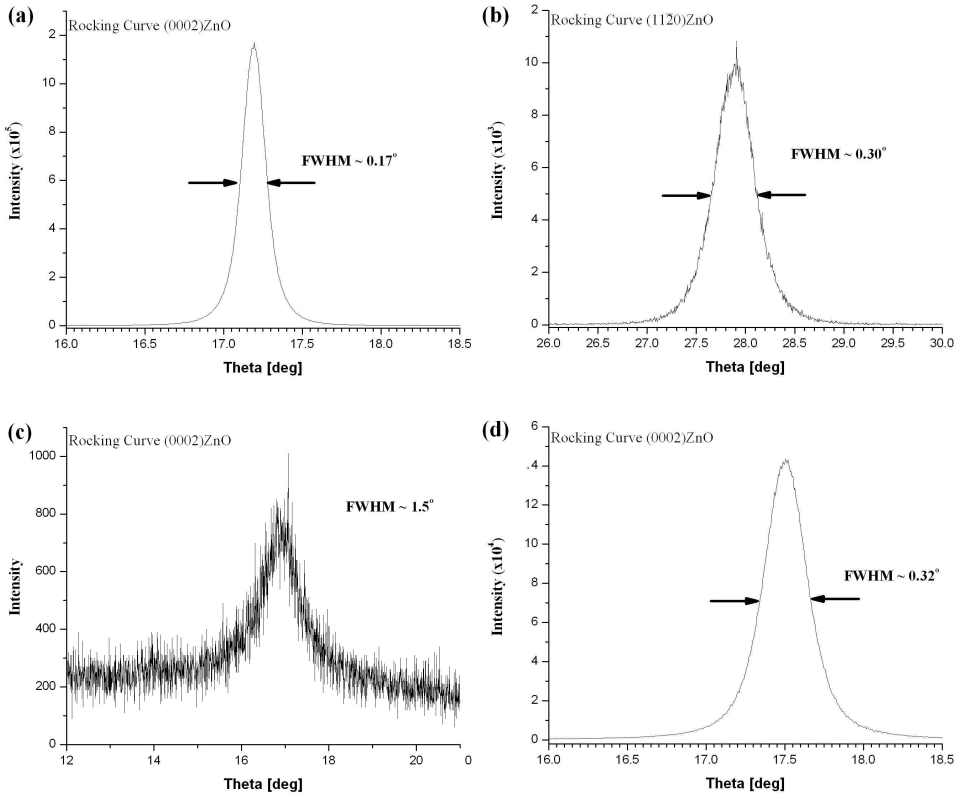

Figure 5.14: X-ray diffraction rocking curves for the crystalline ZnO peaks for ZnO grown on a-Al_2O_3 (a), r-Al_2O_3 (b-c), and c-Al_2O_3 (d) corresponding to samples pictured in Figure 5.13. The ZnO/r-Al_2O_3 was crystalline in both the (11$\bar{2}$0) and (0002) planes, (b) and (c) respectively.

this polycrystalline growth. The ZnO/c-Al_2O_3 sample was oriented along the [0002] axis and the rocking curve showed that the peak had a centre position at 17.5° with a FWHM of 0.32°, see Figure 5.14(d).

From this set of samples we see that increasing the number of ablation shots and the pressure had effectively produced nanostructures compared to otherwise similar growth procedures mentioned in previous sections. The duration of deposition was increased because it was believed that the earlier noted nanostructures were part of the wetting layer mentioned earlier. Since ZnO initially deposits in a layer-by-layer growth mode, we believed that by increasing the number of layers, strain in the film would build up and eventually 'release'

itself by allowing for more favourable island growth modes from that point forward. This situation is classical of the Stranski-Krastanov growth mode. It is believed that in the earlier samples, the vertical nanostructures observed were actually regions that had changed over from layer-by-layer to an island growth mode. The smooth, featureless regions between those island bases were wholly the wetting layer. Thus, when we increased the number of layer depositions, eventually these smoother areas also provoked new areas where SK-mode was favoured.

It is also proposed that as the velocity of the particles traveling to the surface could also be reduced (possibly by the shock wave due to the higher background pressures), this possibly allowed for enough time for clusters to form. These nanoclusters, once attached to the sample surface, would serve two possible purposes: (1) they would act themselves as seeding sites for island growth, and (2) these larger species would certainly cause more strain on the ZnO surface which would lead to an SK-mode of growth.

For both the increase of ablations and the pressure, once the Stranski-Krastanov growth mode began, these new-formed islands were then active nucleation sites for continuous vertical ZnO growth as observed in these samples.

5.3.2 Growth with Argon Ambient Gas

The third growth condition we decided to change was the the ambient gas during the actual deposition. Until this point all depositions were in pure O_2, so we modified the PLD system to allow deposition in Ar for a series of tests. We first tried with two independent ZnO depositions, both on a-Al_2O_3 substrates. As with the previous set of samples, these ZnO/a-Al_2O_3 samples was grown under the same pressure (of argon), temperature, fluence, and for 30 minutes deposition. Similarly both samples were not annealed, but post deposition, the chamber was filled to 1/2 atmosphere of oxygen gas.

The SEM analyses shows that the two samples grown under argon had distinctly different outcomes, as can be seen in Figure 5.15. The first ZnO/a-Al_2O_3

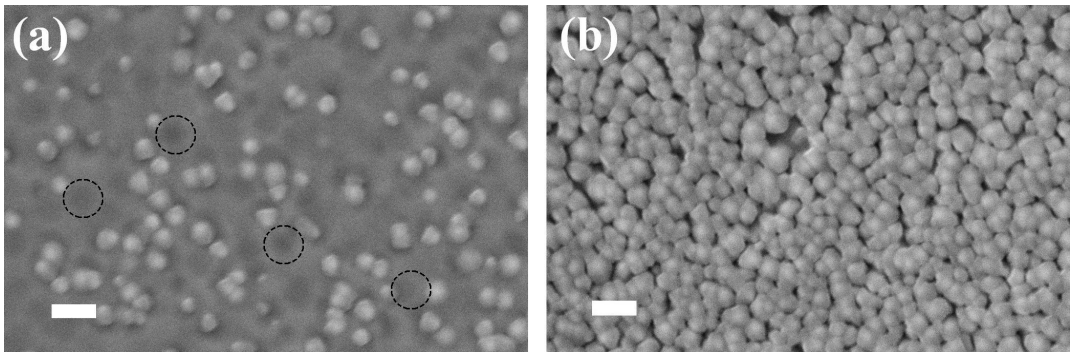

Figure 5.15: SEM images of two irregular ZnO films both grown on a-Al_2O_3 substrates deposited at 950 °C with a laser fluence of 2 J/cm^2 under 3.5 $\times$ 10^{-1} mbar of argon for 18,000 pulses. Dashed circles indicate a few areas where nano-holes were observed. Scale bars represent a distance of 1 micron.

seemed to revert to a structure more akin to earlier examples of nanostructures with a wetting layer. The nanostructures seen have widths of roughly 300 - 500 nm. Interestingly, the surface also has nano-holes of about the same diameters. It is unsure as to why such a unique ZnO surface was formed due to the presence of an argon background pressure. It is possible that such a film was created solely because the ZnO during ablation was oxygen-starved and was forced into such formation. In Figure 5.15(b), we see that the second ZnO/a-Al_2O_3 sample displays a more typical densely packed, albeit 'fused together', nanostructured surface. Again it is unsure why the columns melded together; this was sometimes observed on other sample surfaces but not to such an extent.

X-ray diffraction results differed from those deposited in presence of an oxygen environment, as shown in the 2θ-ω scans in Figure 5.16. The first ZnO/a-Al_2O_3 sample revealed that 3 orientations of ZnO had formed: the usual (0002) peak, and two unusual $(10\bar{1}0)$ and $(10\bar{1}1)$ peaks. Even though the latter

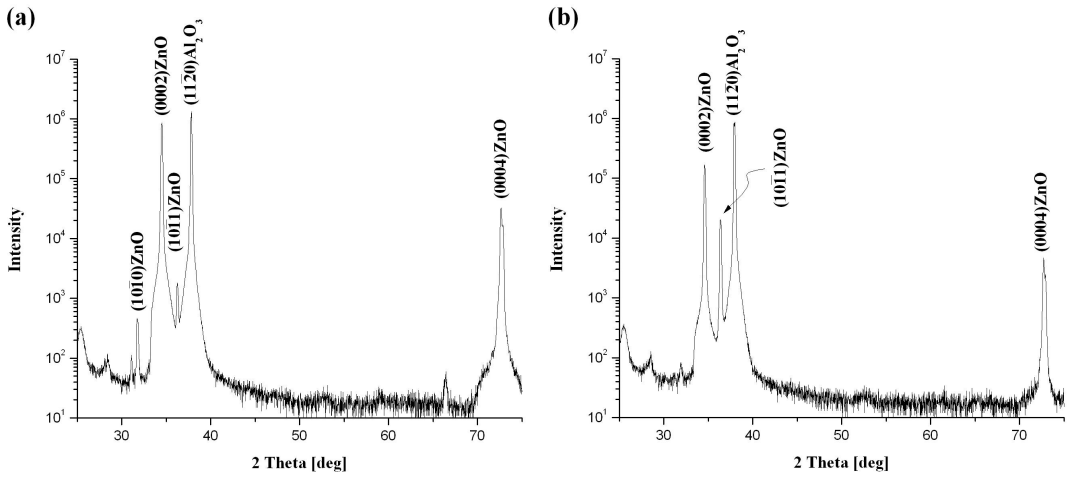

Figure 5.16: X-ray diffraction scans of two different ZnO/a-Al_2O_3 samples (see Figure 5.15) separately grown under the same conditions. The peaks labeled for ZnO were found to be crystalline.

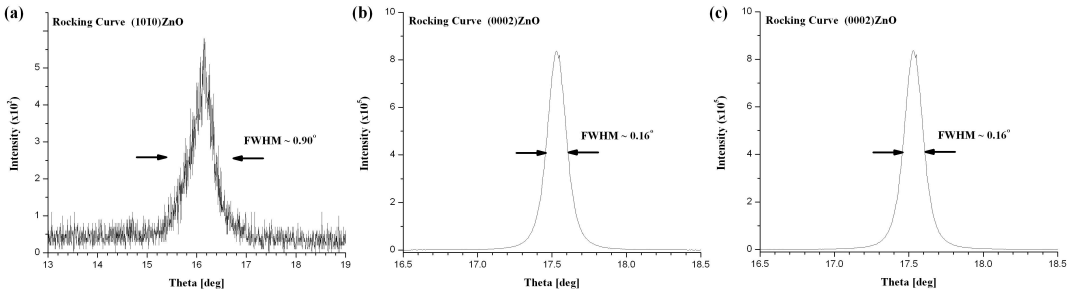

Figure 5.17: XRD rocking curves for ZnO/a-Al_2O_3 crystalline peaks for 2θ-ω scan shown in Figure 5.16(a).

two were very weak in intensity in comparison to the c-axis ZnO peak, rocking curves for the peaks indicated significant crystallinity. The (0002) peak, with an intensity ∼800,000 counts, had a rocking curve FWHM of 0.16° centered at 17.5°, see Figure 5.17(b). The (10$\bar{1}$0) peak, with an intensity of ∼400 counts, had a rocking curve FWHM of 0.90° centered at 16.1° (Figure 5.17(a)), while the (10$\bar{1}$1) peak, with an intensity of ∼2000 counts, had a FWHM of 0.45° centered at 18.4° (Figure 5.17(c)).

The XRD for the second ZnO/a-Al_2O_3 sample was also found to be poly-

crystalline with only two ZnO peaks at (0002) and (10$\bar{1}$1). The (0002)ZnO

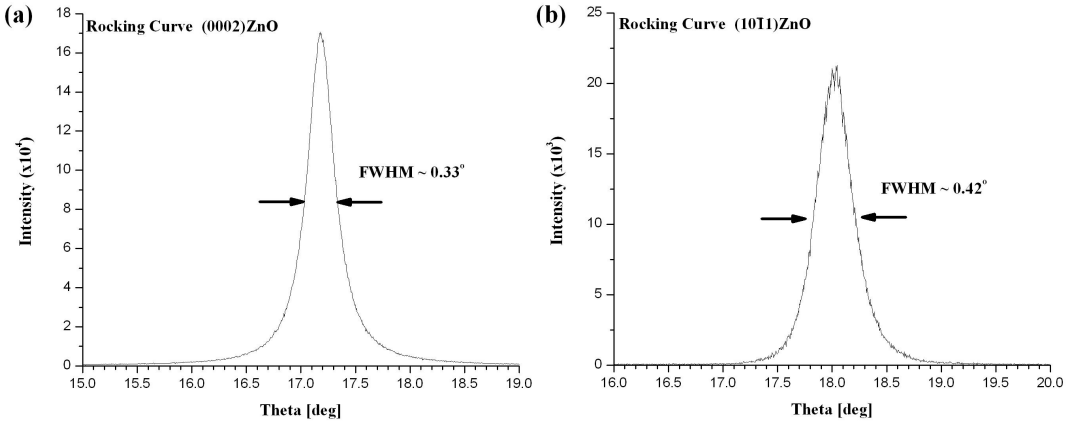

Figure 5.18: XRD rocking curves for ZnO/a-Al_2O_3 crystalline peaks for 2θ-ω scan shown in Figure 5.16(b).

peak, with and intensity of 180,000 counts, had a FWHM of 0.33° centered at 17.2° (Figure 5.18(a), while the (10$\bar{1}$1)ZnO peak, with an intensity of ∼20,000 counts, had a FWHM of 0.42° centered at 18.0° (Figure 5.18(b)).

One possible explanation for these results is since growths were done in presence of only an argon background gas, there was a lack of available oxygen for Zn-species to combine with, making the film oxygen deficient. In order to further explore the effect background gas, namely Ar, has on nanostructured growth, a series of experiments was devised and carried out as detailed in the following section.

5.3.3 Mixed Background Gas

In this section, the series of experiments done on varying the background gas during growth between varying ratios of O_2 and Ar gas are detailed. While the overall pressure was kept constant, the two gasses were varied in increments of 25% from pure Ar to pure O_2 ambient, i.e. O_2:Ar concentration ratios of: (a) 0%:100%, (b) 25%:75%, (c) 50%:50%, (d) 75%:25%, and (e) 100%:0%.

Other than the partial gas pressure, the growth condition for the series of five experiments were identical, as detailed, for each of the three cuts of sapphire. The Nd:YAG laser was still operated at $\lambda = 266$ nm at 10 Hz and focussed to 2 J/cm^2. The ZnO was ablated onto the substrates (preheated to 900 °C) for 18,000 shots with the overall pressure being 3.5×10^{-1} mbar. Each of the series of samples were also annealed for 30 extra minutes post-deposition and following that, the chamber was raised to 1/2 atm of O_2 during the slow cooling process. For clarity, the data analyses for the series of samples will be subdivided below according to the cut of sapphire the ZnO was grown upon. The discussions will follow in §5.3.3.4 for all three following sections. HR-SEM and AFM were used on all samples to image the surfaces and to gather physical details on the nanostructures themselves, and X-ray diffraction was used to determine their crystalline properties. Lastly room temperature photoluminescence was performed on the ZnO deposited on the *a*- and *c*-Al_2O_3 only.

5.3.3.1 ZnO/*a*-Al_2O_3

HR-SEM imaging of the ZnO grown on *a*-cut sapphire are shown in Figure 5.19 which respectively correspond to the O_2:Ar concentration ratios of (a)-(e) previously listed. Similarly, the corresponding AFM images for these same samples are shown in Figure 5.20. In sample (a), Figure 5.19(a), with no O_2, a rough structured film of ZnO with a scatter of larger quasi-hexagonal structures is observed. On this wetting-layer type surface, depressions can be seen throughout that resemble inverted hexagons - some with spherical deposits at the apex. In Figure 5.19(b), a range of packed hexagonal nanorods capped with nanopyramids are seen; these then are also capped with a tip-like structure. AFM analysis of sample in Figure 5.20(b) shows each of the pyramidal steps to be about 100 nm in height and each of the tips is about 250nm high; the overall height of the nanopyramid (steps + tip), is, on average, 700 nm. The

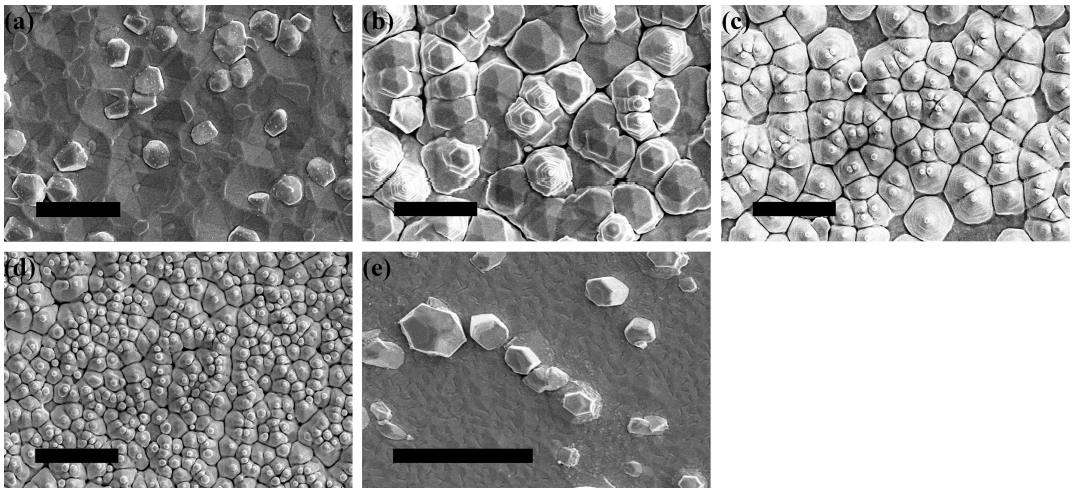

Figure 5.19: HR-SEM images of ZnO films grown on a-Al_2O_3 substrates deposited at 900 °C with a laser fluence of 2 J/cm^2 for 18,000 pulses. The 3.5 $\times$ 10^{-1} mbar background pressure during each growth was a mixed O_2:Ar concentration ratio of: (a) 0%:100%, (b) 25%:75%, (c) 50%:50%, (d) 75%:25%, and (e) 100%:0%. Scale bar represents 2 μm for images (a)-(d) and 5 μm for (e).

complete structure tapers upwards from a columnar base approximately 1 μm in width to 100 nm at the tip-like structure atop the nanopyramid. In Figure 5.19(c), the nanopyramid sharp terracing had smoothed out into a cone-like shape, making it difficult to measure the terrace step-heights with AFM (of Figure 5.20(c)). The bases of these nanostructures had been reduced in size by half and the cone tips heights are now about 90 nm tall and 85 nm wide as determined by AFM. The entire nanopyramids have an average total height of 400 nm. In Figure 5.19(d) and 5.20(d), the nanostructures have further reduced in size, overall average nanopyramid height of 300 nm, while the cone tips dimensions remain roughly the same with average heights of 90 nm and widths of 100 nm. Finally, in Figure 5.19(e) and 5.20(e), with 100% oxygen background gas, structures similar to those under 100% argon background gas have been produced with the exception of height. Instead of the cap-like structures in (a), the hexagonal nanostructures in (e) are approximately 300 nm in

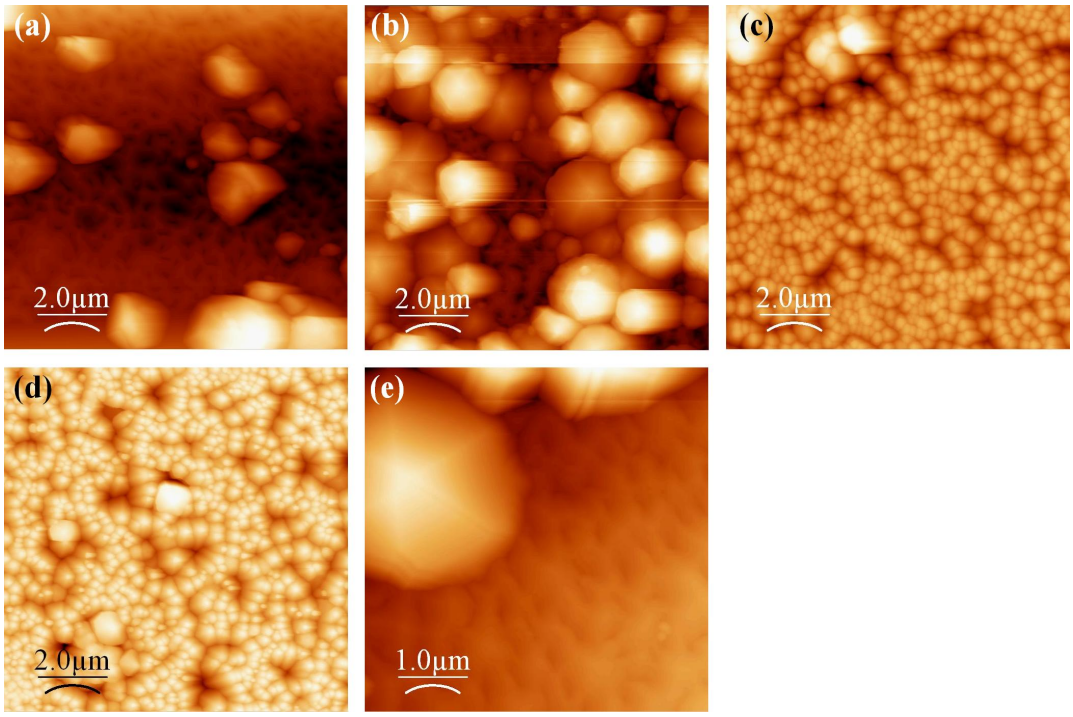

Figure 5.20: AFM images of corresponding samples shown in Figure 5.19(a) through (e). The 3.5×10^{-1} mbar background pressure during each growth was a mixed O_2:Ar concentration ratio of: (a) 0%:100%, (b) 25%:75%, (c) 50%:50%, (d) 75%:25%, and (e) 100%:0%.

height. The physical characteristics of these five samples are summarised in Table 5.2.

X-ray diffraction results determined that all 5 ZnO/a-Al_2O_3 nanostructure films are crystalline along the c-axis. The (0002) rocking curves for samples (a) through (e) are shown in Figure 5.21. The list of rocking curves FWHM are found in Table 5.3. ϕ-scans were also carried out and confirm the ZnO/a-Al_2O_3 epitaxial relationships for each sample.

Finally, room temperature photoluminescence showed intense, broadband, UV emission in the near band-edge region with peak positions listed also in Table 5.3(a)-(e), respectively (as show in Figure 5.22). An intense deep-level, green defect band was observed for sample (a), for no O_2 background gas,

Sample	Base Width [μm]	Pyramid Tips		Total Height [nm]
		Width [nm]	Height[nm]	
(a)	1-3	N/A	N/A	N/A
(b)	1	500	250	700
(c)	0.5	85	90	400
(d)	0.4	100	90	300
(e)	1-3	N/A	N/A	300

Table 5.2: Table of average physical dimensions for ZnO nanostructures grown on a-Al_2O_3 presented in this section and shown in Figures 5.19 and 5.20.

Sample	X-ray Diffraction	Photoluminescence
	Rocking Curve FWHM [deg]	Peak Positions [eV]
(a)	0.11	3.224
(b)	0.09	3.242
(c)	0.11	3.257
(d)	0.10	3.272
(e)	0.11	3.254

Table 5.3: Table of both the FWHM of XRD rocking curves and the PL peak positions (at 300 K) for ZnO nanostructures grown on a-Al_2O_3 presented in this section and shown in Figures 5.19 and 5.20.

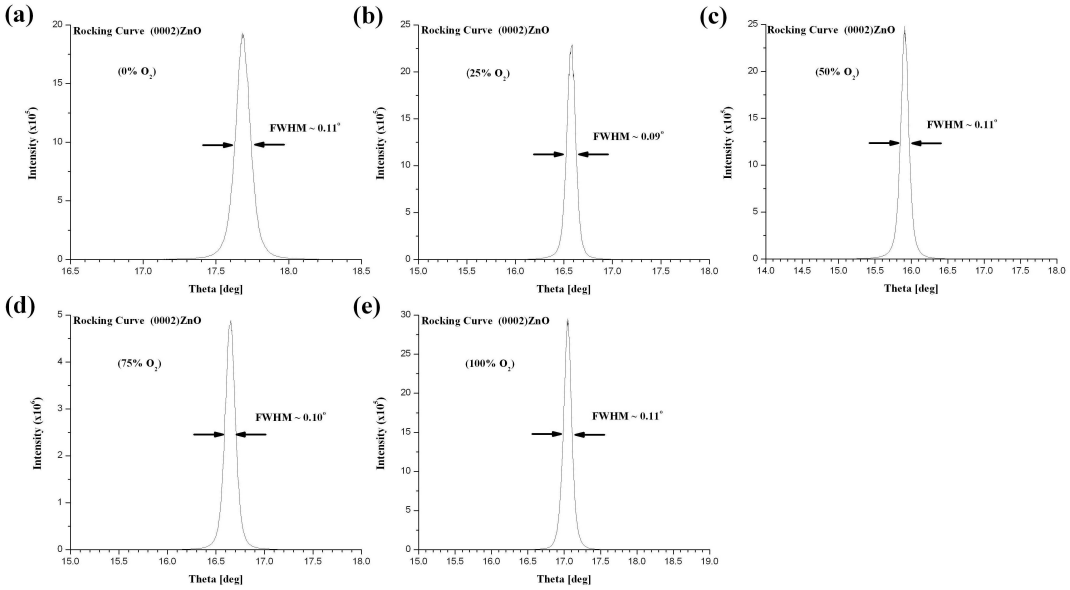

Figure 5.21: X-ray diffraction rocking curves for ZnO nanostructures grown on a-Al_2O_3 presented in this section and shown in Figures 5.19 and 5.20.

with an intensity of 6% to that of the main peak. The same band was further observed for sample with 100% O_2 background gas (e), which had a relative intensity of 21% to that of the main peak.

All discussions and conclusions for data presented in this section and the following two sections are done so together in §5.3.3.4.

5.3.3.2 ZnO/r-Al_2O_3

Similarly, HR-SEM imaging of ZnO/r-Al_2O_3 are shown in Figure 5.23 corresponding to the same O_2:Ar concentration ratios (a) - (e). Corresponding AFM data for these samples are presented in Figure 5.24(a) through (e). In Figure 5.23(a), the ZnO has formed the usual underlying striae with cap-like nanostructures with a somewhat hexagonal form. The AFM in Figure 5.24(a) shows these cap-like nanostructures have average widths of 1.5 μm and heights of 800 nm, while the average width of each of the stria is 400 nm. In Figure 5.23(b), the approximately half of the nanostructures observed had a hexago-

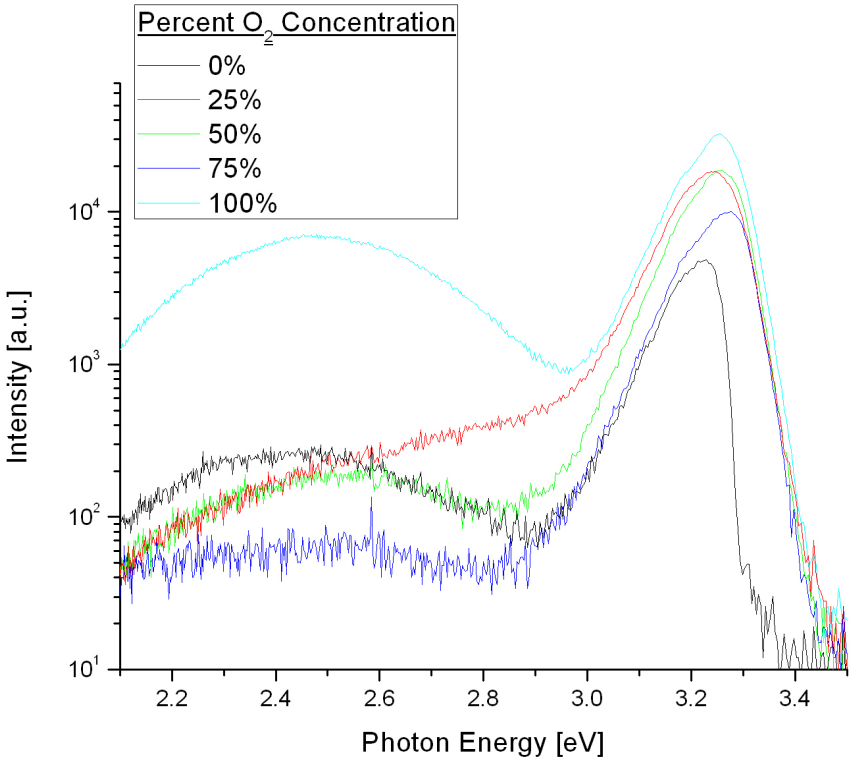

Figure 5.22: Photoluminescence spectra of ZnO films grown on a-Al_2O_3 substrates deposited at 900 °C with a laser fluence of 2 J/cm^2 for 18,000 pulses. The 3.5 $\times$ 10^{-1} mbar background pressure during each growth was a mixed O_2:Ar concentration ratio of: (a) 0%:100%, (b) 25%:75%, (c) 50%:50%, (d) 75%:25%, and (e) 100%:0%.

nal cone-shaped top, while the rest had grown into the surrounding structures. The nanostructures covered the entire sample and there was no presence of any striae. From AFM, the observed nanostructures were determined to range in widths from 0.5 - 1 μm in size. In Figure 5.23(c), underlying ZnO striae are observed with tilted nanostructures emerging from the surface, a majority of which are hexagonal in shape . In addition, nano-sized spheres are seen in the HR-SEM images, but were not detected in the AFM imaging (Figure 5.24(c)). It is possible that these spheres could be an artifact due to the gold coating the samples must receive beforehand. The AFM reveals that these nanostructures

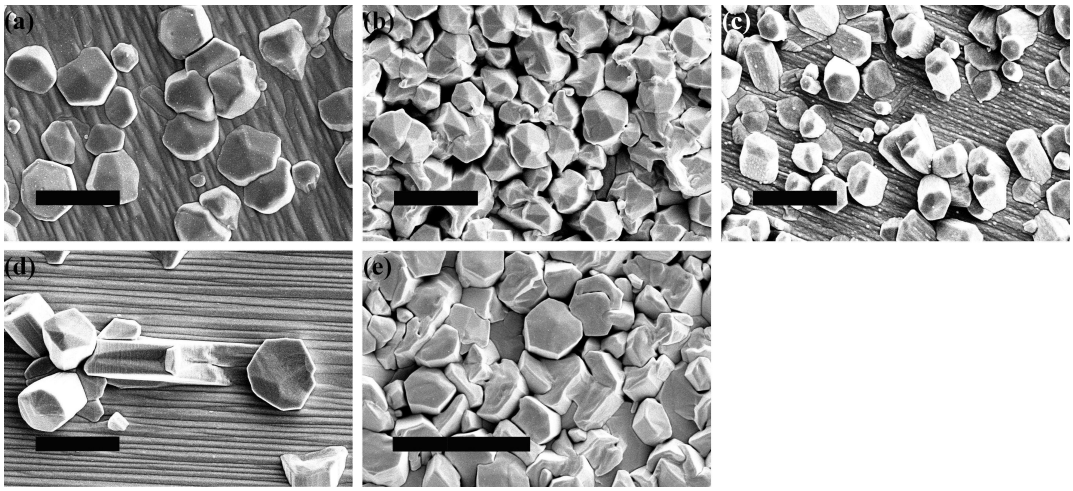

Figure 5.23: HR-SEM images of ZnO films grown on r-Al_2O_3 substrates deposited at 900 °C with a laser fluence of 2 J/cm^2 for 18,000 pulses. The 3.5 $\times$ 10^{-1} mbar background pressure during each growth was a mixed O_2:Ar concentration ratio of: (a) 0%:100%, (b) 25%:75%, (c) 50%:50%, (d) 75%:25%, and (e) 100%:0%. Scale bar represents 2 μm for images (a)-(d) and 5 μm for (e).

columns have reduced in width to an average of 600 nm and the heights widely range from 0.5 - 1.5 μm. The striae themselves have also become very narrow with an average stria measuring 65 nm wide. In Figure 5.23(d), the ZnO surface is comprised of more striae than emerging nanostructures. AFM reveals these columns are roughly about 1 - 1.5 μm in width and have heights ranging from 250nm upwards to 2 μm. The striae themselves range in widths from 150 - 300 nm. Finally, in Figure 5.23(e), the structure seen here under 100% O_2 is somewhat similar to that seen in Figure 5.23(b), but with less hexagonally shaped structures. Those that have a hexagonal form have an average width of 2 μm. The physical characteristics are summarised in Table 5.4.

For this set of 5 samples on r-Al_2O_3 , XRD results showed all ZnO films were polycrystalline in both the usual ZnO/r-Al_2O_3 growth direction in the [11$\bar{2}$0] direction and also in the natural [0002] growth direction of ZnO. The rocking curves showed that the ZnO was more aligned in the (11$\bar{2}$0) plane than

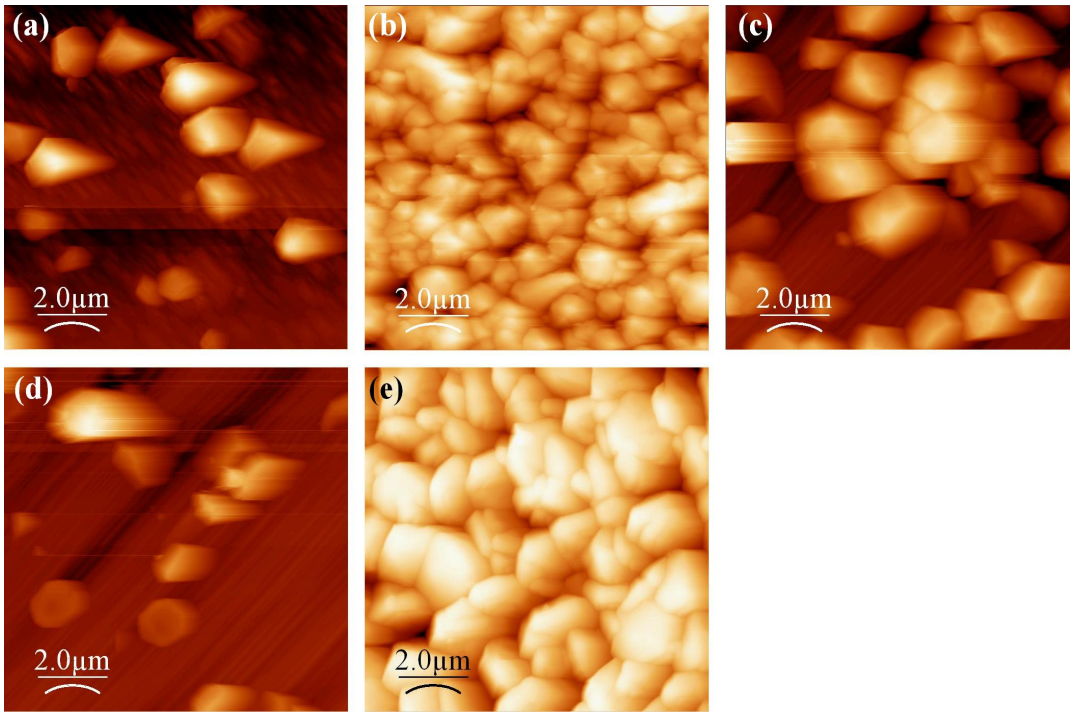

Figure 5.24: AFM images of corresponding samples shown in Figure 5.23(a) through (e). The 3.5×10^{-1} mbar background pressure during each growth was a mixed O_2:Ar concentration ratio of: (a) 0%:100%, (b) 25%:75%, (c) 50%:50%, (d) 75%:25%, and (e) 100%:0%.

in the (0002) plane. The rocking curves for the $(11\bar{2}0)$ and (0002) peaks for samples (a) - (e) are combined in Table 5.5.

All discussions and conclusions for data presented in this section, the preceding section and, the following two sections are done so together in §5.3.3.4.

5.3.3.3 ZnO/*c*-Al_2O_3

Lastly, the HR-SEM imaging for the set of five ZnO*c*-Al_2O_3 samples (with the same corresponding (a) - (e) O_2:Ar ratios) are shown as Figure 5.25. Corresponding AFM data for these samples are presented in Figure 5.26(a) through (e). In Figure 5.25(a), we see that the nanostructures formed are relatively shapeless and featureless for the most part, but some columns with a

Sample	Base Width [μm]	Total Height [μm]	Stria Width [nm]
(a)	1.5	0.8	400
(b)	0.5-1	N/A	N/A
(c)	0.6	0.5-1	65
(d)	1-1.5	0.25-2	150-300
(e)	2	N/A	N/A

Table 5.4: Table of average physical dimensions for ZnO nanostructures grown on r-Al_2O_3 presented in this section and shown in Figures 5.23 and 5.24.

Sample	XRD Rocking Curve FWHM [deg]	
	$(11\bar{2}0)$ZnO	(0002)ZnO
(a)	0.26	1.13
(b)	0.28	1.33
(c)	0.31	0.99
(d)	0.26	1.41
(e)	0.31	2.24

Table 5.5: Table of the FWHM for x-ray diffraction rocking curves for of both the $(11\bar{2}0)$ZnO and (0002)ZnO grown on r-Al_2O_3 presented in this section and shown in Figures 5.23 and 5.24.

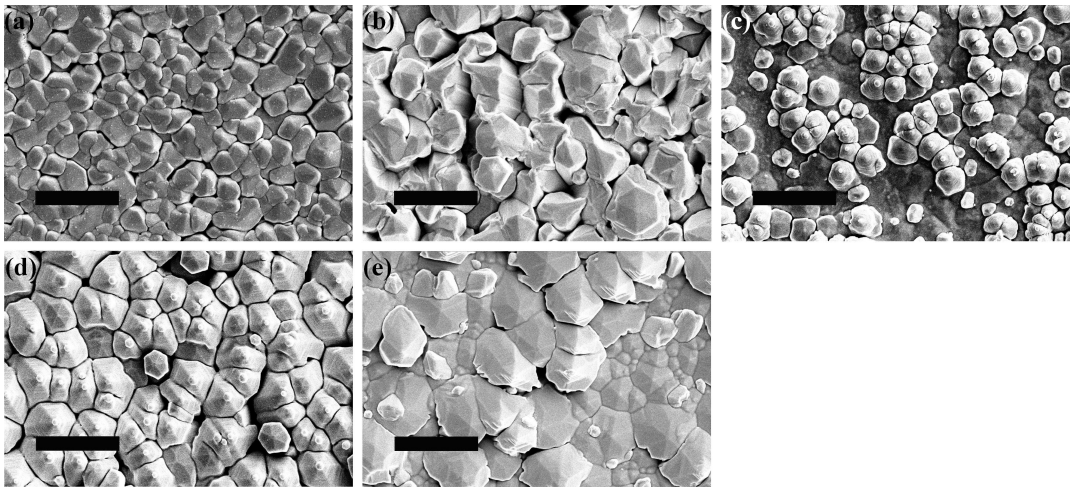

Figure 5.25: HR-SEM images of ZnO films grown on c-Al_2O_3 substrates deposited at 900 °C with a laser fluence of 2 J/cm^2 for 18,000 pulses. The 3.5 $\times$ 10^{-1} mbar background pressure during each growth was a mixed O_2:Ar concentration ratio of: (a) 0%:100%, (b) 25%:75%, (c) 50%:50%, (d) 75%:25%, and (e) 100%:0%. Scale bars represent 2 μm for all images.

hexagonal top are present. From AFM (Figure 5.26(a)), the average width of these nanostructures is 500 nm and the average height is 200 nm. Figure 5.25(b) shows more presence of hexagonal-capped columns, but overall the nanostructures have grown towards each other. The average width of these nanostructures has increased to 800 nm and the height, due largely to the gaps between, increase to approximately 800 nm (Figure 5.26(b)). In Figure 5.25(c), the ZnO is more ordered with clusters of cone-like nanostructures with tiny hexagonal-shaped dots on top. These are not unlike those seen in Figure 5.19(c). These cones again have semblance to previously seen nanopyramids, but no steps were measurable with the AFM (Figure 5.26(c)). The base of these structures were measured by AFM as approximately 500 nm wide and tapered upwards to the hexagonal dots, with widths of 65 nm. The average total height of these nanostructures was 700 nm. In Figure 5.25(d), we see a similar surface to the previous, except it is entirely covered with these nanopyramid-like structures

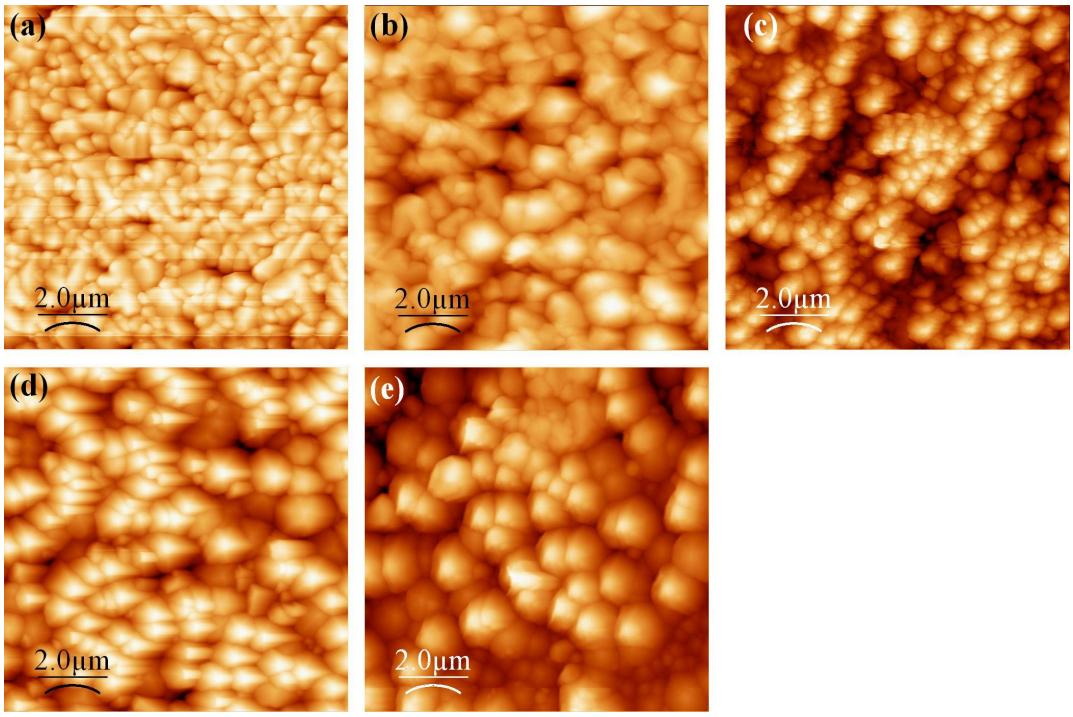

Figure 5.26: AFM images of corresponding samples shown in Figure 5.25(a) through (e). The 3.5×10^{-1} mbar background pressure during each growth was a mixed O_2:Ar concentration ratio of: (a) 0%:100%, (b) 25%:75%, (c) 50%:50%, (d) 75%:25%, and (e) 100%:0%.

(instead of the clumped islands) and additionally, random, perfectly-formed, hexagonal columns protrude the surface. These nanopyramid-like structures were measured with AFM (Figure 5.26(d)) and found to be wider at the base with an average width of 750 nm and taper to equally wider hexagonal dots with an average widths in the 150 - 200 nm range. The perfect hexagonal columns range in widths from 350 - 400 nm. Lastly, in Figure 5.25(e), the ZnO surface is densely packed with hexagonal-shaped structures. The underlying structures have excellent hexagonal form, as do some of the larger ones, however the larger structures appear to be overlapping each other in one direction. On the side of this direction, more semblance of terracing is visible (but, again, could not be measured with the AFM, image shown in Figure 5.26(e)). The

Sample	Base Width [μm]	Pyramid Tip Width [nm]	Total Height [nm]
(a)	0.5	N/A	200
(b)	0.8	N/A	800
(c)	0.5	65	700
(d)	0.75	150-200	N/A
(e)	1.5	N/A	300

Table 5.6: Table of average physical dimensions for ZnO nanostructures grown on c-Al_2O_3 presented in this section and shown in Figures 5.25 and 5.26.

columns on this surface range widely in size upwards of 1.5 μm in width; the average heights are approximately 300 nm. Again the physical measurements determined with the AFM are detailed in Table 5.6.

XRD results showed that these 5 samples of ZnO on c-Al_2O_3 were crystalline along the [0002] direction. The rocking curves for this peak are listed in Table 5.7.

Finally, room temperature PL had also been carried out for this set of 5 samples which also showed intense, broadband, UV emission in the near band-edge region. These peak positions are listed in Table 5.7 for samples (a)- (e), respectively (as shown in Figure 5.27. In addition to the main peak for sample (a) with no O_2 background gas, two small shoulders in the violet region are present, with the first being approximately 0.11 eV wide centered at 3.01 eV, and the second approximately 0.13 eV wide and centered at 2.85 eV. As with the samples on a-Al_2O_3 , two deep-level, green defect bands were observed for samples (c) and (e) and, in addition, a very shallow, green defect band for sample (d) was observed just above background noise. The weak green bands observed for sample (c), with 50% O_2 concentration, for sample (d), with 75% O_2, and sample (e), with 100% O_2 had relative intensities of 1.8%, <1%, and 1.2%, respectively to those of their main peaks.

Sample	X-ray Diffraction Rocking Curve FWHM [deg]	Photoluminescence Peak Positions [eV]
(a)	0.16	3.272
(b)	0.13	3.261
(c)	0.14	3.252
(d)	0.12	3.260
(e)	0.12	3.256

Table 5.7: Table of both the FWHM of XRD rocking curves and the PL peak positions (at 300 K) for ZnO nanostructures grown on c-Al_2O_3 presented in this section and shown in Figures 5.25 and 5.26.

All discussions and conclusions for data presented in this section and the two preceding sections are done so together in §5.3.3.4.

5.3.3.4 O_2/Ar Study Discussions

From the XRD results for all 3 sets of experiments, one sees that all of the samples produced highly crystalline ZnO nanostructures regardless of the relative oxygen concentration. For each of the 3 cases with only an argon ambient acting as a buffer gas, there was still a sufficient amount of oxygen present in the film to be highly ordered throughout. The oxygen in these cases could only come from the target's stoichiometric ZnO or from the post anneal, which would mainly effect the topmost layers and would not allow for such a highly crystalline structure throughout the entire ZnO nanostructure film. This implies that as the ablated ZnO travels towards the substrate or on the substrate surface, single oxygen species are being incorporated throughout the crystalline bulk of the film.

We now propose a qualitative model to interpret the surface morphology in light of the results presented in the three preceding sections. This model is

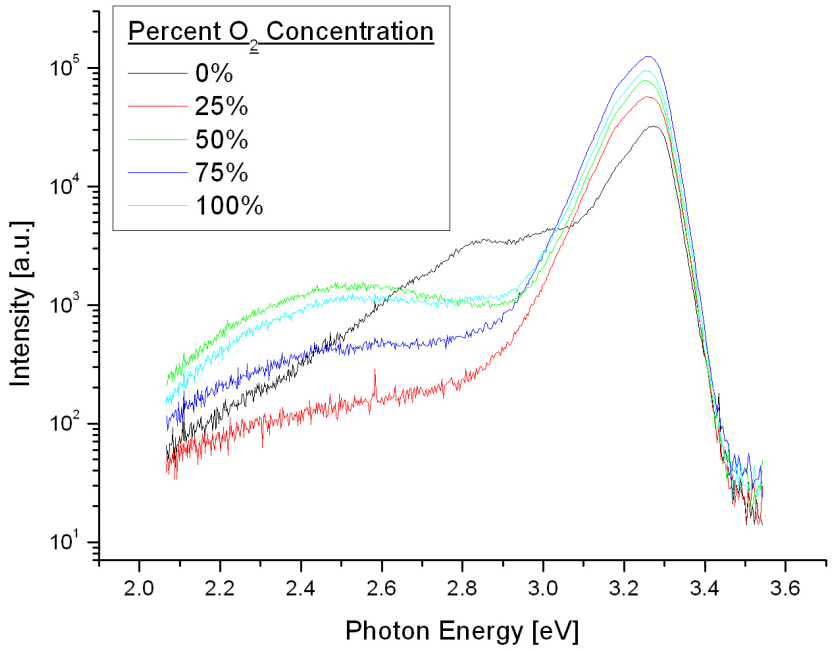

Figure 5.27: Photoluminescence spectra of ZnO films grown on c-Al_2O_3 substrates deposited at 900 °C with a laser fluence of 2 J/cm^2 for 18,000 pulses. The 3.5 $\times$ 10^{-1} mbar background pressure during each growth was a mixed O_2:Ar concentration ratio of: (a) 0%:100%, (b) 25%:75%, (c) 50%:50%, (d) 75%:25%, and (e) 100%:0%.

based on three basic assumptions: (1) that nanoclusters form in the expanding plume under certain conditions [10, 14, 15], (2) these deposit onto the substrate surface to act as nucleation sites, and (3) nanopyramids grow according to a columnar growth (CG) mode [16].

In the 3 cases of sample (a) where there is only argon gas present during deposition, we proposed the argon seemed to work as a buffer in slowing down the plume enough to allow for some in-plume crystallisation. From Figures 5.19(a) and 5.25(a) we see there was a lack of distinct overall shape to the larger structures that had undergone a CG mode, and similarly in Figure 5.23(a) for both the $(000l)$ZnO and $(11\bar{2}0)$ZnO orientations. For sample (a) on a-

Al_2O_3 the underlying textured surface has definite hexagonal depressions, and for sample (a) on r-Al_2O_3 there were definite hexagonal cap-like structures protruding from the c-axis ZnO surface, which are in the $(11\bar{2}0)$ orientation. We reasonable assume, a few of the inverted depressions had acted as attractive sites for nucleation, as the 6-sided depression would form as many nearest-neighbour bonds for any passing adatom. As seen in Figure 5.23(a), some of these inversions have actually begun a nucleation site at the apex, which further increases the potential for electrostatically attracting incoming particles from the plume. The hexagonal cap-like structures on the r-Al_2O_3 had developed on nucleation sites after SK growth began. In the case of sample (a) on c-Al_2O_3, not much can be said of its featureless surface, despite the material being highly crystalline. In the three cases of sample (a), since there was no external source of oxygen available during growth except what was from the target, the finite limit of O_2 limited the possible amount of ZnO nanoclusters that can be formed; thus, there was more of a crystalline, film-like coverage.

In samples (b) - (d) for all three cuts of substrate, a similar process to above occurs, but since there is an increasing amount of oxygen present, a larger number of nanoclusters form within the plume. The greater abundance of these nanocrystallites depositing on the surface increases the strain of the initial underlying film. Eventually this case is reduced, for samples on a- and c-Al_2O_3 following the transition to CG mode resulting in the observed packed, hexagonal nanopyramids. This similarly occurs on the r-Al_2O_3 also, except it follows the transition to SK mode resulting in a rough array of tilted nanostructures. An excellent tilted-view image of the ZnO and sapphire boundary was taken (corresponding to the conditions of Figure 5.25(d)). This view can be seen in Figure 5.28 and shows both (1) a definitive view of individual columns (not fused together) from the base of the substrate interface as indicated just above the red line, and (2) the tapered hexagonal nanopyramids atop these columns. Additionally we also confirm the duration of growth does yield the assumed

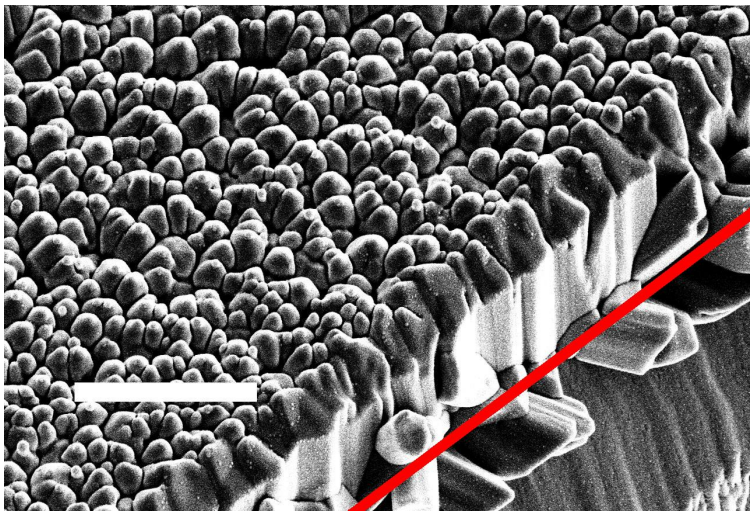

Figure 5.28: A tilted view of the ZnO/sapphire interface (above solid red line). The columns are clearly visible as well as the nanopyramid tops. The scale bar represents approximately 2 μm.

$\sim$2 μm thickness of the nanostructures.

In the cases of sample (e) on the 3 cuts of sapphire, there is an excess of O_2 gas, and as expected had grown crystalline as shown by XRD results. However, SEM data suggests that under these conditions, there were not enough nanoclusters formed in the plume to lead to the stress-driven mechanism for the columnar or Stranski-Krastanov growth modes just described.

The PL spectra for those samples on a-Al_2O_3 are shown in Figure 5.22. It is observed that the higher oxygen partial pressure the more intense the featureless green band (attributed to oxygen vacancies, V_O [17]) is. Similarly, but to a much lesser extent, the PL spectra for the samples on c-Al_2O_3 (seen in Figure 5.27) also present the green band for those samples with higher oxygen partial pressures. Although contradictory at first glance, this observation can be explained by the known Zn-rich conditions prevailing in a laser plume of ZnO ablated in O_2 which is poorly oxidising [18]. Similar observations were made by Liu *et al.* [19]. In other words, even though one might expect to see

less V_O in a oxygen-rich environment, there is seemingly an effect the argon has towards reducing these vacancies.

These PL results appear to support our qualitative growth model: in the case of sample (e) on a-Al_2O_3 and samples (c) - (e) on c-Al_2O_3 , the presence of the various green bands support our interpretation that not enough oxygen is engaging in the formation of ZnO nanoclusters prior to reaching the surface. It also shows that the post-anneal is not effecting the overall stoichiometry of the as-grown ZnO film or crystalline property. In the cases of the two samples under condition (a) on a-Al_2O_3 and c-Al_2O_3 , respectively there was a reduced intensity green band emission and a pair of shallow bands both detected in the violet region. The green band on the a-Al_2O_3 sample, as mentioned, was due to V_O and the bands in the violet region are equally due to V_O as reported by various authors [4, 20, 21]. This also supports the model as ablated atomic oxygen is likely to reach the substrate in an Ar atmosphere, but at the cost of a reduced rate due to possible oxygen species recombining. In short, the resultant film tends to be oxygen deficient: (1) under 100% Ar background gas due to the lack of abundant oxygen other than from the stoichiometric ZnO in the plume, or (2) under 100% O_2 background gas due to the lack of Ar molecules assisting with the formation of nanoclusters.

5.3.4 Isolated Nanostructures

A unique set of samples were grown under all but one of the same conditions to those corresponding to samples produced under a 100% oxygen atmosphere in the preceding section (§5.3.3). This only exception was that in the preceding section samples were grown at 900 °C and the 3 samples presented here (see Figure 5.29) that were grown at a slightly higher temperature of 950 °C. As can be seen from the SEM images the ZnO films grown on a-, r-, and c-cut sapphire look completely different to those from Figures 5.19(e), 5.23(e), and

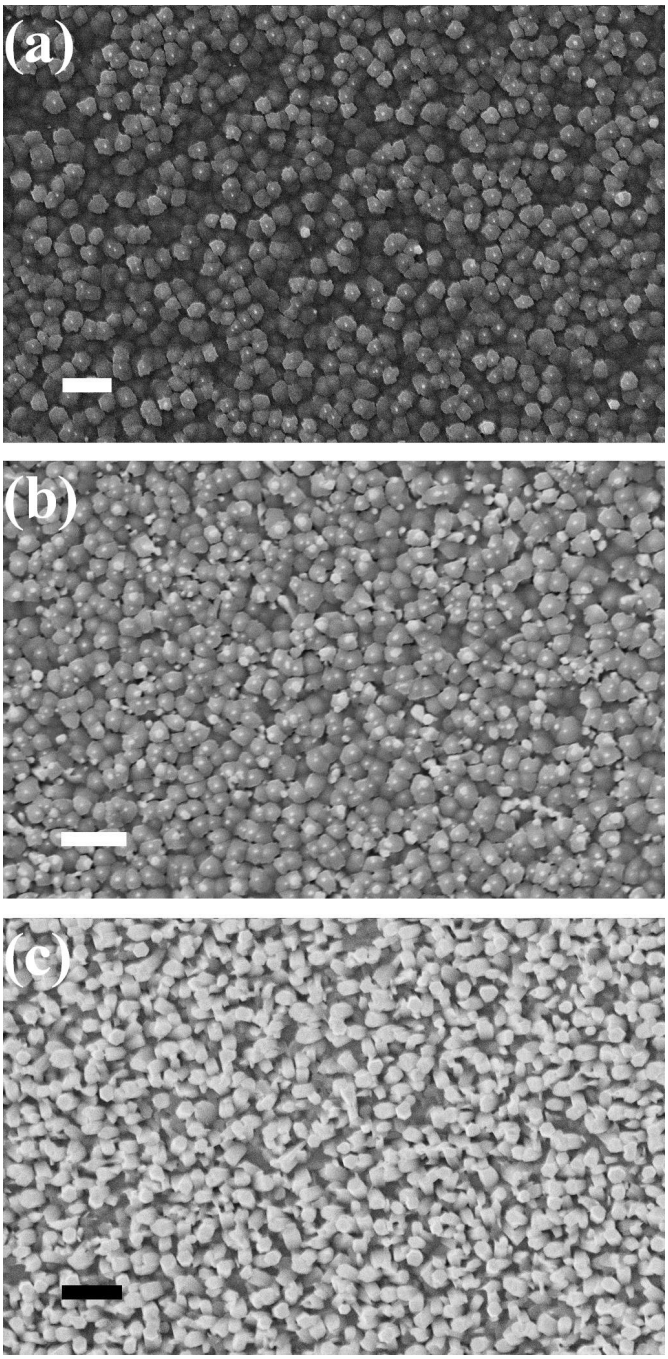

Figure 5.29: SEM images of ZnO films grown on (a) a-Al_2O_3, (b) r-Al_2O_3, and (c) c-Al_2O_3 substrates deposited at 950 °C with a laser fluence of 2 J/cm^2 for 18,000 pulses (pO_2 = 3.5 $\times$ 10^{-1} mbar background pressures). Scale bars represent 3 μm for all images.

5.25(e) respectively. Additionally, for the samples grown on a- and r-sapphire, isolated, nanostructured, spike-like columns are observed (seen more clearly in the magnified images of Figures 5.30 and 5.31).

The ZnO/a-Al_2O_3 sample had the most interesting variation of the three samples. The hexagonal nanostructured columns range in widths from 750 - 1500 nm. The isolated nanostructures atop the columns were roughly 100 nm wide and ranged in heights from 100 - 150 nm tall. Some of the sample was covered in these hexagonal columns with the additional nano-spikes. A closer HR-SEM view of these are seen in Figure 5.30

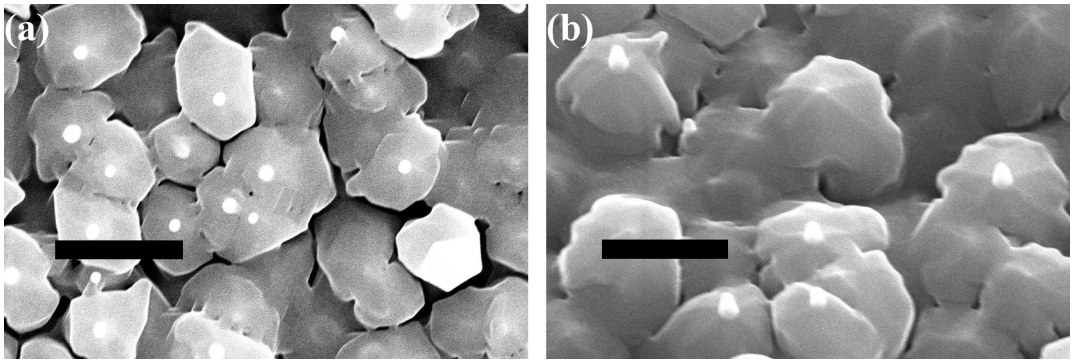

Figure 5.30: HR-SEM (a) top-down and (b) tilted views of ZnO films grown on a-Al_2O_3 showing columnar growth with additional isolated nanostructured spikes on top. Scale bars represent 1 μm.

The image in Figure 5.30 was observed on roughly half of the substrate. The nanostructured morphology for the other half of the sample is shown in Figure 5.31. In these top-down and tilted images, a complex multi-leveled network of bridges and walls can be seen.

The ZnO sample grown on r-Al_2O_3, is less interesting but also shares the development of these nanostructured columns with spikes on top. The hexagonal columns are around 750 nm wide and the tips are in the range of 50 - 100 nm. There was only the single form of growth on this sample unlike that on the a-Al_2O_3. The ZnO/c-Al_2O_3 was the least interesting of the three as it did

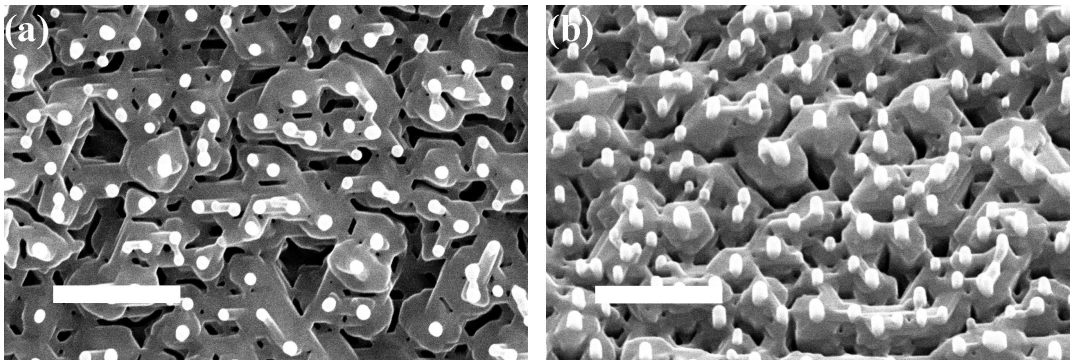

Figure 5.31: HR-SEM (a) top-down and (b) tilted views of ZnO films grown on a-Al_2O_3 showing columnar growth with additional isolated nanostructured spikes on top. Scale bars represent 1 μm.

not possess these isolated spikes at all, nor were the hexagonal columns well aligned on the surface. The columns were in the range of 750 - 1500 nm wide.

It is inconclusive as to why such a slight temperature variation of 50 °C would yield quite interesting features. It might possibly be the fact that within a certain temperature range one mode of crystalline growth is favoured over another, in this case, island or SK-mode due to the presence of these spikes.

5.3.5 Nanostructures on Silicon

Finally, we report and example of the successful growth of ZnO nanostructures on Si. Figure 5.32 shows a nanostructured film of misshapen hexagonal columns on a Si(100) substrate surface. The sample was grown deposited at 900 °C at half the growth duration (9,000 shots) with a laser fluence of 2 J/cm^2. The ambient oxygen pressure was 3.5×10^{-1} mbar during growth and the sample was allowed to cool immediately after deposition (no annealing).

The nanostructures ranged from 250 - 500 nm and were mostly vertically aligned. XRD shows that the ZnO is crystalline in the [0002]-direction. However, the rocking curve performed shows that the ZnO is crystalline with a FWHM of $\sim$3.5°. Recall, despite the fact this ZnO nanostructured film is

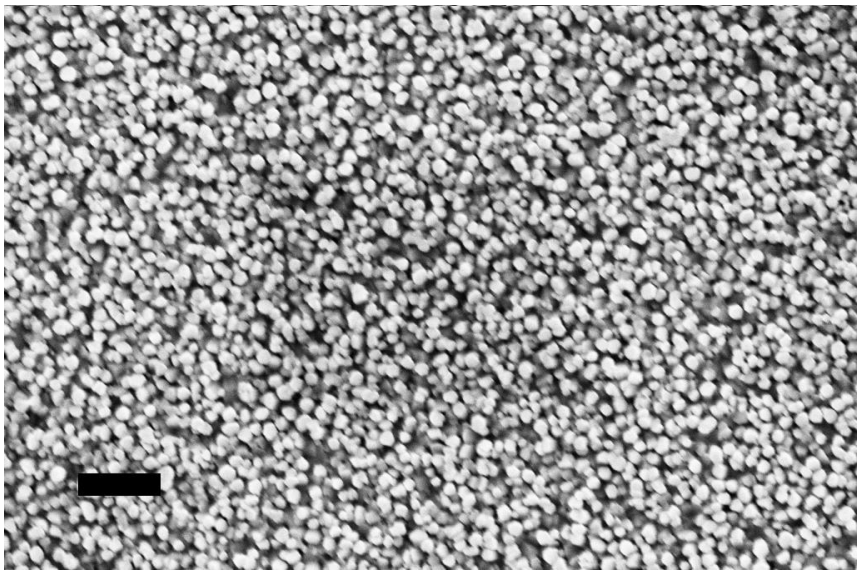

Figure 5.32: SEM image of a ZnO nanostructured surface grown on Si(100). The scale bar represents 3 μm.

'poor' in terms of (0002)ZnO rocking curves seen earlier (for example, samples in §5.3.3.1 with a FWHM around 0.1°), this result is comparable to the ZnO/Si(100) samples presented in §5.1.1. This is more than likely due to the large lattice mismatch and the lack of any buffer layer before depositing the ZnO.

References

[1] A. Tsukazaki, A. Ohtomo, T. Onuma, M. Ohtani, T. Makino, M. Sumiya, K. Ohtani, S. F. Chichibu, S. Fuke, Y. Segawa, H. Ohno, H. Koinuma, and M. Kawasaki. Repeated temperature modulation epitaxy for p-type doping and light-emitting diode based on ZnO. *Nature Materials*, 4(1):42–46, 2005.

[2] T. Nobis, E. M. Kaidashev, A. Rahm, M. Lorenz, and M. Grundmann. Whispering gallery modes in nanosized dielectric resonators with hexagonal cross section. *Physical Review Letters*, 93(10):103903, Sep 2004.

[3] T. Okada and K. Kawashima. Synthesis of a variety of ZnO nanostructured crystals by nanoparticle-assisted pulsed-laser deposition. volume 5662, pages 420–425. SPIE - Fifth International Symposium on Laser Precision Microfabrication, 2004.

[4] X. W. Sun and H. S. Kwok. Optical properties of epitaxially grown zinc oxide films on sapphire by pulsed laser deposition. *Journal of Applied Physics*, 86(1):408–411, 1999.

[5] D. P. Norton. Synthesis and properties of epitaxial electronic oxide thin-film materials. *Materials Science and Engineering: R: Reports*, 43(5-6):139–247, 2004.

[6] F. C. Stedile, I. J. R. Baumvol, I. F. Oppenheim, I. Trimaille, J. J. Ganem, and S. Rigo. Thickness of the SiO_2/Si interface and composition of silicon

oxide thin films: Effect of wafer cleaning procedures. *Nuclear Instruments and Methods in Physics Research Section B: Beam Interactions with Materials and Atoms*, 118(1-4):493–498, 1996.

[7] A. Nahhas, H. K. Kim, and J. Blachere. Epitaxial growth of ZnO films on Si substrates using an epitaxial GaN buffer. *Applied Physics Letters*, 78(11):1511, 2001.

[8] S. P. Chang, S. J. Chang, Y. Z. Chiou, C. Y. Lu, T. K. Lin, C. F. Kuo, H. M. Chang, and U. H. Liaw. ZnO epitaxial layers grown on nitridated Si(100) substrate with HT-GaN/LT-ZnO double buffer. *Journal of Crystal Growth*, 310(2):290 – 294, 2008.

[9] A. B. Hartanto, X. Ning, Y. Nakata, and T. Okada. Growth mechanism of ZnO nanorods from nanoparticles formed in a laser ablation plume. *Applied Physics A: Materials Science & Processing*, 78(3):299–301, 2004.

[10] T. Okada, K. Kawashima, and M. Ueda. Ultraviolet lasing and field emission characteristics of ZnO nano-rods synthesized by nano-particle-assisted pulsed-laser ablation deposition. *Applied Physics A*, 81(5):907–910, 2005.

[11] Y. Sun, G. M. Fuge, and M. N. R. Ashfold. Growth of aligned ZnO nanorod arrays by catalyst-free pulsed laser deposition methods. *Chemical Physics Letters*, 396(1-3):21–26, 2004.

[12] B. K. Meyer, H. Alves, D. M. Hofmann, W. Kriegseis, D. Forster, F. Bertram, J. Christen, A. Hoffmann, M. Straßburg, M. Dworzak, U. Haboeck, and A. V. Rodina. Bound exciton and donor-acceptor pair recombinations in ZnO. *Physica Status Solidi (B)*, 241(2):231–260, 2004.

[13] S.-C. Liu and J.-J. Wu. Low-temperature and catalyst-free synthesis of well-aligned ZnO nanorods on Si(100). *Journal of Materials Chemistry*, 12(10):3125–3129, 2002.

[14] I. Ozerov, A. V. Bulgakov, D. K. Nelson, R. Castell, and W. Marine. Production of gas phase zinc oxide nanoclusters by pulsed laser ablation. *Applied Surface Science*, 247(1-4):1–7, 2005.

[15] S. Choopun, H. Tabata, and T. Kawai. Self-assembly ZnO nanorods by pulsed laser deposition under argon atmosphere. *Journal of Crystal Growth*, 274(1-2):167–172, 2005.

[16] M. A. Herman, W. Richter, and H. Sitter. *Epitaxy: Physical Princilples and Technical Implementation*. Springer-Verlag, Berlin, Heidelberg, New York, 2004.

[17] Ü. Özgür, Ya. I. Alivov, C. Liu, A. Teke, M. A. Reshchikov, S. Doğan, V. Avrutin, S.-J. Cho, and H. Morkoç. A comprehensive review of ZnO materials and devices. *Journal of Applied Physics*, 98(4):041301, 2005.

[18] Y. Yan, S. B. Zhang, and S. T. Pantelides. Control of doping by impurity chemical potentials: Predictions for *p*-type zno. *Physical Review Letters*, 86(25):5723–5726, Jun 2001.

[19] Z. W. Liu, C. K. Ong, T. Yu, and Z. X. Shen. Catalyst-free pulsed-laser-deposited ZnO nanorods and their room-temperature photoluminescence properties. *Applied Physics Letters*, 88(5):053110, 2006.

[20] X. M. Fan, J. S. Lian, L. Zhao, and Y. H. Liu. Single violet luminescence emitted from ZnO films obtained by oxidation of Zn film on quartz glass. *Applied Surface Science*, 252(2):420–424, 2005.

[21] B. J. Jin, S. Im, and S. Y. Lee. Violet and UV luminescence emitted from ZnO thin films grown on sapphire by pulsed laser deposition. *Thin Solid Films*, 366(1-2):107–110, 2000.

Chapter 6

Results & Analyses: Biomedical Application of ZnO Thin Film

In this chapter, we present the work done on utilising ZnO thin films as an extension of previous studies in biomedical applications. Zinc oxide is a highly versatile material with numerous attractive physical and chemical properties contributing to applications in many domains of science and technology as earlier mentioned. Our focus for this work was to use ZnO thin films to inactivate a biofilm, namely *Staphylococcus epidermidis*, under UV illumination.

This work was formed as a collaboration of our research and that done by another group working with titanium dioxide. TiO_2 is a semiconductor with anatase or rulite crystalline structures [1] that uses photocatalytic chemistry to make it a powerful disinfectant. The basic principle of this technique consists of illuminating the semiconductor surface with band gap light to create valence band holes which have a sufficiently positive potential to oxidise organic matter directly or to oxidise water yielding hydroxyl ($OH^{\bullet}$) and/or other radicals ($O_2^{-\bullet}$, $HO_2^{\bullet}$) with known bactericidal properties, for example, see Refs [2–7]. Anatase/rulite TiO_2 remains the most widely used and studied photocatalyst material and recent fundamental studies have demonstrated that the surface

defects such as oxygen vacancies mediate the dissociation of water on its surface [8]. Despite this, one main drawback noted in recent works point to doped TiO_2 for optimum performance which requires the implementation of comparatively more complex deposition methods [9]. Furthermore, titanium dioxide has been recently classified as possibly carcinogenic to humans [10]. Therefore there is all the more need to use alternative oxide semiconductors for photocatalytic applications.

ZnO is well known to have antibacterial properties, as studied in powder or nanoparticle form [11–15], and this effect can be further enhanced by ultraviolet light activation [16]. Nanostructured ZnO has interesting properties towards the photocatalytic decomposition of organic pollutants [17] and dyes [18] while La-doped and saline-coated ZnO nanoparticles have recently shown remarkable photocatalytic action against monocrotophos [19] and tetrachloroethylene [20]. Several studies have compared the effectiveness of the photocatalytic properties of ZnO for the inactivation of several pathogens with that of various metallic oxides and demonstrated that ZnO is highly effective in this context [16, 21, 22]. These works suggest the use of ZnO coatings for the inactivation of biofilms, a subject which had remained unexplored at the time of this study.

The choice of biofilm the collaborators were working with was *S. epidermidis* because, as it was once regarded as a harmless part of the skin flora, it is now accepted as a major nosocomial pathogen. To date, to prevent the formation of *Staphylococcus epidermidis* biofilms, new techniques using silver-doped phenyltriethoxysilane sol-gel coatings [23] or antibiotic-loaded titania nanotubes [24], for example, have been successfully tested.

ZnO with its active surface sites, strong photoeffects, and antibacterial properties combined with the comparatively time- and cost- effective technique of pulsed laser deposition made this unexplored topic a fruitful area of research. In this chapter we show that an optically thick ZnO film deposited at room temperature by PLD onto a soda-lime glass substrate can be used to inac-

tivate a biofilm of *S. epidermidis* grown directly on the ZnO surface when back-illuminated with above band gap UV radiation (around 376 nm). This technique has potential for the disinfection of contaminated surfaces and inner-surfaces, which is a topic of great practical importance [24]. In the following sections, we first present our experimental set-up and the conditions used for bacterial inactivation. We then present data on the characterisation of the ZnO films both before and after UV illumination with a view to identify some relevant physical and chemical systems. Finally, we propose a model to explain the bacterial inactivation that accounts for all the experimental observations.

6.1 Sample Preparation

The samples for the experiments throughout this chapter of work were deposited by a growth procedure modified from those of previous experiments. The motivation behind this change in the growth procedure as detailed below came from the result of using glass as a substrate. In this section, the growth and preparation of the samples is described.

6.1.1 Preparation of ZnO Film

Standard, soda lime glass microscope slides were prepared as substrates for deposition by standard cleaning using acetone and IPA. Additionally, a piece of tantalum foil was used to mask each half of the rectangular, glass slide lengthwise, as to create half-ZnO coated samples. The glass slide substrates were then mounted in the chamber and the chamber was evacuated to base pressure. An oxygen background gas was then introduced to bring the pressure up to 3.5×10^{-1} mbar. The substrates were not heated during the growth of these ZnO films. The Nd:YAG laser beam (λ = 266 nm, τ = 6 nm) was focused to deliver an energy fluence of approximately 1.3 J/cm^2. At a rate of

10 Hz, 36,000 shots of ZnO material were deposited onto the substrate with a corresponding layer thickness of approximately 2 μm. The samples were then withdrawn from the chamber and the tantalum foil was removed. Half of them were saved as 'as-grown ZnO' reference samples for characterisation; the other half were then prepared for the cultivation of the biofilm over both halves of the sample, as detailed in the following section.

6.1.2 Cultivation of Biofilm

In this next step, the half-coated ZnO/glass slides first required sterilisation by exposing them to UVC light to ensure no foreign dust or organisms accidentally contaminated the sample during *ex-situ* transportation. They were then placed in a sterile Petri dish where 10 mL of Brain-Heart Infusion (BHI) broth was added. The BHI broth was prepared in advance and is a solution of BHI agar, which is commonly used to cultivate microorganisms, and a strain of *Staphylococcus epidermidis*. The reference strain of *Staphylococcus epidermidis* RP62A (ATCC 35984) was resuscitated using a BHI agar plate (CM0225, Oxoid Ltd. UK) and then heated overnight at 37 °C. The Petri dish containing both our sample and BHI broth were then inoculated for 18 hours to a standardised cell suspension of 10^6 Colony Forming Units per mL. Afterwards, the samples were rinsed clean three times with sterile, deionised water to remove any residual broth or planktonic cells that cultivated in the broth itself and not on the sample surface. At this point, each glass substrate in this set of samples was now half coated with ZnO first and fully coated with a biofilm afterwards. These samples were then ready to be tested for the effect the ZnO layer had on the biofilm after they were exposed to UV light.

6.2 ZnO/Biofilm Sample Irradiation

As of now, each half of the glass microscope slide is either the test sample or the control sample where: (1) the test sample is glass coated with ZnO then coated with biofilm, and (2) the control sample is glass coated only with the biofilm. In this way, each pair of slides were prepared identically but can be individually tested without question to see the effects of the ZnO layer on the bacteria.

The samples were irradiated in a custom made, divided cell, constructed of Perspex, and specifically designed to vertically suspend a pair of slides immersed in a fluid (distilled water). Each of the two slides were suspended in either half of the divide (and, recall, each slide is half coated with ZnO and then fully coated with a biofilm). One half of the cell had a window made of fused quartz to allow the irradiating ultraviolet light through while the other half of the cell was completely light tight. Thus, one sample was kept in the dark while the other was irradiated by the UV light (and both in the distilled water) as depicted in Fig. 6.1. The sample exposed to the UV light was irradiated with the glass surface positioned towards the UV source. All directionality further discussed will be in the direction of the UV light propagation, i.e. the biofilm will be the last layer the light contacts. The light source used was a low pressure mercury vapour lamp (UVA lamp PL-S 9W/10, Philips, Aylesbury, UK). The lamp emits long wave UVA radiation in the 350 - 400 nm region and peaks at around 365 nm (100% intensity) with a FWHM of roughly 20 nm (360 nm - 380 nm). It has a UVA/UVB ratio of less than 0.1% and operates at an intensity of 14 W/m^2. The 'back illuminated' sample was irradiated for 2 hours in distilled water while the other sample was similarly submerged but completely sealed in the dark for the same duration.

In summary, after the 2 hours, this bacterial inactivation experiment had produced a total of 4 testable regions - an experimental and control from each

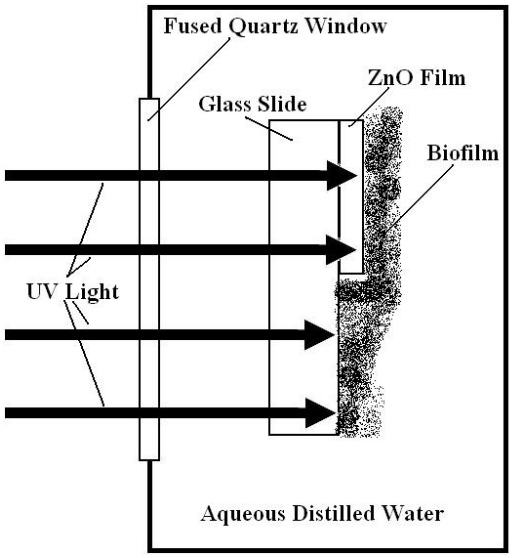

Figure 6.1: Diagram showing the back-illumination of glass slide half-coated with ZnO and fully covered by a layer of *S. epidermidis* bacteria. The UVA light entered from a light source outside the bath chamber (filled with distilled water) through a quartz glass window. Note that the sample is fully and evenly illuminated.

of the pair of samples. The first of the 2 glass samples was isolated from any light source, yielding: (i) a glass/ZnO/biofilm region without UV exposure, and (ii) a glass/biofilm region without UV exposure. The other, UV treated, glass sample yielded: (iii) a glass/ZnO/biofilm region with UV exposure, and (iv) a glass/biofilm region with UV exposure.

6.3 ZnO/Biofilm Sample Characterisation

The pair of UV treated and untreated samples were first to be prepared for testing the viability of the biofilm under each of the previously mentioned four regions. They were stained using a LIVE/DEAD BacLight Bacterial Viability kit L-13152 and then optically imaged with an LSM510 META Axopan upright confocal scanning laser microscope. The viability kit was comprised of two nucleic acid stains: (1) an STYO 9 (excitation maximum, 508 nm; emission

maximum, 528 nm), a lipophilic membrane permeable cationic stain that labels live bacterial with green fluorescence, and (2) propidium iodide (excitation maximum, 536 nm; emission maximum, 620 nm) a membrane impermeable anionic stain that labels membrane-compromised bacteria with red fluorescence. On its own, STYO 9 stains both live and dead bacteria, whereas propidium iodide penetrates only cells with compromised cell membranes. This staining method has been used extensively as a viability indicator, eg [25–27].

Randomly selected areas of each sample were then observed with the contrast microscope. Confocal illumination was provided by an argon-ion laser (with an excitation wavelength of 488 nm) fitted with a 505 - 550 nm band pass emission filter for detection of the green fluorescence of the STYO 9, and a HeNe laser (with an excitation wavelength of 543 nm) fitted with a 585 - 615 nm band pass emission filter for detection of the red fluorescence of the propidium iodide. A resulting contrast image was a combined image showing either red (dead) or green (living) stained bacterial cells. Three (or in some cases four) images were selected at random for the ZnO coated and uncoated regions on both the UV exposed and unexposed samples. From each image, the red and green cells were hand counted and the percentage viability calculated as an average over the 3 (or 4) images for each region. On average, there were between 800 - 1000 cells per image.

After viability test images of the stained biofilm were captured, the samples were then treated with a disinfectant and rinsed with sterile water for further testing of the ZnO film surface. The as-grown set of ZnO films set aside earlier were also tested along with the UV treated samples for comparison. The ZnO surfaces of both as-grown and UV treated samples were imaged with SEM and AFM. The crystalline properties of both the as-grown and UV treated ZnO films were then investigated. To determine the optical transmission before and after treatment, a double-beam UV-vis spectrophotometer was used (in the same configuration as in the UV irradiation experiment) to measure the ZnO

UV Irradiation	Cell Viability (%)		P value
	Test Sample (ZnO Coating)	Control Sample (Without ZnO Coating)	
Without Exposure	70 ± 13	87 ± 6	$P > 0.05$
With Exposure	30 ± 12	83 ± 4	$P < 0.01$

Table 6.1: Comparison of cell viability (%) of *S. epidermidis* biofilms grown on ZnO coatings with or without exposure to UV lamp radiation (14 W/m^2, UVA 350 - 400 nm) for 2 hours and P values from one-way ANOVA.

films' transmissions in the 300 nm - 700 nm wavelength range. X-ray photoelectron spectroscopy was also used on both sets of samples to determine any change in the stoichiometry of the ZnO surfaces. Finally, Raman spectroscopy was preformed on the as-grown and post-UV treated ZnO films to detect any change in defect or impurity concentration.

The results of these characterisations are detailed and analysed throughout the next section.

6.4 Results & Analyses

6.4.1 Bacterial Viability

A representative selection of images obtained from the confocal laser scanning microscope (CLSM) are presented in Figure 6.2(a)-(d) for the respective regions (i)-(iv) previously mentioned. The data for the cell viability and additional analyses on variance (ANOVA) of this data are produced in Table 6.1. For the data analysed by one-way ANOVA, the probability values (or P-values) of less than 0.05, 0.01, or 0.001 are generally considered to be respectively significant, highly significant, or extremely significant. The p-value is the probability that the result of an experiment is statistically relevant to the hypothesis, in this

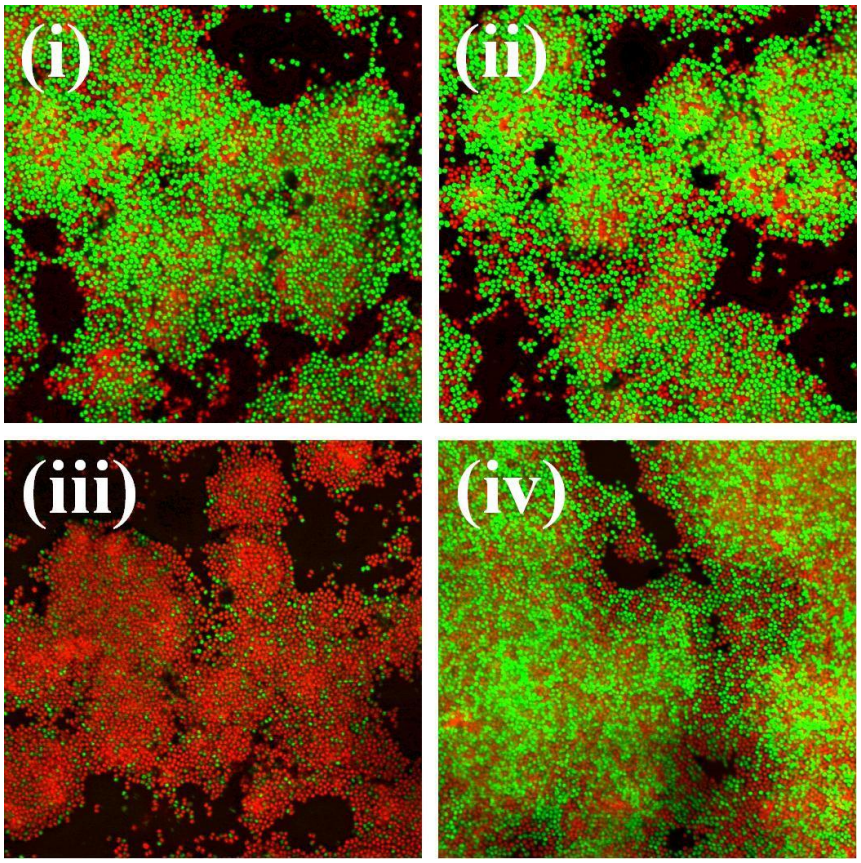

Figure 6.2: Fluorescence images showing results from bacteria viability stains. The green and red stains respectively indicate living bacteria and membrane compromised bacteria. Quadrants (i) a glass/ZnO/biofilm region, and (ii) glass/biofilm region were both unexposed to UV light, whereas quadrants (iii) a glass/ZnO/biofilm region, and (iv) glass/biofilm region were both exposed to UV illumination.

case, the effect the ZnO coating has on the viability of the bacteria. The smaller the value, the more significant an effect the ZnO has on the viability. As the data shows, 83 $\pm$ 4 % of the cells were viable after 2 hours exposure to UVA on the uncoated portion of the sample as opposed to the 30 $\pm$ 12 % on the ZnO coated portion. The coating in this case had shown a highly significant effect on viability ($P < 0.01$) as determined from the one-way ANOVA. On the other hand, the samples isolated in darkness for 2 hours were 87 $\pm$ 6 % and 70 $\pm$ 13 % viable for the uncoated and coated portions respectively, with an

insignificant effect on viability ($P > 0.05$).

The results of this viability test imply four things: (1) *S. epidermidis* does grow on ZnO as well as the glass, (2) ZnO does show slight natural inactivation of the biofilm consistent with previously reports of its antibacterial properties, (3) neither the ZnO nor the UV exposure is independently responsible for the significant bactericide of the biofilm, but the combination are, and lastly (4) UVA exposure initiates the release of active species on the ZnO surface as indicated by the stains ability to penetrate only membrane compromised cells.

6.4.2 Surface Imaging

SEM and AFM imaging were preformed on the as-grown ZnO reference sample, shown respectively in Figures 6.3(a) and 6.4(a). The samples which had

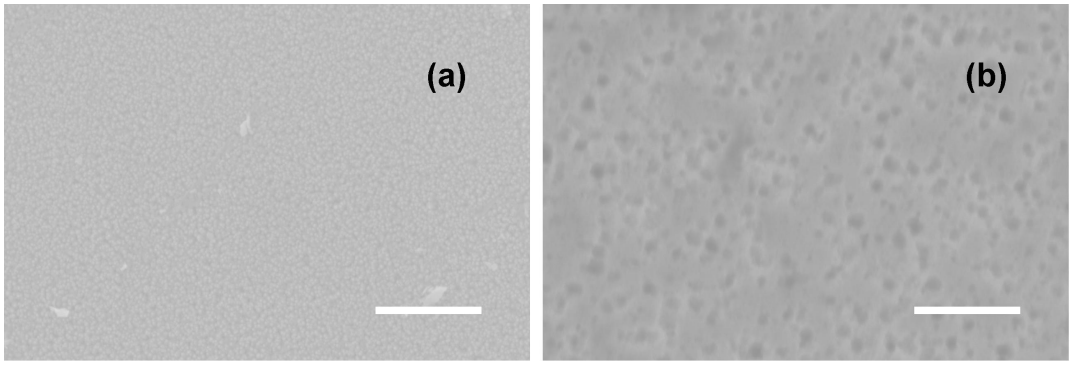

Figure 6.3: SEM images of the (a) as-grown ZnO surface and (b) ZnO surface after UV treatment and removal of biofilm. The scale bars represent 5 μm for both images.

undergone biofilm growth and UV treatment, were sterilised and also imaged with SEM and AFM (Figures 6.3(b) and 6.4(b), respectively). This way, the effects the experiment had on the ZnO surface can be directly compared to its as-grown state. The SEM images of the as-grown ZnO showed a uniform grain-like microstructure, but after the sample was UV treated, it displayed micron-sized pits evenly distributed across the ZnO surface. These images

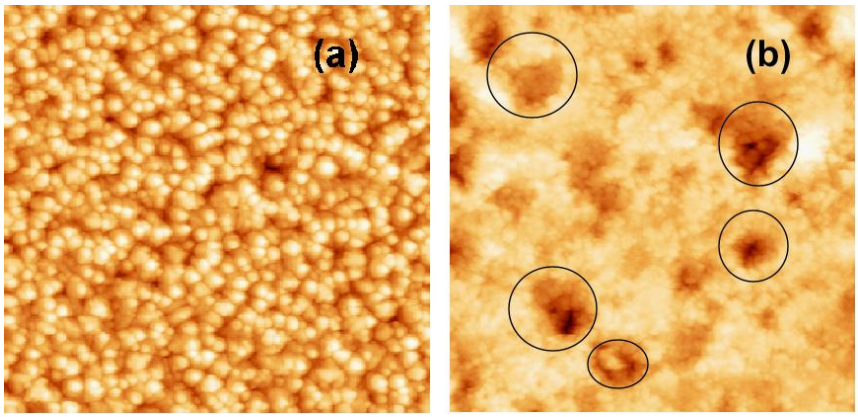

Figure 6.4: AFM images of the (a) as-grown ZnO surface and (b) ZnO surface after UV treatment and removal of biofilm. The black circles show micron-sized pitting described in text. Each image is $5 \times 5\ \mu m^2$ in size.

imply that the ZnO was decomposed due to the *S. epidermidis* in conjunction with the UV exposure.

From the AFM imaging, it was found that RMS roughness of the as-grown ZnO film was 49.7 nm with a grain height of 231.7 nm. After the experiment was carried out, these valuse increased, respectively, to 68 nm and 401.5 nm. These increases in the surface roughness and the grain heights infer a degradation of the ZnO thin film following the treatment. The micron-sized pits with diameters of 0.5 μm - 1.0 μm and depths of 0.4 μm also agree with this idea. These pits could be localised sites of accelerated degradation during the UV irradiation step.

6.4.3 X-ray Diffraction

X-ray diffraction θ-2θ scans (Figure 6.5) were carried out on both the as-grown and UV treated ZnO samples. It can be seen that the as-grown ZnO film grew predominantly in the $[000l]$ and $[10\bar{1}1]$ directions. The successful growth of crystalline, ZnO films on an amorphous (glass) substrates at room temperature is a noteworthy point [28]. The crystallinity of the ZnO films were also affected

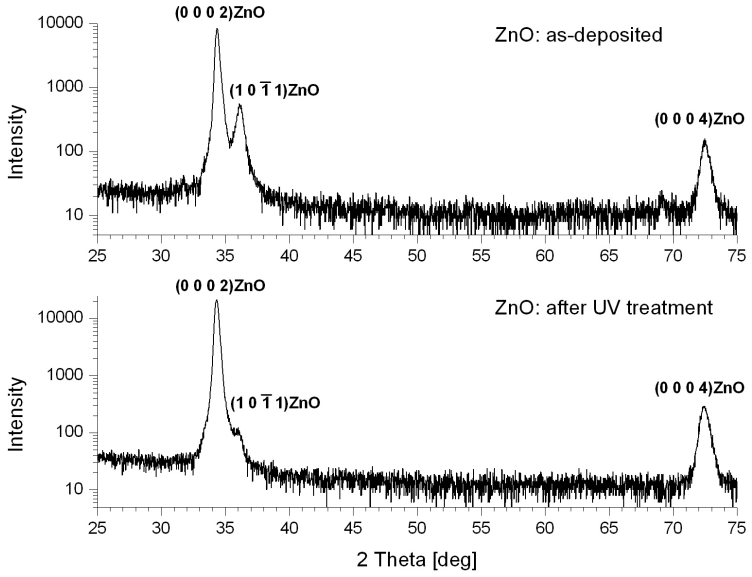

Figure 6.5: XRD θ-2θ scan of ZnO as-grown on a glass substrate (top) and of the ZnO film after UV treatment (bottom).

by the UV treatment as seen by the lessened intensities of the ZnO $(000l)$ peak and significantly diminished $(10\bar{1}1)$ peak. Again, it is apparent some form of interaction during the UV exposure was the cause of such physical and crystalline deterioration.

Two pieces of information can be extracted from this data: (1) the ZnO grown via PLD at room temperature was crystalline on a glass substrate, and (2) there was a noticeable degradation of the crystallinity of the ZnO film after the UV irradiation.

6.4.4 UV-vis Absorption Spectroscopy

Figure 6.6 shows the UV-vis transmission spectra of the ZnO films on glass for both the as-grown and post-UV treated samples. Both spectra exhibit an absorption region just beyond 368 nm – the band gap region of ZnO. The as-grown ZnO sample had about 0.2% transmission below the ZnO band gap and

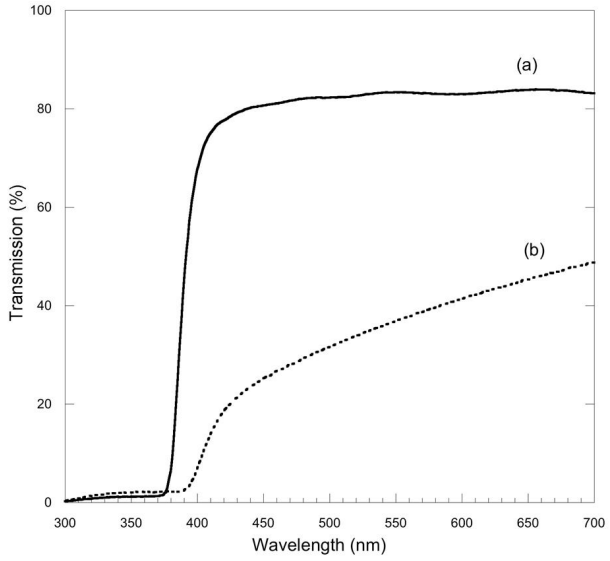

Figure 6.6: Optical transmission spectra for (a) as-grown and (b) UV treated and cleaned ZnO films.

roughly 85% transmission in the 400 nm - 700 nm region. The ZnO sample that had undergone UV treatment displayed a more gradual, non step-like behaviour, unlike the as-grown ZnO sample, in the same 400 nm - 700 nm region. This was noticeable to the naked eye, as the sample without UV exposure was visibly transparent yet the treated sample was a yellowish-milky colour. From these observations, two conclusions can be drawn: (1) band gap photons, i.e. with energies large enough to generate electron-hole pairs, were able to penetrate and traverse the thickness of the $\sim$2 μm thick ZnO film, and (2) further evidence that the UV treatment was leading to a chemical change in the ZnO layer itself.

It has been reported [29] that the exciton diffusion length in ZnO is to be within the range of 0.5 μm - 2 μm and this is directly comparable to the thickness of the ZnO layer grown on the glass substrate. Therefore, it is not unlikely that the electron-hole pairs generated at the glass/ZnO interface allow for holes to migrate to the polar (0001)-Zn surface. These holes, now at

the ZnO/biofilm interface, are the probable candidates behind the optical and structural degradation of the ZnO film thus observed, and more importantly, the bactericidal phenomenon observed.

The UV-vis transmission spectrum for this sample provides a clue for helping further understand what role the electron-holes play at the interface during the UV exposure. The same gradual, non step-like behaviour observed in the UV-treated ZnO film was notably similar to UV-vis absorption spectra of zinc peroxide [30, 31], both prepared by a sol-gel method. Furthermore, both groups show the absorbance spectra of the ZnO nanoparticles decomposed from the ZnO_2 powder is similar to the characteristic step-like transmission spectrum of the as-grown ZnO spectra displayed in Figure 6.6. These facts give new insight into what chemical processes are possibly occurring at the ZnO/biofilm interface. During the UV irradiation, it is unconfirmed, but not unlikely, that hole diffusion to the interface causes ZnO to oxidise into a peroxide.

6.4.5 XPS

To better understand the effects observed both physically and experimentally, further analysis of the ZnO surface was needed. X-ray photoelectron spectroscopy (XPS) was carried out on the ZnO surfaces of both the in-dark and UV-exposed samples which were suspended in distilled water for the 2 hour duration of the experiment. (Before analysing the ZnO, the surfaces were thoroughly washed clean of and sterilised for any remaining biofilm.) In this way, the sample left in darkness will be a reference for the effects the biofilm, distilled water, and cleaning had. Since XPS specifically penetrates up to depths of 10-100 Å, any change in the chemical composition of the ZnO at the biofilm/ZnO interface would be detected. Figure 6.7 shows the XPS binding energy spectra (in eV) of the the ZnO films, respectively, without and with UV exposure. The spectra display the binding energy in the O 1s region, which has been refer-

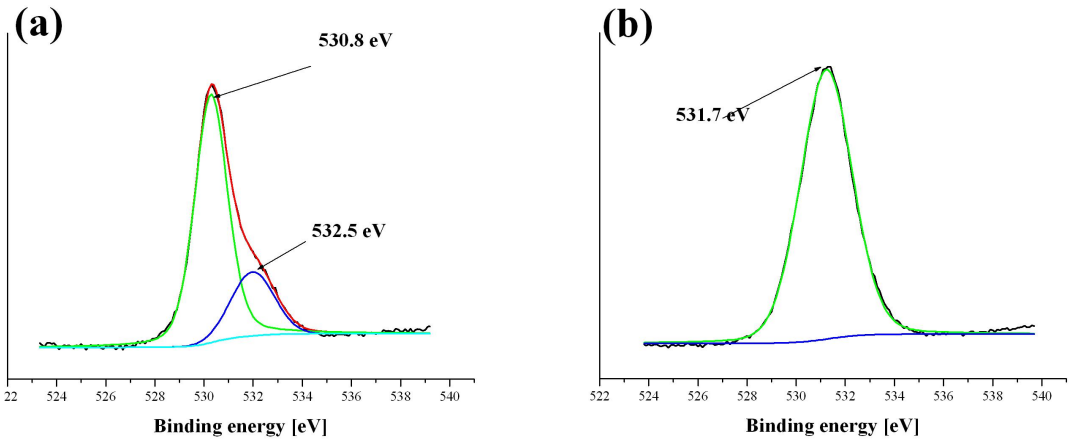

Figure 6.7: XPS of (a) an as-grown ZnO film and (b) a UV treated and cleaned film in the region of the O 1s binding energy. The spectra was referenced to the C 1s binding energy taken at 285.0 eV.

enced to the C 1s binding energy taken at 285.0 eV. We note in both cases, the spectra showed virtually no angular dependence, which indicates the absence of strongly surface-localised components. The XPS data were analysed with the help of peak fitting software that assumes a non-linear background and a combination of Lorentzian and Gaussian line shapes (Voigt profiles) for the fitting peaks.

In the reference sample of ZnO left in darkness (Figure 6.7(a)), two lines were fitted to this spectral feature, peaking at 530.8 eV and 532.5 eV having relative intensities of 77% and 23%, respectively. The ZnO film which had undergone UV treatment had a single peak fit with a maximum at 531.7 eV (Figure 6.7(b)). Spectra were also measured in the region of the Zn $2p_{2/3}$ binding energy and showed identical pure Lorentzian line shapes with maxima at 1022.4 eV and 1022.6 eV for the respective reference and UV treated samples. This indicates no significant core level shifts or line shape changes for the Zn in either sample. Therefore, the relative intensity ratios of Zn and O electron peaks yield the stoichiometric molecular formulae values of $ZnO_{0.95}$ and $ZnO_{2.2}$, respectively for the reference and UV treated samples. This data substantiates

the previous evidence that structural and optical degradation are indeed occurring at a chemical level at the biofilm/ZnO interface, and, furthermore, are not caused by the biofilm, aqueous solution, or sterilisation independently.

The XPS spectrum of ZnO has been measured and interpreted by numerous authors [32–35] which have carried out systematic XPS studies of metal oxides such as ZnO, hydroxides, and peroxides in highly controlled experimental conditions. We follow these works in the interpretation of the O 1s XPS data presented in Figure 6.7 for an understanding of the mechanics at work at the biofilm/ZnO interface during the UV exposure. For the reference sample, the strong low-energy component at 530.8 eV corresponds to the O^{2-} of the wurtzite ZnO structure, while the 532.5 eV component corresponds to the oxygen in a lower ionisation, eg O^{-} species, that is supposed to result from the compensation of charge deficiencies in the substrate of the metal oxide [35]. In the UV treated sample, the component 531.7 eV corresponds to oxygen integrated in the material with ionisation characteristic of OH^{-} (hydroxide) species or O_2^{2-} (peroxide) species. The interpretation of this XPS data concurs with published works which establish active surface defect sites on the ZnO structure, such as oxygen vacancies V_O, in addition to its potent catalytic properties and strong photoeffects [36]. These were revealed in the present experiments carried out in an aqueous environment, in the form of the net oxidising effect of the UV irradiation of ZnO films.

The XPS data is indicative of a definite chemical decomposition at the biofilm/ZnO interface while in an aqueous solution during UV exposure. The notion for the possible cause of the observed degradation in the ZnO film may be due to both (1) the change of the stoichiometric ratio, and (2) the shift of the O 1s binding energy to 531.7 eV.

These compliment the results mentioned in the UV-vis data and expands this notion into a probable simultaneous, two-step process. During the UV irradiation, when electron-hole pairs are created, holes migrate towards the

polar Zn^{+} surface creating the measured O_2^{2-} species as well as the OH^{-} species, both attributed to the binding energy peak at 531.7 eV. As the electron-holes oxidise the ZnO into $ZnO_{2.2}$, the peroxide species are likely produced, and as they react with the surrounding aqueous solution likely forming the hydroxide species. Additionally, studies showed photo-holes can oxidise bacterial organic matter [19, 20], as was the *S. epidermidis* biofilm in the viability test. Thus, the electron-holes are simultaneously acting as both a reducer and an oxidiser at the interface.

6.4.6 Raman Spectroscopy

Lastly, Figures 6.8(a) and 6.8(b) show the Raman spectra of ZnO-coated substrates both as-grown, and after the microbial and UV light interactions respectively. In both samples, three weak Raman bands can be distinguished

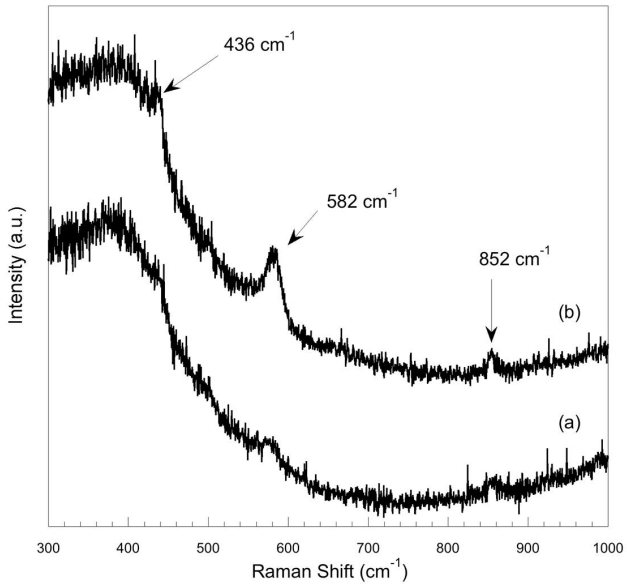

Figure 6.8: Raman spectra of (a) as-grown ZnO and (b) UV treated and cleaned ZnO films on a glass substrate.

above the the noise at 436 cm^{-1}, 582 cm^{-1}, and 852 cm^{-1}, which have been previously reported in literature [37, 38]. The band at 436 cm^{-1}, can be readily

attributed to the allowed E_2(high) phonon mode of ZnO. The 582 cm^{-1} and 852 cm^{-1} are described as anomalous Raman modes variously attributed (see discussion in [37]) to local vibrational modes of defects, impurities, or silent ZnO modes allowed by the breakdown of crystal symmetry induced by defects or impurities. As seen in Figure 6.8(b), these two bands are enhanced in the spectrum, indicating the UV treatment has likely increased the defect/impurity concentrations of the ZnO film in our experiments with respect to the reference sample. This also corroborates with the observed effects and results discussed in the preceding sections.

Additionally, the band found a 852 cm^{-1} has been similarly reported in conjunction with a band near 436 cm^{-1} in Raman spectrum of ZnO_2 samples. For example, Uekawa *et al.* [31] observed two bands (at 435 cm^{-1} and just above 840 cm^{-1}) in their Raman spectrum of ZnO_2 powder fired at 473 K for two hours. The authors attributed the former to the allowed E_2(high) mode of ZnO while the latter was assigned to a stretching mode of the peroxide ion O_2^{2-} contained in the ZnO lattice [39]. Similarly, Sun *et al.* [30] prepared ZnO_2 using a sol-gel method and also observed an unknown Raman band near 840 cm^{-1} which they attributed to ZnO_2. These results further support previous conclusions regarding the band measured at 852 cm^{-1} in our spectra and suggest that the extra oxygen incorporated in the ZnO film during the UV/bacterial processing thereby caused the increase in the defect concentration. With that said, this is only one such hypothesis that does happen to corroborate with the rest of the data. Other explanations could be found possible with further extensive testing.

6.5 Conclusions

In this study, ZnO was grown as a crystalline thin film on a soda lime glass substrate via pulsed laser deposition. A bacterial biofilm of *S. epidermidis*

was grown over the ZnO thin film, submersed in an aqueous solution, and then back-illuminated by a UVA light source for a duration of 2 hours. It had been observed that the UV exposure significantly effected the viability of the biofilm solely adherent to the ZnO film. As previously mentioned, it had been reported that zinc oxide films have been used for their photocatalytic properties. Through general observations and *ex situ* measurements, a model has been developed for the apparent photocatalytic disinfection/inactivation at the ZnO/biofilm site in an aqueous solution in this study.

To construct the model for this bactericidal activity, it must first be recalled that the samples are illuminated by the UVA light source from the backside of the sample, i.e. passing through the glass and into the ZnO along the crystalline [000l] axis. As earlier mentioned, ZnO is a polar material and has grown such that the Zn^+ surface is towards the c-axis direction of growth. As the sample is back-illuminated, the UV interaction at the glass/ZnO interface creates electron-hole pairs. The photo-holes, found capable of penetrating the full thickness of the 2μm thick ZnO during the UV-vis absorption experiment, migrate towards the Zn^+-polar surface, i.e. the ZnO/biofilm interface. See diagram in Figure 6.9.

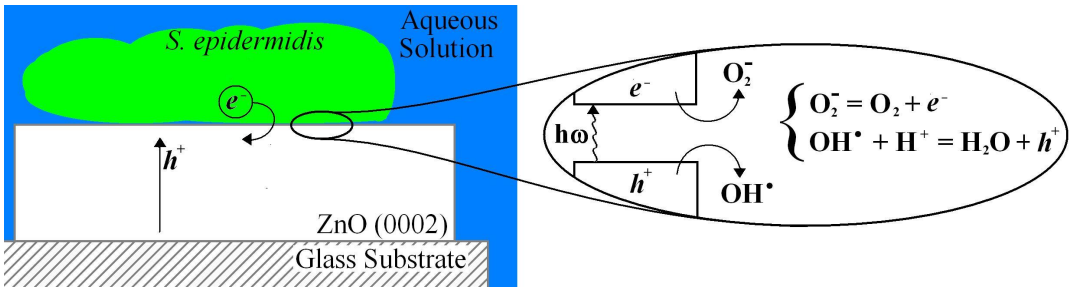

Figure 6.9: Diagram of redox-reaction site at the ZnO/biofilm interface in an aqueous solution and the corresponding band diagram indicating the formation of hydroxyl radicals and oxygen species which ultimately compromise cell membranes in the biofilm.

At this point, it is proposed that the photo-holes act as a catalyst for a

number of redox reactions that occur simultaneously. First and foremost, the photo-holes directly oxidise the bacterial film in accordance to Rohe *et al.* and Anandan *et al.* at the ZnO/biofilm interface [19, 20]. Secondly, as the sample is in an aqueous environment, the holes can alternatively oxidise water to produce hydroxyl $OH^{\bullet}$ radicals which can trigger a series of chemical reactions leading to reactive oxygen species, such as superoxide ($O_2^{\bullet}$) or peroxide (O_2^{2-}) radicals as shown by X. Domènech *et al.* [40]. Evidence of these species have been observed in the data from both the x-ray photoelectron and Raman spectroscopies. These species have potent anti-bactericidal properties. Thirdly, J. Doménech and A. Prieto [41] have also shown that a likely product following the initial formation of $OH^{\bullet}$ in an aqueous solution is hydrogen peroxide (H_2O_2). H_2O_2 and ZnO are known to react to produce zinc peroxide [40], which is again in agreement with the results determined from UV-vis, XPS, and Raman data, and additionally, would account for the crystalline deterioration seen in the XRD data. The absence of any typical ZnO_2 peaks in the XRD data does not conflict with the optical data because the structure of the as-grown ZnO displayed weaker intensities than those of typical crystalline ZnO films. Thus, the degradation of the already misaligned ZnO crystallites would be observed, but the emergence of ZnO_2 crystallites would not likely be large or aligned enough to be detected above the noise. Lastly, UV illumination of ZnO is also known to lead to a photolysis of the ZnO lattice whereby oxygen gas is released, leaving behind very active oxygen vacancies [36, 41] which were also interpreted as reduction sites from the XPS data. Bikondoa *et al.* [8] have shown unambiguously that such oxygen vacancy sites mediate the photodissociation of water on the surface of TiO_2. Therefore, it is reasonable to assume that such a process may occur similarly in this model since a small fraction of the UV light can penetrate the ZnO film to the surface.

The experimental data presented, which contrasts the as-grown reference ZnO film to the UV treated film, actively support this model. Raman data

showed the possible degradation of the ZnO lattice structure from the presence of defects such as extra oxygen. XPS data show that these extra stoichiometric oxygen were incorporated into the ZnO film during a surface reduction reaction throughout the UV exposure. The UV-vis transmission data showed a possible evolution of ZnO being effectively oxidised to ZnO_2. Finally, the physical surface as seen in the SEM and AFM are also in agreement with the model. Post-treatment, they both exhibit roughened surfaces with "micropitting" likely due to active surface sites playing a role in the photocorrosion of the lattice.

References

[1] K. Hashimoto, H. Irie, and A. Fujishima. TiO_2 photocatalysis: A historical overview and future prospects. *Japanese Journal of Applied Physics*, 44(12):8269–8285, 2005.

[2] T. A. McMurray, J. A. Byrne, P. S. M. Dunlop, and E. T. McAdams. Photocatalytic and electrochemically assisted photocatalytic oxidation of formic acid on TiO_2 films under UVA and UVB irradiation. *Journal of Applied Electrochemistry*, 35(7/8):723–731, 2005.

[3] K. Sunada, T. Watanabe, and K. Hashimoto. Bactericidal activity of copper-deposited TiO_2 thin film under weak UV light illumination. *Environmental Science and Technology*, 37(20):4785–4789, 2003.

[4] M. Machida, K. Normoto, and T. Kimura. Antibacterial activity of photocatalytic titanium dioxide thin films with photodeposited silver on the surface of sanitary ware. *Journal of the American Ceramic Society*, 88(1):95–100, 2005.

[5] Y. Kikuchi, K. Sunada, T. Iyoda, K. Hashimoto, and A. Fujishima. Photocatalytic bactericidal effect of TiO_2 thin films: Dynamic view of the active oxygen species responsible for the effect. *Journal of Photochemistry and Photobiology A: Chemistry*, 106(1-3):51–56, 1997.

[6] E. F. Duffy, F. Al Touati, S. C. Kehoe, O. A. McLoughlin, L. W. Gill, W. Gernjak, I. Oller, M. I. Maldonado, S. Malato, J. Cassidy, R. H. Reed,

and K. G. McGuigan. A novel TiO_2-assisted solar photocatalytic batch-process disinfection reactor for the treatment of biological and chemical contaminants in domestic drinking water in developing countries. *Solar Energy*, 77(5):649–655, 2004.

[7] Z. Huang, P.-C. Maness, D. M. Blake, E. J. Wolfrum, S. L. Smolinski, and W. A. Jacoby. Bactericidal mode of titanium dioxide photocatalysis. *Journal of Photochemistry and Photobiology A: Chemistry*, 130(2-3):163–170, 2000.

[8] O. Bikondoa, C. L. Pang, R. Ithnin, C. A. Muryn1, H. Onishi, and G. Thornton. Direct visualization of defect-mediated dissociation of water on TiO_2(110). *Nature Materials*, 5(3):189–192, 2006.

[9] M. Maeda and T. Watanabe. Visible light photocatalysis of nitrogen-doped titanium oxide films prepared by plasma-enhanced chemical vapor deposition. *Journal of The Electrochemical Society*, 153(3):C186–C189, 2006.

[10] R. Baan, K. Straif, Y. Grosse, B. Secretan, F. El Ghissassi, and V. Cogliano. Carcinogenicity of carbon black, titanium dioxide, and talc. *The Lancet Oncology*, 7(4):295–296, 2006.

[11] W. R. Moorer and J. M. Genet. Antibacterial activity of gutta-percha cones attributed to the zinc oxide component. *Oral Surgery, Oral Medicine, Oral Pathology*, 53(5):508–517, 1982.

[12] O. Yamamoto, M. Komatsu, J. Sawai, and Z. Nakagawa. Effect of lattice constant of zinc oxide on antibacterial characteristics. *Journal of Materials Science: Materials in Medicine*, 15(8):847–851, 2004.

[13] O. Yamamoto. Influence of particle size on the antibacterial activity of

zinc oxide. *International Journal of Inorganic Materials*, 3(7):643–646, 2001.

[14] K. Ghule, A. V. Ghule, B.-J. Chen, and Y.-C. Ling.

[15] N. Padmavathy and R. Vijayaraghavan. Enhanced bioactivity of ZnO nanoparticles — an antimicrobial study. *Science and Technology of Advanced Materials*, 9(3):035004–035510, 2008.

[16] H.-L. Liu and Thomas C.-K. Yang. Photocatalytic inactivation of *Escherichia coli* and *Lactobacillus helveticus* by ZnO and TiO_2 activated with ultraviolet light. *Process Biochemistry*, 39(4):475–481, 2003.

[17] C. Hariharan. Photocatalytic degradation of organic contaminants in water by ZnO nanoparticles: Revisited. *Applied Catalysis A: General*, 304:55–61, 2006.

[18] C. Ye, Y. Bando, G. Shen, and D. Golberg. Thickness-dependent photocatalytic performance of ZnO nanoplatelets. *Journal of Physical Chemistry: B*, 110(31):15146–15151, 2006.

[19] B. Rohe, W. S. Veeman, and M. Tausch. Synthesis and photocatalytic activity of silane-coated and UV-modified nanoscale zinc oxide. *Nanotechnology*, 17(1):277–282, 2006.

[20] S. Anandan, A. Vinu, K. L. P. S. Lovely, N. Gokulakrishnan, P. Srinivasu, T. Mori, V. Murugesan, V. Sivamurugan, and K. Ariga. Photocatalytic activity of La-doped ZnO for the degradation of monocrotophos in aqueous suspension. *Journal of Molecular Catalysis A: Chemical*, 266(1-2):149–157, 2007.

[21] O. Seven, B. Dindar, S. Aydemir, D. Metin, M. A. Ozinel, and S. Icli. Solar photocatalytic disinfection of a group of bacteria and fungi aqueous

suspensions with TiO_2, ZnO and Sahara desert dust. *Journal of Photochemistry and Photobiology A: Chemistry*, 165(1-3):103–107, 2004.

[22] J. Sawai. Quantitative evaluation of antibacterial activities of metallic oxide powders (ZnO, MgO and CaO) by conductimetric assay. *Journal of Microbiological Methods*, 54(2):177–182, 2003.

[23] N. Stobie, B. Duffy, D. E. McCormack, J. Colreavy, M. Hidalgo, P. McHale, and S. J. Hinder. Prevention of *Staphylococcus epidermidis* biofilm formation using a low-temperature processed silver-doped phenyltriethoxysilane sol-gel coating. *Biomaterials*, 29(8):963–969, 2008.

[24] K. C. Popat, M. Eltgroth, T. J. LaTempa, C. A. Grimes, and T. A. Desai. Decreased *Staphylococcus epidermis* adhesion and increased osteoblast functionality on antibiotic-loaded titania nanotubes. *Biomaterials*, 28(32):4880–4888, 2007.

[25] H. Altman, D. Steinberg, Y. Porat, A. Mor, D. Fridman, M. Friedman, and G. Bachrach. *In vitro* assessment of antimicrobial peptides as potential agents against several oral bacteria. *Journal of Antimicrobial Chemotherapy*, 58(1):198–201, 2006.

[26] M. A. E. Auty, G. E. Gardiner, S. J. McBrearty, E. O. O'Sullivan, D. M. Mulvihill, J. K. Collins, G. F. Fitzgerald, C. Stanton, and R. P. Ross. Direct *in situ* viability assessment of bacteria in probiotic dairy products using viability staining in conjunction with confocal scanning laser microscopy. *Applied and Environmental Microbiology*, 67(1):420–425, 2001.

[27] J. J. H. Oosterhof, K. J. D. A. Buijssen, H. J. Busscher, B. F. A. M. van der Laan, and H. C. van der Mei. Effects of quaternary ammonium silane coatings on mixed fungal and bacterial biofilms on tracheoesophageal shunt

prostheses. *Applied and Environmental Microbiology*, 72(5):3673–3677, 2006.

[28] Y. Nakata, T. Okada, and M. Maeda. Deposition of ZnO film by pulsed laser deposition at room temperature. *Applied Surface Science*, 197-198:368–370, 2002.

[29] O. Lopatiuk, L. Chernyak, A. Osinsky, J. Q. Xie, and P. P. Chow. Electron-beam-induced current and cathodoluminescence studies of thermally activated increase for carrier diffusion length and lifetime in n-type ZnO. *Applied Physics Letters*, 87(16):162103, 2005.

[30] M. Sun, W. Hao, C. Wang, and T. Wang. A simple and green approach for preparation of ZnO_2 and ZnO under sunlight irradiation. *Chemical Physics Letters*, 443(4-6):342–346, 2007.

[31] Naofumi Uekawa, Naomi Mochizuki, Jyunichi Kajiwara, Fumihiko Mori, Yong Jun Wu, and Kazuyuki Kakegawa. Nonstoichiometric properties of zinc oxide nanoparticles prepared by decomposition of zinc peroxide. *Physical Chemistry Chemical Physics*, 5(5):929–934, 2003.

[32] M. Kunat, S. Gil Girol, T. Becker, U. Burghaus, and C. Wöll. Stability of the polar surfaces of ZnO: A reinvestigation using He-atom scattering. *Physical Review B*, 66(8):081402, 2002.

[33] M. Grunze, W. Hirschwald, and E. Thull. Characterization of thin zinc-rich and oxygen-rich zinc oxide layers. *Thin Solid Films*, 37(3):351–356, 1976.

[34] H. L. Mosbacker, Y. M. Strzhemechny, B. D. White, P. E. Smith, D. C. Look, D. C. Reynolds, C. W. Litton, and L. J. Brillson. Role of near-surface states in ohmic-Schottky conversion of Au contacts to ZnO. *Applied Physics Letters*, 87(1):012102, 2005.

[35] J.-C. Dupin, D. Gonbeau, P. Vinatier, and A. Levasseur. Systematic XPS studies of metal oxides, hydroxides and peroxides. *Physical Chemistry Chemical Physics*, 2(6):1319–1324, 2000.

[36] W. H. Hirschwald. Zinc oxide: An outstanding example of a binary compound semiconductor. *Accounts of Chemical Research*, 18(8):228–234, 1985.

[37] F. J. Manjón, B. Marí, J. Serrano, and A. H. Romero. Silent Raman modes in zinc oxide and related nitrides. *Journal of Applied Physics*, 97(5):053516, 2005.

[38] P. Y. Emelie and B. Phillips, J. D.and Buller. Free carrier absorption and lattice vibrational modes in bulk ZnO. *Journal of Electronic Materials*, 35(4):525–529, 2006.

[39] R. A. Nyquist, C. L. Putzig, and M. A. Leugers. *Handbook of Infrared and Raman Spectra of Inorganic Compounds and Organic Salts*. Academic Press, London, 1997.

[40] X. Domènech, J.A. Ayllón, and J. Peral. H_2O_2 formation from photocatalytic processes at the ZnO/water interface. *Environmental Science and Pollution Research*, 8(4):285–287, 2001.

[41] J. Doménech and A. Prieto. Stability of zinc oxide particles in aqueous suspensions under UV illumination. *Journal of Physical Chemistry*, 90(6):1123–1126, 1986.

Chapter 7

Conclusions & Outlook

The work presented in this thesis encompasses the research performed using a state-of-the-art pulsed laser deposition system to produce both thin and nanostructured films. The material used throughout this work was the wide band gap semiconductor, ZnO, and as proven, displays a wide range of uses both in society and industry. Throughout the course of this thesis work, experiments fell into three main avenues of research: thin films, nanostructures, and device applications.

As shown in comparison to work done on ZnO grown with the PLD method in past and current literature, our work in establishing high-quality ZnO thin films was presented. The growths with differing substrate temperatures over a range of 600-1050 °C were explored and we established depositions around the 850-900 °C substrate temperature range were best for higher-quality, crystalline ZnO thin films. ZnO was also deposited on various substrates, predominantly sapphire, and these ZnO films were found to grow epitaxially atop the sapphire substrates. More work could have been done on improving the quality of ZnO films deposited on silicon substrates. Additionally, this would have included exploring the effects various buffer layers would have on the film quality.

The second area of research developed the conditions for the growth of

nanostructures as well as trying to control this growth. The first parameter presented in this thesis was explored briefly but developed the idea of in-plume crystallisation. The idea was to vary the laser fluence to help assist nanoclusters to develop within the ablation plume as it traveled to the substrate surface. With a fluence of 2 J/cm^2, we did begin to develop nanostructured, ZnO thin films as opposed to smooth, thin films. We also presented a more thorough set of experiments on various sapphire substrate cuts (a-, r-, and c-cut sapphire) with intent to (1) produce the best crystalline quality ZnO films possible for us, and (2) to establish and present x-ray diffraction data (2θ-ω, rocking curve, and ϕ-scans) found for the majority of samples produced throughout this work. Additionally, for those samples which photoluminescence spectra were collected, we presented the PL data for the three cuts of sapphire substrate.

Still in the vein of nanostructures, we devised a comparative set of experiments to further thicken the amount of material deposited onto the substrates. We found that by increasing the number of ablation shots from 4,800 to 18,000 we get columnar-like structures, some of which are hexagonal in shape, which is what we initially set out to achieve. The bulk of the film crystal was found to be of similar quality to those with the fewer number of ablation shots, implying that (1) the crystalline quality was not significantly effected by the additional amount of material deposited, and that (2) we had produced high-crystalline-quality ZnO nanostructures, even if they are not perfectly aligned nanostructures. We also present data where we replace the oxygen process gas with inert argon. The intent was to further manipulate the ablation species as they travel in-plume by using a larger sized, non-reactive, buffer gas. Some unique samples were presented as a result of this experiment. The crystalline structure of these ZnO films were also compromised, likely due to the lack of an external source for a surplus of reactive, oxygen species.

We wanted to further explore this concept of argon as a buffer gas to assist with in-plume crystallisation, so a set of experiments were performed to detail

the results of varying the ratio of growth gas from pure-oxygen through to growth under pure-argon. This data was presented in three separate parts (one for each set grown on the three cuts of sapphire substrate) and an overall model for interpreting this data was presented. Concisely, in a mixed ratio of oxygen and argon, nanostructures were prone to develop due to a strain in the film as it was deposited. This strain is possibly due to the following: (1) as the there is less oxygen and more argon, the argon slows down the ablated species allowing for more in-plume crystallisation with the stoichiometric oxygen from the target, and (2) as these species crystallise in-plume they potentially act as nucleation sites for nanostructured growth as they adsorb to the surface. Extensions of this model would be advantageous to explore with physical means of measuring or detecting species or clusters in-plume to develop this notion of nanoparticle-assisted PLD.

Finally, the last area of research was in developing a ZnO film to be utilised as a device material. In the last chapter of this thesis we present the extensive work carried out to use a ZnO thin film deposited on a glass substrate to inactivate a biofilm of *Staphylococcus epidermidis* when the sample (glass/ZnO/biofilm) is exposed to UV light. A model for this inactivation was proposed and it was corroborated by the presented data. It states that as electron-hole pairs are created due to the UV interaction, photo-holes migrate to the surface which trigger a series of redox-reactions, namely the formation of hydroxyl radicals as the biomaterial is oxidised due to the photo-holes migrating to the ZnO/biofilm interface. The work done in this section of the thesis could be extended to further establish the precise reactions occurring, as well as developing this device for materials other than glass to make it more applicable to the medical or environmental fields, such as plastics or metals.